UTILIZING EMBEDDED SENSING FOR THE DEVELOPMENT OF PIEZORESISTIVE ELASTODYNAMICS

by

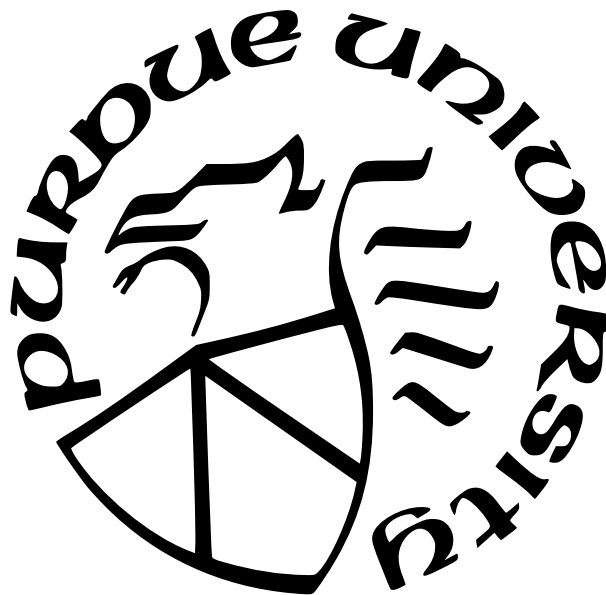**Julio A. Hernandez**

A Dissertation

Submitted to the Faculty of Purdue University

In Partial Fulfillment of the Requirements for the degree of

Doctor of Philosophy

School of Aeronautics and Astronautics

West Lafayette, Indiana

August 2023

THE PURDUE UNIVERSITY GRADUATE SCHOOL
STATEMENT OF COMMITTEE APPROVAL

Dr. Tyler N. Tallman, Chair

School of Aeronautics and Astronautics

Dr. Wayne Chen

School of Aeronautics and Astronautics

Dr. Byron Pipes

School of Aeronautics and Astronautics

Dr. Fabio Semperlotti

School of Mechanical Engineering

Approved by:

Dr. Gregory Blaisdell

¡Hasta las estrellas!

ACKNOWLEDGMENTS

TABLE OF CONTENTS

LIST OF TABLES

LIST OF FIGURES

ABBREVIATIONS

CB   Carbon Black

CEM   Complete Electrode Model

CNF   Carbon Nanofibers

CNT   Carbon Nanotube

EIT   Electrical Impedance Tomography

EMI   Electrical Magnetic Interference

FEA   Finite Element Analysis

FEM   Finite Element Modeling

FFT   Fast Fourier Transform

GFRP   Glass Fiber Reinforced Polymer

GNP   Graphene Nanoparticles

IMM   Idiopathic Inflammatory Myopathics

LV   Laser Vibrometry

MRI   Magnetic Resonance Imaging

MWCNT   Multiwalled Carbon Nanotube

PVA   Polyvinyl Alcohol

PVDF   Polyvinylide Fluroride

PVP   Polyvinyle Pyrrolidone

PZT   Lead Zirconate Titanate

SEM   Scanning Electron Microscopy

SHPB   Split-Hopkinson Pressure Bar

ToF   Time of flight

ABSTRACT

Obtaining full-field *dynamic* material state awareness would have profound and wide-ranging implications across many fields and disciplines. For example, achieving dynamic state awareness in soft tissues could lead to the early detection of pathophysiological conditions. Applications in geology and seismology could enhance the accuracy of locating mineral and hydrocarbon resources for extraction or unstable subsurface formations. Ensuring safe interaction at the human-machine interfaces in soft robotic applications is another example. And as a final representative example, knowing real-time material dynamics in safety-critical structures and infrastructure can mitigate catastrophic failures. Because many materials (e.g., carbon fiber-reinforced polymers composites, ceramic matrix composites, biological tissues, cementitious and geological materials, and nanocomposites) exhibit coupling between their mechanical state and electrical transport characteristics, self-sensing via the piezoresistive effect is a potential gateway to these capabilities. While piezoresistivity has been mostly explored in static and quasi-static conditions, using piezoresistivity to achieve dynamic material state awareness is comparatively unstudied. Herein lies the significant gap in the state of the art: the piezoresistive effect has yet to be studied for in-situ dynamic sensing.

In this thesis, the gap in the state of the art is addressed by studying the piezoresistive effect of carbon nanocomposites subject to high-rate and transient elastic loading. Nanocomposites were chosen merely as a representative self-sensing material in this study because of their ease of manufacturability and our good understanding of their electro-mechanical coupling. Slender rods were manufactured using epoxy, modified with a small weight fraction of nanofillers such as carbon black (CB), carbon nanofibers (CNFs), and multi-walled carbon nanotubes (MWCNTs), and subject to loading states such as steady-state vibration at structural frequencies ($10^2 - 10^4$ Hz), controlled wave packet excitation, and high-strain rate impact loading in a split-Hopkinson pressure bar. This work discovers foundational principles for dynamic material state awareness through piezoresistivity.

Three major scholarly contributions are made in this dissertation. First, an investigation was pursued to establish dynamic, high-strain rate sensing. This investigation clearly demon-

strated the ability of piezoresistivity to accurately track rapid and spatially-varying deformation for strain rates up to 10^2 s^{-1}. Second, piezoresistivity was used to detect steady-state vibrations common at structural frequencies. Utilizing simple signal processing techniques, it was possible to extract the excitation frequency embedded into the collected electrical measurements. The third contribution examined the dynamic piezoresistive effect through an array of surface-mounted electrodes on CNF/epoxy rods subject to highly-controlled wave packet excitation. Electrode-spacing adjustments were found to induce artificial signal filtering by containing larger portions of the injected wave packets. The strain state in the rod was found after employing an inverse conductivity-to-mechanics model, thereby demonstrating the possibility of deducing actual in-situ strains via this technique. A digital twin in ABAQUS was constructed, and an elastodynamic simulation was conducted using identical dynamic loading, the results of which showed very good agreement with the piezo-inverted strains.

This work creates the first intellectual pathway to full-field dynamic embedded sensing. This work has far-reaching potential applications in many fields, as numerous materials exhibit self-sensing characteristics through deformation-dependent changes to electrical properties. Therefore, *piezoresistive elastodynamics* has the incredible potential to be applied not just in structural applications but in other potentially innovated applications where measuring dynamic behavior through self-sensing materials is possible.

1. LITERATURE REVIEW

1.1 Introduction

1.1.1 Applications of Elastodynamics

Knowing the full-field dynamics [1] [2] of materials would be immensely beneficial to a diverse number of fields and applications, such as geology, biomedicine, and engineering. For example, seismologists and geophysicists employ seismic waves to conduct subsurface environmental assessment surveys for geological instabilities in seismically active areas prior to civil construction and to advance exploration efforts to extract natural resources such as minerals and hydrocarbons [3] [4] [5] [6] [7]. In clinical applications, ultrasound is a common tool to inject high-frequency and nondamaging vibrations into patients. The reflections are used to reconstruct the boundaries between fluids and tissues to aid in medical diagnostics [8] [9] [10]. In the field of engineering, the structure's dynamic response can be used to assess its current condition [11] [12].

However, physically capturing full-field dynamic behavior is challenging to achieve with conventional sensing. As a result, advanced analytical tools were created to comprehend the dynamic data from a sparse sensor network and achieve material state awareness. For example, these tools can be used to discern subtle changes in material properties within an entire body from surface measurements. In a geological context, it is well known that different subsurface strata exhibit different geomechanical properties (e.g., density, elastic properties, porosity, etc.). Among the different geological layers are minerals and natural resources that may have subtly different properties than the surrounding material. Identifying and delineating these regions of interest can be a complex task with seismic waves due to the fact that mechanically similar materials can produce low-amplitude wave reflections. This often requires employing an array of geophones to enhance geolocation efforts. Chen et al. [13] used a shallow seismic exploration method to detect and spatially locate gold ore deposits to a depth of 600 m. In addition to identifying ore deposits, seismic velocity structures for different lithologic layers were also determined and provided a spatial mapping of the subsurface strata. Markovic et al. [14] used seismic reflection methods for the mineral exploration of skarn-type and apatite-rich iron-oxide deposits initially believed to be at a

depth of 850 m based on historical drilling. Several new reflections identified additional unknown ore veins extending 300 meters further down. Koivisto et al. [15] conducted a reflection seismic survey on platinum group mineral veins within the local geology of layered sedimentary and volcanic rocks down to a depth of 1.5 km. This work was found to be in good agreement with a similar study using three-dimensional reflection seismology by Malehmir et al. [16]. It is worth mentioning the nature of geotechnical surveying invokes a mathematical inverse problem on account that the specific depth and regions of different subsurface materials must be calculated from a sparse set of surface measurements [17] [18].

The biomedical field encounters similar challenges to geologists and seismologists, where noninvasive diagnostics (i.e., surface measurements) are heavily preferred. Therefore insights must be made about subsurface regions of interest from remote measurements. Elastography is a non-invasive and non-damaging imaging modality to study soft tissue biomechanics. The fundamental principle of elastography is to utilize dynamic mechanical excitations to ascertain changes to the elasticity of biological tissue [19]. Changes to the viscoelastic properties of tissues can serve as indicators of possible pathophysiological conditions leading to fibrosis or impaired tissue function. For example, the elasticity of ocular and periocular tissue was examined by Li et al. [20] using ultrasound elastography. Ocular hypertension was simulated in the tissue sample, and a change in biomechanical properties was observed through variations in wave velocity and tissue elasticity. Shih et al. [21] conducted an intravascular assessment of atherosclerotic disease using a dual-frequency transducer for ultrasonic shear wave elastography. It was found that the regions with atherosclerotic plaque can be distinguished. The difference in shear modulus properties between healthy and diseased tissue was up to 1.6 kPa. Alfuraih et al. [22] utilized shear wave elastography to investigate idiopathic inflammatory myopathies (IMM). Findings resolved through substantial differences in shear wave velocities reduced muscle stiffness due to the effects of IMM on muscle tissue and its effects on biomechanical properties. Elastography can also be combined with the capabilities of magnetic resonance imaging (MRI) [23] to directly capture wave motion and then apply an inversion algorithm to convert the data collected into an elastogram. Magnetic resonance elastography has been employed to great effect in detecting liver fibrosis [24], malignant and benign tumors in breast [25] and brain tissue [26], and abnormal cardiovascular function [27].
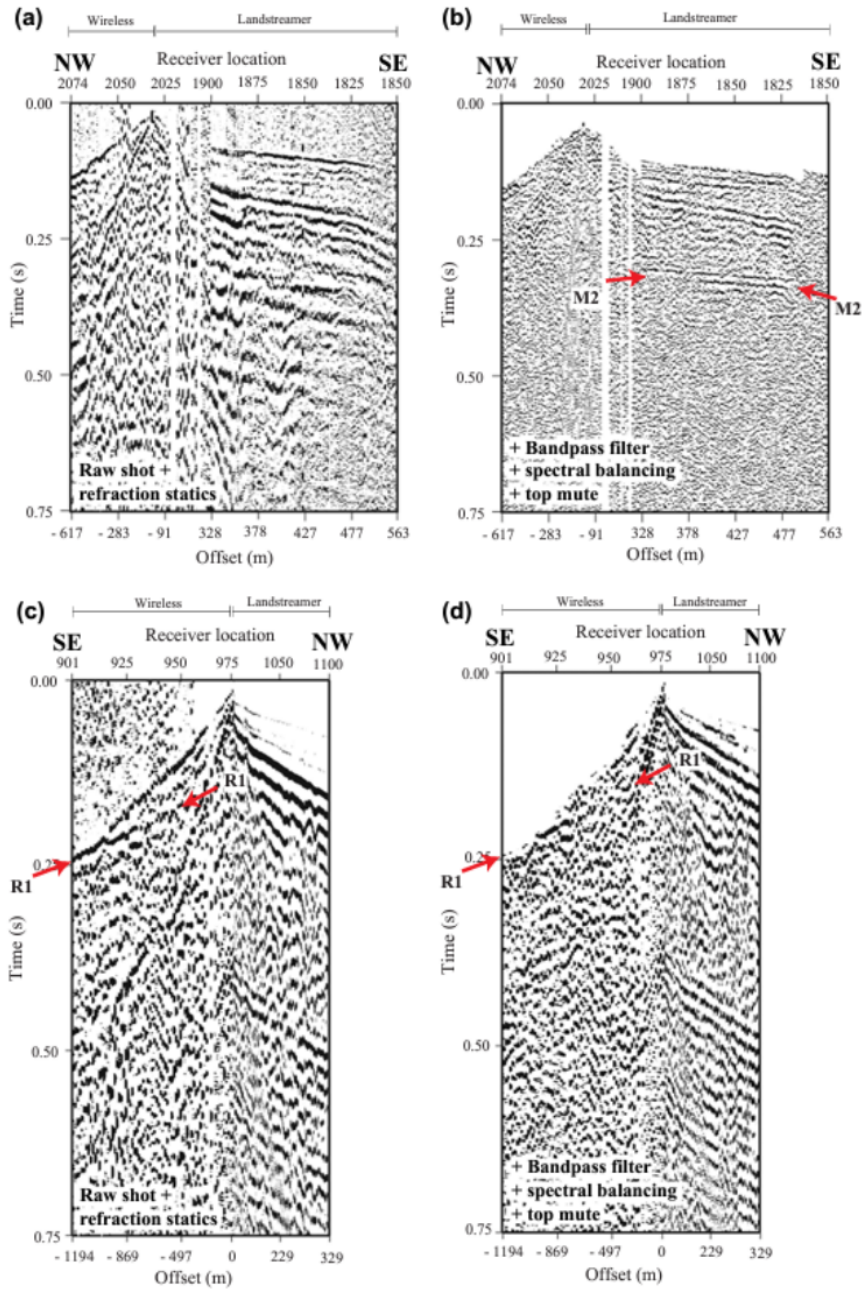
Figure 1.1. Explosive shots were generated to transmit elastic waves and measure reflections through an array of equally spaced geophones. (a) Raw shot data was collected through geophones. (b) A bandpass filter, spectral balancing, and "top-mute" were applied for signal conditioning. Red arrows pointing to M1 and M2 likely denote mineralization. (c) Raw shot data at another location. (d) Post-signal conditioning of collected data reveals likely locations of subsurface fault lines in strata (R1 and R2) [14].

In engineering, vibration methods are well-established techniques that greatly improve operational safety and reliability by capturing changes to the nominal dynamic behavior of structures [28] [29] [30]. Guided waves can be utilized in various applications where the structural components act as transmission paths or waveguides for the propagation of transmitted waves and their reflections [31] [32] [33] [34]. Most guided wave efforts focus on damage/flaw detection and localization. Two examples using composite materials are as follows: Li et al. [35] employed co-linear guided waves to identify the presence and spatial position of low-velocity impact-induced damage on a carbon fiber-reinforced polymer composite. The presence of damage could be inferred in the spectral domain where the variation in mixing frequency components peak counts was found to have a positive correlation with impact energy, denoting more significant nonlinear acoustic behavior in the material due to the presence of damage. Sherafat et al. [36] created artificial single-ply cracks using Teflon tape in a carbon fiber-reinforced polymer composite and employed ultrasonic-guided waves. The condition of the composite panel was measured by the scattering of the reflected waves as a function of wave frequency. It was found the effect of excitation wavelength is a crucial factor in reflection, transmission, and scattering behavior in damage detection efforts.

1.1.2   Self-Sensing Materials for Discrete Structural Sensing

Common to all elastodynamic approaches is the reliance on physical sensors (e.g., metallic foil strain gages [37] [38], accelerometers (PZT) [39] [40], fiber optic cables [41] [42], lead zirconate titanate transducers [43] [44]) to accurately capture dynamic behavior. Although physical sensors are ubiquitous and highly effective, practical limitations exist. Physical sensors are constrained by their ability to physically sense at specific locations, and large distributed sensing arrays may incur significant mass penalties.

One promising solution is to leverage self-sensing materials with deformation-dependent changes to electrical behavior. Self-sensing can occur in natural materials, such as in biological cells [45] [46], semi-saturated soils [47] [48], and certain minerals/ores [49] [50], or artificially, such as in cements [51] [52], continuous carbon fiber composites [53] [54], and nanocomposites [55] [56]. Nanocomposites are the most commonly studied materials where

self-sensing is expressed through the piezoresistive effect [57] [58] [59] [60] [61] [62]. Piezoresistive materials can achieve mechanical state awareness at discrete locations or over spatially distributed regions. In composites, this is made possible with the dispersion of small quantities of nanofiller inclusions (such as CBs, CNFs, carbon nanotubes, and graphene nanoplatelets) into the matrix material. A well-connected conductive network is formed when the nanofillers are properly dispersed, and the deformation of the nanocomposite will result in a change in the conductive network due to individual nanofiller movement. Variations in the inter-filler distance will change the resistance experienced by electrons as they tunnel between adjacent nanofillers across the conductive network [63] [64]. This change in electron tunneling resistance manifests as bulk changes in the intrinsic electrical properties of the nanocomposite [65] [66] [67] that can then be measured. Exploiting this deformation-dependent electrical behavior enables piezoresistivity to be used for mechanical sensing and inferring material state awareness.

The piezoresistive effect has proven to be highly effective in monitoring highly dynamic behavior. Within an elastodynamic framework, the piezoresistive sensors have been employed as surface patch sensors at discrete locations. For example, Zeng et al. [69] manufactured various weight fractions of MWCNT and CB-modified polyvinylidene fluoride (PVDF) sensors for steady-state 100 Hz–3 kHz vibration and ultrasonic guided wave monitoring up to 400 kHz. The piezoresistive sensors were found to accurately track dynamically changing loads and capture the propagation of the zeroth symmetric and antisymmetric modes of ultrasonic wave packet transmissions into a 600 mm × 600 mm steel plate. Zhou et al. [68] produced inkjet-printed piezoresistive sensors using CB nanofillers and polyvinyl pyrrolidone (PVP). The printed flexible sensors were adhered onto a 400 mm × 400 mm glass fiber reinforced polymer (GFRP) laminate plate and subject to sinusoidal tonal bursts (i.e., wave packets) at frequencies ranging from 50 kHz–500 kHz. The signals recorded from the CB/PVP sensors faithfully recorded both the zeroth order symmetric and antisymmetric modes. In a later study, Zhou et al. [70] found the capabilities of CB/PVP sensors maintained stable sensing capabilities at temperatures ranging between -60 °C and 150 °C typical for aircraft and spacecraft operations using the same ultrasonic methods. Cao et al. [71] developed graphene/PVP material that could be sprayed onto surfaces to create a thin piezoresistive
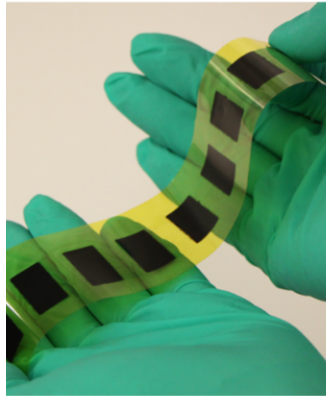
(a)
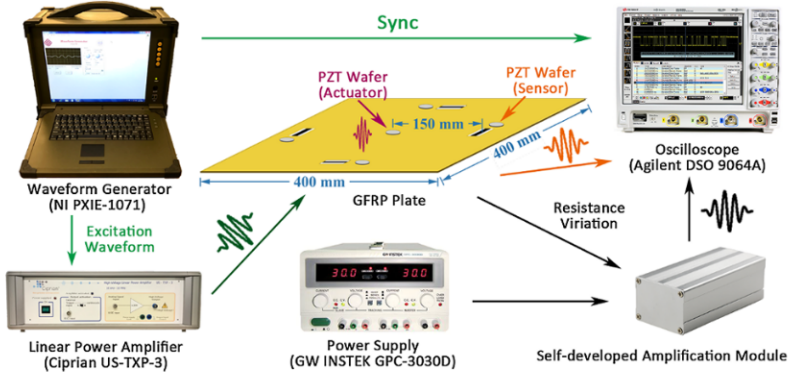
(b)
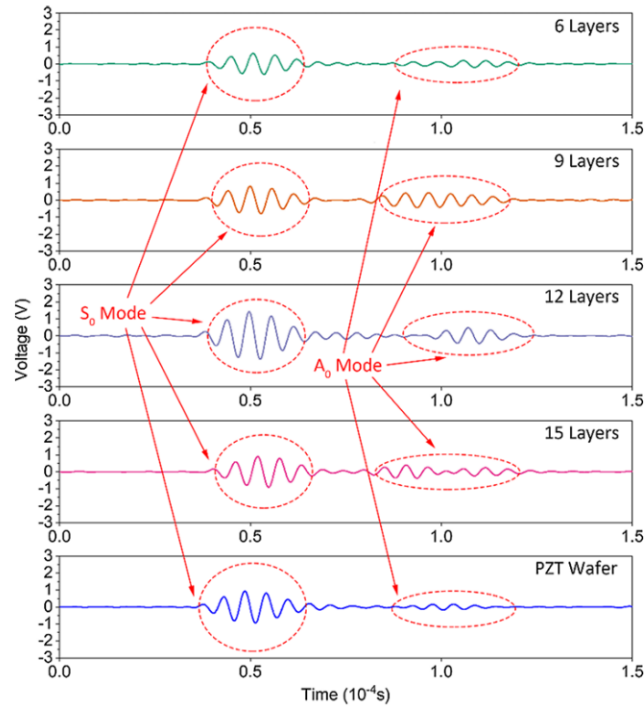
(c)

Figure 1.2. (a) Inkjet printed CB/PVP sensors directly deposited on polyimide film. (b) Experimental setup with CB/PVP sensors and PZT wafers adhered onto a GFRP laminate place. Ultrasonic wave packets were inserted into the plate and detected through the adhered sensors. (c) Raw ultrasound signals were captured by the ink jet-printed CB/PVP sensors. The sensors accurately captured the zeroth symmetric and antisymmetric modes [68].

film. Discrete patch sensors were created on a 500 mm × 500 mm aluminum plate to monitor ultra-high frequency guided wave transmission. A bonded mass on the plate simulated energy scattering and reflection phenomenon (i.e., artificial damage). This change in wave behavior was accurately recorded through the piezoresistive sensors. Furthermore, time-of-flight calculations accurately determined the positioning of the bonded mass on the plate based on wave reflections.

It is important to note that the aforementioned contributions developed surface-mounted discrete piezoresistive sensors rather than using a continuous approach wherein the entire structure is the sensor (which is an important distinguishing factor of this thesis work). In the interest of advancing subsurface measurement capabilities, Sun et al. [72] [73] created spray-coated graphene/PVP sensors with carbon nanotube film wires with remarkable thinness, approximately 45 μm. The prepared sensors were implanted into an E-glass epoxy and used for in-situ monitoring of cure kinetics using elastodynamics. Furthermore, the implanted sensors had good sensing capabilities to observe broadband excitations ranging from steady-state vibrations to lamb wave transmissions up to 450 kHz.

1.1.3 In-Situ Piezoresistive Dynamics

Although piezoresistive sensors have proven to be widely effective in monitoring highly dynamic mechanical behaviors, it suffers from a significant limitation. The aforementioned section demonstrated discrete piezoresistivity-based sensors conducting measurements at certain locations. Design and environmental constraints may prevent attaching densely or large-scale distributed piezoresistive sensor arrays. Fortunately, imparting the piezoresistive effect into the material itself (as opposed to attaching discrete sensors) for spatially distributed sensing would address this limitation where entire material or structural-level sensing can be conducted between opposite locations. This section will discuss how piezoresistivity can be leveraged for full-scale in-situ measurements of highly dynamic behavior.

Piezoresistivity enables the sensing of highly dynamic behaviors throughout entire structures. Ubertinit et al. [75] introduced 2 wt.% carbon nanotubes (CNTs) into cement to track cyclic excitations in the range of 0.25 Hz–15 Hz. This study showcased that large
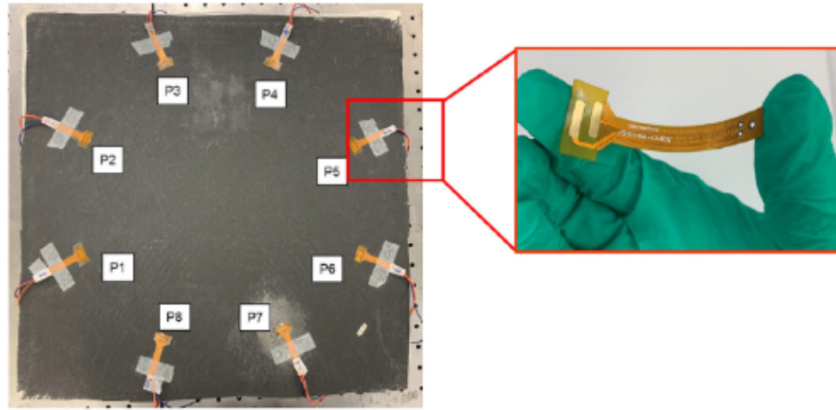
(a)
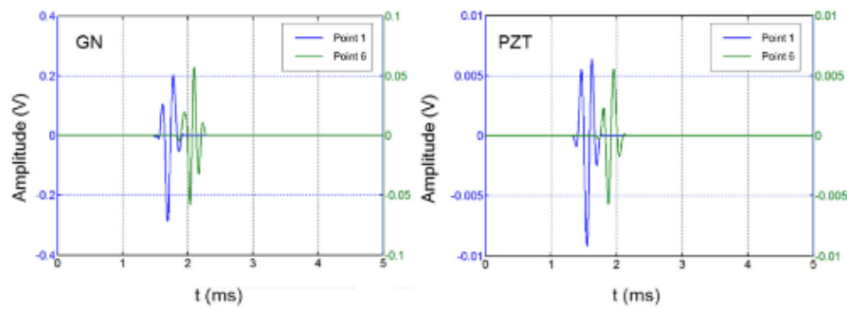
(b)
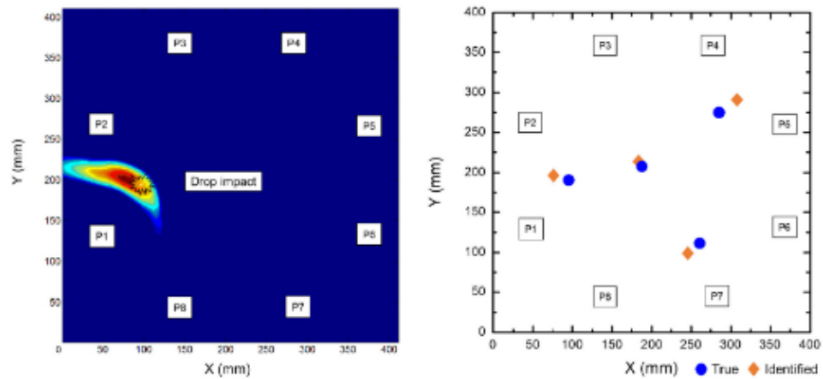
(c)

Figure 1.3. (a) GNP/GFRP laminate plate with printed conductive electrodes adhered onto the surface. (b) Acoustic emissions can be detected from the electrodes and PZT wafers adhered to the surface of the GNP/GFRP plate. (c) Using time of flight calculations, the locations of acoustic emission sources can be accurately determined [74].

structural-level piezoresistive dynamics can be detected. Garcia et al. [76] manufactured a 0.5 wt.% CB/GFRP laminate beam with electrodes placed at the ends of the beam. Electrical resistance measurements were taken across the beam while the beam was subject to 30 Hz and 500 Hz and steady-state harmonic excitation. Furthermore, the effect of two different damage types, a concentrated mass and a drilled hole, were investigated through piezoresistive measurements. Examination of response peaks in the frequency domain indicated a change in the material state of the CB/GFRP beam can be clearly distinguished through piezoresistive measurements. Li. et al. [77] leveraged the piezoresistive effect of graphene nanoparticles (GNP) GFRP plate for guided wave applications. Printed electrical circuits and electrodes were made to form a distributed electrode sensing array on the surface of the GNP/GFRP plate to detect 180 kHz guided waves. The response from the sensing electrodes and surface-mounted PZT wafers was found to be in good agreement. The electrode sensing array proved a proof-of-concept application that guided wave propagation could be monitored from any point on the nanocomposite plate through piezoresistive measurements. Furthermore, the location of the original excitation can be triangulated with time-of-flight calculations. In a later study, Li et al. [74] revisited the topic of distributed piezoresistive-based sensing through surface-mounted printed electrodes for guided wave applications in a GNP/GFRP plate. The exact source location of dropped steel balls on the plate could be obtained from piezoresistive observations of acoustic emissions below 10 kHz. The dispersion curves of the composite plate were also experimentally determined up to 500 kHz with the aid of commercially available software [78].

As shown above, comparatively little has been done in the field of piezoresistive dynamics at high rates of deformation through structural level measurements. Some have shown tracking highly dynamic behavior is possible from direct electrical measurements from nanofiller-modified composite structures; however, none have utilized piezoresistivity for in-situ elastodynamics. Furthermore, no work has been done to integrate dynamic piezoresistivity with conductivity imaging modalities like electrical impedance tomography [79] [66] [80] [81] to capture the spatial and time-varying behavior within a self-sensing body. Because the previously described broader applications of piezoresistive self-sensing do indeed have precedent for using electrical impedance tomography (EIT) (e.g., biomedical imaging

[82] [83] [84], geospatial prospecting and exploration [85] [86] [87], structural health and condition monitoring [61] [88] [89], etc.), this very feasible next step to expand the capabilities of conductivity imaging modalities for full-field dynamic imaging.

2. PROBLEM STATEMENT, RESEARCH GOAL, DISSERTATION CONTRIBUTIONS, AND DISSERTATION ORGANIZATION

Problem Statement: The piezoresistive effect has immense potential for realizing embedded sensing of full-field dynamics. Many materials, both engineered and naturally occurring, exhibit piezoresistive behavior, and many applications would benefit from knowledge of in-situ full-field dynamics. However, very few have used dynamic piezoresistivity to directly extract specific material mechanical characteristics through electrical measurements. This important is an important limitation as a successful combination of piezoresistivity with elastodynamics can achieve unprecedented *dynamic* material state awareness with relatively simple hardware requirements (i.e., power supply and voltage measurement device). Furthermore, the piezoresistive effect enables spatially distributed sensing capabilities that can be leveraged to make these insights through remote, embedded, and subsurface measurements.

Research Goal: The goal of this thesis is to pioneer the field of *piezoresistive elastodynamics.* None have investigated leveraging coupled electro-mechanical properties for elastodynamics to discover the basics of dynamic self-sensing principles. Knowledge gained through discovering dynamic behavior in a carbon nanofiller-modified epoxy material is anticipated to be translatable to any material with piezoresistive characteristics. The work herein can therefore open a new avenue for advancing dynamics-integrated self-sensing to obtain full-field material state awareness.

Dissertation Contributions: This dissertation makes three important contributions toward the aforementioned research goal. First, the work herein established piezoresistivity can effectively enable material state awareness utilizing highly dynamic behavior. The significance of this contribution is that in situ material characterization can be shown to be achieved from dynamic and rapid mechanical perturbations such as elastic stress waves. Second, not only can highly dynamic and transient events be tracked, but material condition-relevant data can be ascertained, such as excitation frequencies, material speed of sound, and dynamic modulus. Furthermore, signal filtering of excitations can be made by adjusting electrode configuration or spacing between measurement points. Third, combining analytical

piezoresistivity and complete electrode modeling can lead to strain state determination at certain locations along the nanocomposite rod through the piezo-inversion process. This is possible by employing a first-principles-based analytical piezoresistivity model to recover the strain state from recorded electrical measurements.

1. Elastic stress wave tracking via the piezoresistive effect: High-rate impact loading, steady-state vibrations, and repeatable wave packet excitations were effectively monitored by utilizing electrical measurements obtained from surface-mounted electrodes on nanocomposite rods. The significance of this contribution is to clearly demonstrate dynamic piezoresistivity can be utilized for in-situ material characterization, such as obtaining excitation frequencies, material speed of sound, and dynamic modulus

2. Passive signal filtering of dynamic electrical signals: The influence of electrode spacing (i.e., the distance between measurement points) on the collected electrical measurements was investigated as a potential avenue to achieve passive signal filtering on CNF/epoxy rods. This is an important contribution because it demonstrates how electrode topology can be used as a physical filter for certain information contained in elastic waves.

3. Material-state determination from elastodynamic testing: Recovering the strain state in the measurement region between adjacently placed electrodes was achieved. Furthermore, the energy-dissipative characteristics (i.e., damping/attenuation) were accurately determined from piezo-inverted strains and utilized in an ABAQUS digital twin model to qualitatively obtain full-field mechanics of a 1.5 wt.% CNF/epoxy rod. This is a substantial contribution because it outlines a direct pathway to obtain full-field material state awareness through piezoresistive elastodynamics.

Thesis Organization: The organization of this dissertation is as follows. First, an overview of the experimental methodology is presented. This includes subsections on the nanofiller-modified epoxy material manufacturing process, cast manufacturing to form rod structures, and the electrode attachment process. Next, the experimental setup subsection will present

the specific equipment arrangement for the split-Hopkinson pressure bar (SHPB) apparatus to subject nanocomposite rods to high-rate elastic wave propagation and an open and closed-loop piezoelectric/magnetic shaker system to excite the manufactured rods under steady-state vibrations and controlled wave packet injections. The following subsection will outline the specific equipment arrangement to take piezoresistive measurements from the rods during loading. Then, the complete electrode model is described to outline computational modeling efforts. The experimental results section will follow the experimental methodology section. The dissertation will finally be concluded with a brief summary of work and state recommendations for future possible expansion of this framework or body of work developed.

3. EXPERIMENTAL METHODOLOGY

This chapter discusses the experimental work performed to develop piezoresistive elastodynamics for embedded sensing applications. This includes composite manufacturing, electrical interrogation, mechanical testing, and data collection. Three types of self-sensing composites were manufactured: Carbon Black (CB), Carbon Nanofiber (CNF), and Multi-Walled Carbon Nanotube (MWCNTs)-modified epoxy. The following sections describe the manufacturing and experimental procedures in detail.

3.1 Nanocomposite Specimen Preparation

As a test bed to explore dynamic piezoresistivity, carbon nanofiller-modified polymers were manufactured and subject to dynamic loading and transient mechanical excitation. The following sections will outline the material manufacturing procedure and the specific cast process to form long prismatic rod specimens.

3.1.1 Nanocomposite Material Manufacturing Process

A modified nanocomposite manufacturing procedure, originally developed by Tallman et al. [60], was utilized in this investigation for material preparation. In this manufacturing method, nanofillers are dispersed into epoxy material with the aid of a surfactant, high-energy mechanical mixing, and ultra-sonication [60] [90] [91]. The work in this thesis utilized CB Pearls 2000 (CABOT, Alpharetta, Georgia, USA), Pyrograf-III PR-24-XT-HHT unfunctionalized CNFs (Applied Sciences Inc., Cedarville, OH, USA) with an outer diameter and length of 100 nm and 50 μm, and MWCNTs (Cheap Tubes Inc., Grafton, VT, USA) with an outer diameter and length of <8 nm and 10-30 μm, respectively.

The specific quantity of nanofillers utilized in manufacturing a piezoresistive nanocomposite must consider two critical factors: 1) The likelihood of establishing a conductive network within the subsurface and 2) processability during manufacturing. To leverage the piezoresistive effect, nanocomposites must have particle concentrations near or exceeding the percolation threshold. The percolation threshold is the critical concentration where there is a

high probability that a well-connected network of particles is formed within the nanocomposite. When using conductive nanoparticles, dramatic improvements to the nanocomposite's bulk electrical properties can be observed at this point. Localized deformation to the connected nanofiller network will manifest as changes in the bulk electrical properties that can be measured using simple current injection and voltage measurement techniques. Utilizing a concentration of nanofillers beyond the percolation threshold can lead to fewer variations in the spatial distribution of electrical properties and piezoresistive behaviors. However, the benefits gained are at the expense of increased nanofiller/epoxy mixture viscosity and diminished strain sensitivity. Therefore, the specific concentration of nanofillers used to manufacture a piezoresistive nanocomposite should be carefully determined, taking into consideration factors such as manufacturing processability and the probability of establishing a conductive network. The work utilized nanofiller concentrations between 0.5%-1.5% relative to the total polymer matrix (i.e., epoxy resin + hardener). This specific concentration range exceeded the percolation threshold of each nanofiller material without producing an overly viscous material to inhibit the lost glass casting process employed.

The procedure to manufacture polymer nanocomposites is as follows. First, a specific quantity of nanofillers is measured and introduced into FibreGlast 2000 epoxy resin (FibreGlast, Brookville, OH, USA). Acetone was then added to the mixture at an acetone-to-resin volume ratio of 1:2. Acetone serves to thin or decrease the mixture's viscosity and increase the effectiveness of sonication to increase the dispersion of nanofillers [92]. Next, Triton X-100 surfactant (bioWORLD, Dublin, OH, USA) was incorporated into the nanofiller/resin mixture at a surfactant-to-nanofiller mass ratio of 0.76:1. Surfactants have an ameliorating effect on carbon nanofiller dispersion through a chemical modification of the nanofiller surface [93] [94] [95]. Then, the nanofiller/resin/surfactant mixture was mixed by hand for five minutes with a glass stir rod before being stirred five minutes further in an AR-100 compact planetary centrifugal mixture (Thinky USA, Laguna Hills, CA, USA). After stirring, the nanofiller/resin/surfactant mixture was placed within a CP360HT bath sonicator (Crest Ultrasonics, Trenton, NJ, USA) for two hours per ten grams of resin. The mixture was periodically stirred by hand using a glass stir rod to ensure even sonication. After sonication, the nanofiller/resin/surfactant mixture was transferred to a hot plate stirrer for 24 hrs at

600 rpm to evaporate the solvent. Next, the mixture was cooled 5 °C using an ice bath, thereby extending the pot life of the material. Then, the nanofiller/resin/surfactant mixture received the addition of FibreGlast 2020 epoxy hardener (FibreGlast, Brookville, OH, USA) and BYK A-501 air release agent (BYK USA, Earth City, MO, USA) at a hardener-to-resin mass and total epoxy-to-air release agent ratio of 23:100 and 0.3:100, respectively. Finally, the nanofiller-modified epoxy mixture was mechanically stirred by hand with a glass stir rod for five minutes and degassed in a vacuum chamber for ten minutes before being cast.

3.1.2   Cast Manufacturing of Rod Specimens

Lost glass mold casting manufacturing was employed to produce nanofiller-modified epoxy rod structures. Lost glass mold casting is a specialized form of non-reusable cast molding manufacturing that uses a glass mold to contain liquid material. Once solidified, the component is removed by carefully destroying the glass mold. This method offers several notable benefits. Components cast in glass molds have superior surface quality due to the smoothness mold material. Furthermore, glass molds can withstand high casting temperatures. However, utilizing this method poses several significant challenges. Improper treatment or preparation of the mold surface may increase the likelihood of the cast material adhering to the mold. A significant mismatch in the coefficients of thermal expansion of the cast material and glass mold may produce substantial residual stresses and fracture the cast component or mold when cooling from an elevated temperature. Lastly, the fragility of the glass mold must not be ignored in any step of the manufacturing process.

The manufacturing steps for producing long and large aspect ratio nanofiller-modified epoxy rod structures via lost glass mold casting are described. First, Corning Pyrex Borosilicate Glass Tubing (Wale Apparatus, Hellerton, PA, USA) was prepared by cleaning the interior of the mold with acetone. Second, three thin coats of polyvinyl alcohol (PVA) release film (Fibre Glast, Brookville, OH, USA) were applied to the interior surface of the glass mold. The PVA release film serves as a physical barrier between the liquid nanofiller-modified epoxy mixture and the glass surface of the mold. Third, a silicone stopper was cast at one end of the glass mold to create an airtight seal. Fourth, the prepared nanofiller-

Nanocomposite Material Manufacturing

1 Nanofillers
  Epoxy Resin
  Surfactant
  Acetone

2 Stir Mixture
  5 min.

3 Sonicate Mixture
  2 hrs/10 g

4 Stir Mixture
  24 hrs @ 60°C
  600 RPM

5 Chill Mixture

6 Stir into Mixure:
  Epoxy Hardener
  Air Release Agent

7 Degass
  10 min.

8 Clean Interior
  Apply Release Film x3

9 Cast Silicone Stopper

10 Pour Nanofiller-modified
   Epoxy Mixture

11 Cure Material

12 Remove Rod
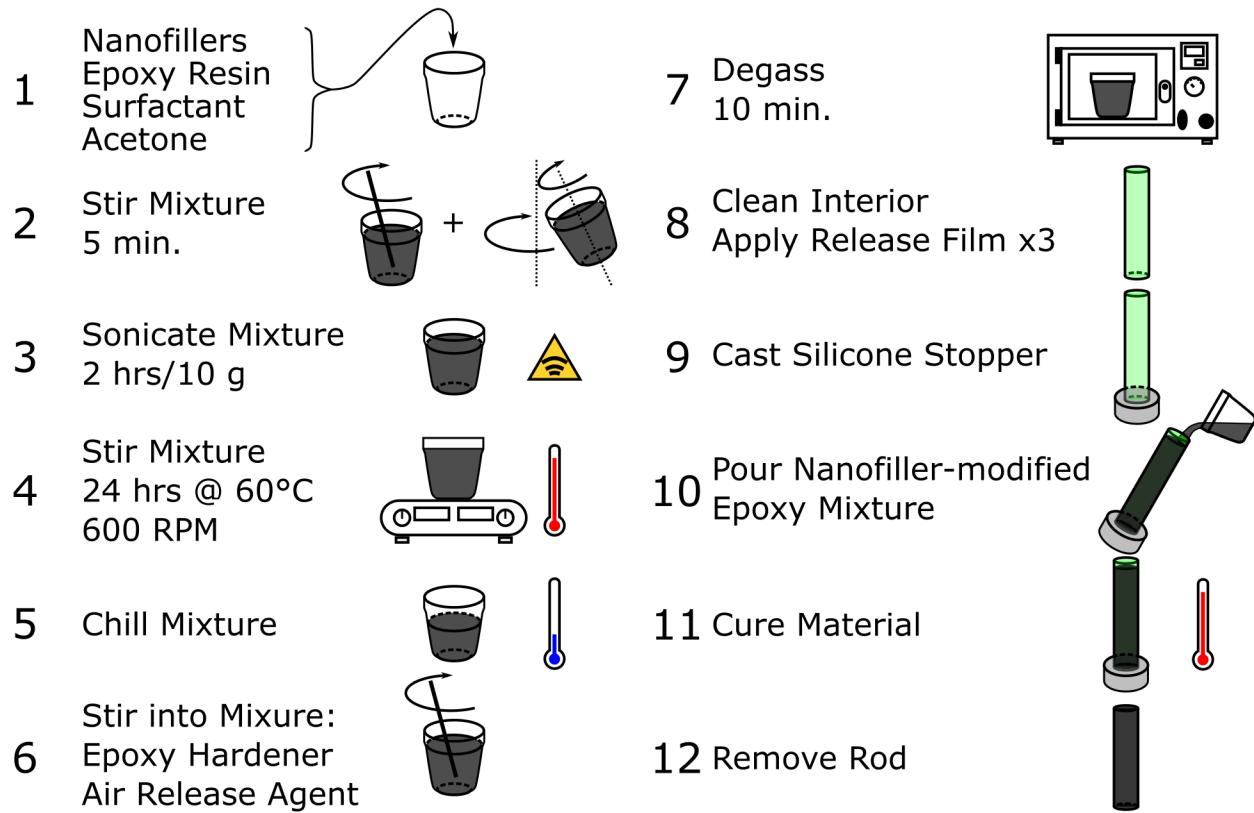
Figure 3.1. Manufacturing nanofiller epoxy rods involves a multistep process to introduce and disperse the nanofillers into the epoxy material. A solvent, such as acetone, is employed to lower the viscosity of the mixture to enable more effective ultrasonication of the mixture by lowering its viscosity. The prepared mixture must be carefully poured into the glass mold before being cured and removed. This entire manufacturing process is outlined as a simple schematic.

modified epoxy was carefully poured into the glass mold at an angle to avoid introducing air bubbles. Fifth, the epoxy-filled tube was then cured. At this stage, the specific curing process is determined by the overall volume of the material utilized. This is due to the fact that the cure kinetics of thermoset epoxies produces an exothermic process that can potentially generate large amounts of heat. In this work, the rods measuring 22 mm in diameter and 505 mm in length, and 12.6 mm in diameter, and 685.8 mm in length were manufactured for high-strain rate impacts and controlled vibration mechanical excitation. The smaller diameter rods were cured in an oven for 5 hours at 80 °C. The larger diameter rods were cured at

room temperature for 12 hours due to the exothermic reaction generating sufficient internal heat to cure and harden the material. After curing, the glass tube was carefully broken to remove the nanofiller-modified epoxy material. Finally, the rods were cut to length using a water-cooled tile saw. The 22 mm diameter and 12.6 mm diameter rods were cut to a length of 560 mm and 700 mm, respectively.

Short small aspect ratio cylinders were also manufactured using the procedure described above for dynamic mechanical characterization. A total of 36 specimens were produced for each nanofiller type investigated. In preparation for testing in an SHPB system, the circular surfaces of the specimens were polished on a rotary water M-prep grinder/polisher (Allied High Tech Products Inc., Rancho Dominguez, CA, USA) using 1200 and 2400-grit sandpaper. Additionally, unmodified epoxy specimens were fabricated to establish a baseline for comparison of dynamic modulus. It is important to have smooth and parallel surfaces to facilitate good transmission of the incident stress wave into the specimen.

3.1.3 Electrode Attachment

High Strain-Rate Impact and Steady-State Vibration Testing

After cutting the nanofiller-modified epoxy rods to length in a water-cooled tile saw, the rod surfaces were sanded with sandpaper to expose the nanofiller network. Residual particulates from sanding were removed using acetone and Kim wipes. Three electrodes were placed at the mid-length of the rod using a combination of silver paint (Ted Pella, Redding, CA, USA) and copper tape (Ted Pella, Redding, CA, USA). Each electrode was applied about the circumference of the rod, measuring 3.18 mm in width and with a spacing of 3.18 mm apart. Lastly, 34 AWG wire adhered to the copper tape electrodes using conductive silver epoxy. This specific combination of silver paint, copper tape, copper wire, and conductive epoxy was chosen to ensure secure and stable voltage measurements from the rod under dynamic impact loading conditions.

Prepared Nanocomposite Rod for SHPB and Steady-State Vibration

Cross Section B-B

Current Injection Electrode

Current Grounding Electrodes

(a)

Copper Tape

Silver Paint

Copper Wire

CNF/Epoxy

Conductive Epoxy

(b)
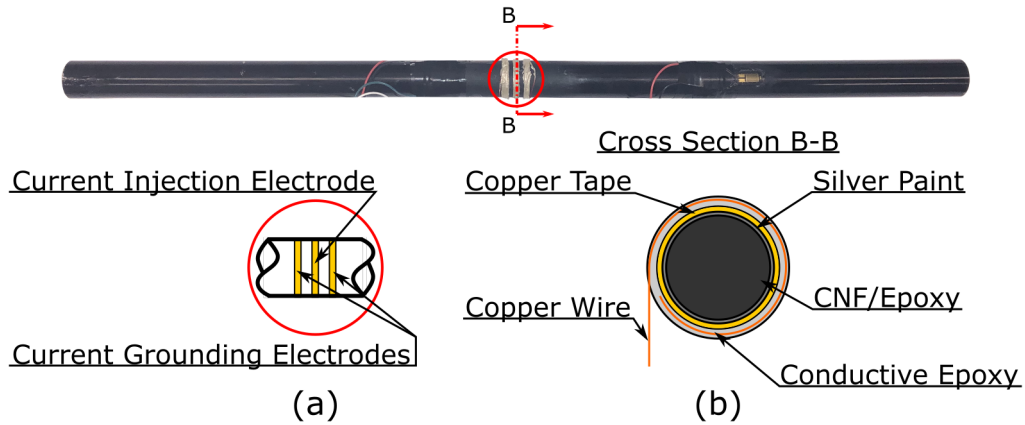
Figure 3.2. (Top) Three electrodes are formed on the surface of manufacturer nanofiller-modified rods to observe transmitted high-rate elastic stress waves and steady-state vibrations from the center of the rod. (a) A simplified schematic detailing the electrode configuration with respect to current injection and grounding. (b) A cross-sectional view reveals the specific layering sequence to create the electrodes through an embedded copper wire in conductive epoxy.

Controlled Wave Packet Excitation

The electrodes on the rods for wave packet injection were prepared using a comparable procedure to the impact rods. The rod surfaces underwent light sanding followed by a thorough cleaning using acetone, and Kim wipes to remove residual particulates. Then the circumferential surface of the rod was covered with painter's tape before being etched, about the circumference, at 6.35 mm intervals along the length of the rod. Alternating segments of the etched tape were removed to expose the surface of the nanofiller-modified epoxy rod. The exposed surfaces were then painted with a layer of quick-drying silver paint. Next, a layer of 6.35 mm wide copper tape was applied on top of the dried silver-painted surfaces to form electrodes. Finally, a second layer of copper tape was applied and formed into electrode tabs to facilitate easy connection with alligator clips with external electrical equipment.
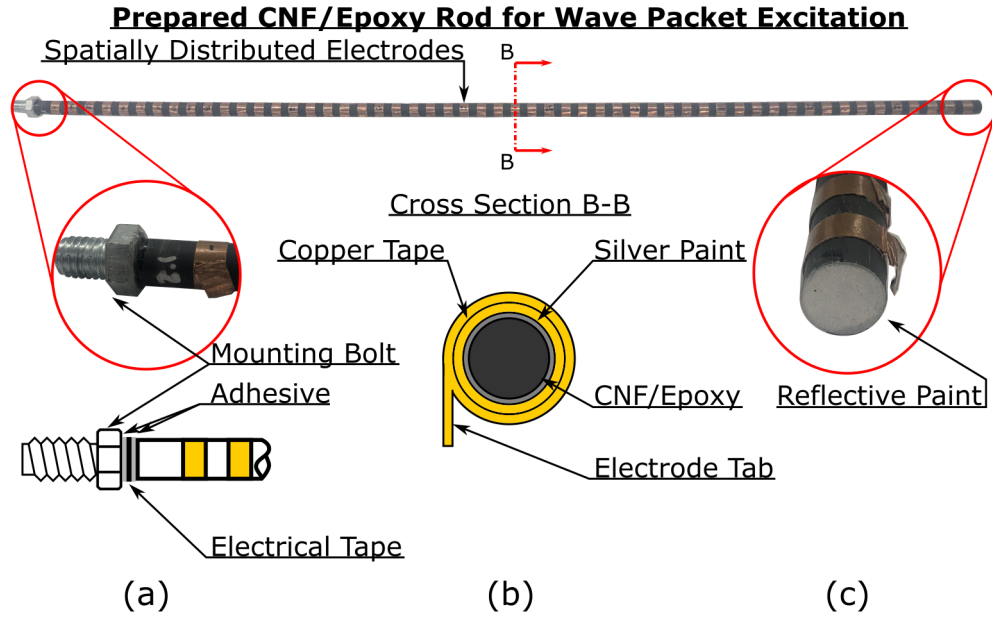
Figure 3.3. (Top) Electrodes are formed on the surface of manufactured CNF/epoxy rods with copper tape. The electrodes are spatially distributed with equidistant spacing along the length of the rod. (a) A simple schematic showcases the mounting configuration, (b) the specific layering sequence of specimen/silver paint/copper tape to form electrodes, and (c) the prepared reflective surface at the end of the rod for laser vibrometry.

3.2 Experimental Setup

3.2.1 Split–Hopkinson Pressure Bar

The SHPB [96] [97] [98] is an experimental apparatus that facilitates dynamic material characterization using uniform one-dimensional stress waves at strain rates ranging between $10^2 - 10^4$ s^{-1}. Conventional SHPB tests employ four bar components: 1) striker bar, 2) incident bar, 3) transmission bar, and 4) momentum bar. A pneumatic gas gun ejects the striker bar to impact the incident bar. The compressive stress wave created from the striker impact travels the length of the incident bar and is injected into the specimen. The compression wave passes through the specimens and builds in intensity as it reflects between the specimen-incident bar and specimen-transmission bar interfaces. If the specimen has a mechanical impedance mismatch with the bar components, then each interaction at the interfaces produces a reflected and transmitted wave [99] [98]. In this situation, strain gages

on the incident and transmission bars observe the transmitted and reflected waves. The momentum bar serves to "catch" the transmission of the stress waves and separates from the transmission bar to prevent secondary reflections from the end of the SHPB system. A momentum trap arrests the movement of the momentum bar. The profile of the incident wave can be "shaped" by employing a sacrificial component called a pulse shaper. Pulse shapers modify the shape of the indecent wave to produce a constant strain rate within the specimen [100].

SHPB Mechanical Characterization
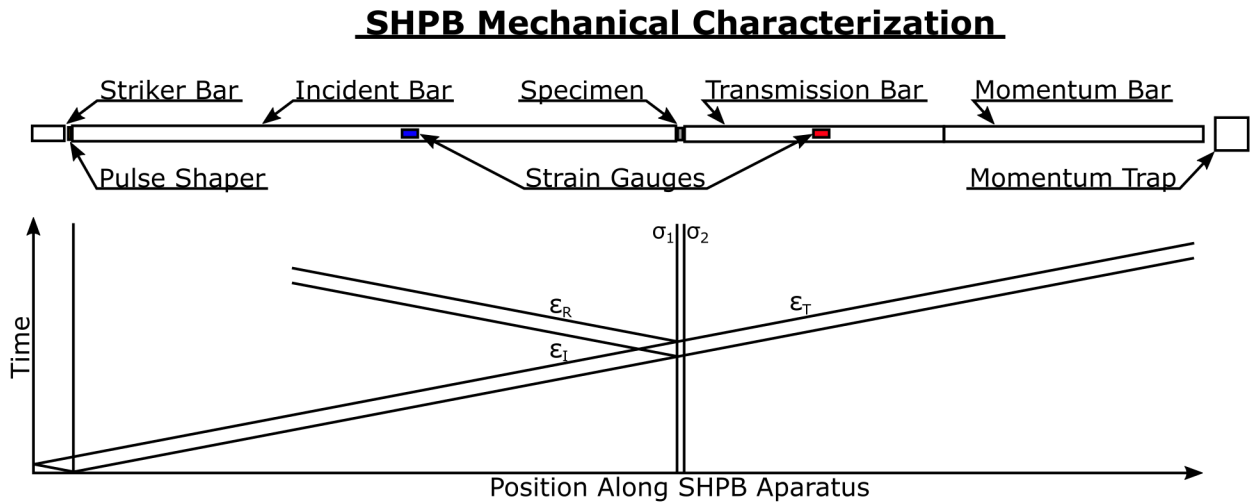
Figure 3.4. (Top) A SHPB apparatus consists of four bar components: a striker, incident, transmission, and momentum bar. A pulse shaper can be used to modify the profile or shape of the stress wave. Strain gages adhered to the surfaces of the incident and transmission bar assess the dynamic behavior of the specimen. (Bottom) A representative space-time plot showcases the stress wave's propagation and reflection along the length of the SHPB apparatus.

When the SHPB is properly aligned and calibrated, the dynamic strain recorded by the strain gages on the incident and transmission bar components is equivalent to the strain experienced by the specimen. The dynamic stresses measured at the specimen-incident, $\sigma_1(t)$, and specimen-transmission bar, $\sigma_2(t)$, interfaces are given by,

$$\sigma_1(t) \quad = \quad \frac{A_B}{A_S} E_B \left(\epsilon_I(t) + \epsilon_R(t) \right) \tag{3.1}$$

$$\sigma_2(t) \quad = \quad \frac{A_B}{A_S} E_B \epsilon_T(t) \tag{3.2}$$

Where the parameters A_B and E_B refer to the cross-sectional area and elastic Young's modulus of the bar components, while A_S denotes the cross-sectional area of the specimen, and strains are measured on the incident and transmission bars via surface-mounted strain gages. The strains $\epsilon_I(t)$, $\epsilon_T(t)$, and $\epsilon_R(t)$ denote the response from the surface-mounted strain gages on the bar components in response to the initial propagation of the incident stress wave, its propagation into the transmission bar after interacting with the specimen, and the reflection of the stress wave from the incident bar-specimen interface, respectively. The average strain rate, $\dot{\epsilon}(t)$, engineering strain, $\epsilon(t)$, and engineering stress, $\sigma(t)$, can be assessed through the mean of the strains and stresses at the specimen-bar interfaces. Where C_B is the wave speed of the bar components and L_S is the specimen length or thickness.

$$\dot{\epsilon}(t) \quad = \quad \frac{C_B}{L_S} \left(\epsilon_I(t) - \epsilon_R(t) - \epsilon_T(t) \right) \tag{3.3}$$

$$\epsilon(t) \quad = \quad \frac{C_B}{L_S} \int_0^t \left(\epsilon_I(t) - \epsilon_R(t) - \epsilon_T(t) \right) dt \tag{3.4}$$

$$\sigma(t) \quad = \quad \frac{1}{2} \frac{A_B}{A_S} E_B \left(\epsilon_I(t) + \epsilon_R(t) + \epsilon_T(t) \right) dt \tag{3.5}$$

To ensure the validity of the previous equations, dynamic equilibrium must be satisfied within the specimen. To address this, let $R(t)$ define the homogenization ratio as a means to quantify dynamic equilibrium. This is achieved by taking the quotient of the stress gradient with respect to the mean stress across the specimen. If the homogenization ratio is less than 5%, then equations (3.3)–(3.5) can be simplified via $\epsilon_T(t) = \epsilon_I(t) + \epsilon_R(t)$ [98]. Put differently, if the stress gradient within the specimen is sufficiently negligible compared to the mean stress, the transmitted strain can be considered equal to the incident and reflected strains,

essentially enforcing the stress at the specimen interfaces are equivalent, $\sigma_1(t) = \sigma_2(t)$. Once equilibrium is achieved, the determination of the material's dynamic response is possible.

$$R(t) \quad = \frac{1}{2}\left[\frac{\sigma_1(t)-\sigma_2(t)}{\sigma_1(t)+\sigma_2(t)}\right] \tag{3.6}$$

The SHPB bar components were precision-machined from VascoMax©350 Maraging steel to a diameter of 25.4 mm. The length of the incident bar measures 1.34 m while the transmission and momentum bars each measure 1.52 m in length. The work herein employed two striker bars, each serving a specific purpose. The first striker bar, with a length of 76.2 mm was utilized to produce an elastic wave that is fully contained within the long 505 mm length rods to observe distinct tension or compression phases of the reflecting waves. The second striker bar, with a length of 609.2 mm, was utilized to conduct a traditional SHPB test on small short aspect ratio cylindrical nanofiller-modified epoxy specimens for dynamic mechanical characterization purposes. VascoMax©350 Maraging steel is an elastic isotropic material with the following mechanical properties: Young's modulus of elasticity of 200 GPa, 8100 kg/m³ density, and a Poisson's ratio of approximately 0.30. Pulse shapers are placed between the incident bar and the striker bar and be used to tailor the profile of the stress wave introduced into the specimen. In the piezoresistivity investigation, small copper disks with a diameter of 6.35 mm and thickness of 0.7 mm were used to shape the stress wave pulse into a triangular stress wave with a well-defined shape and peak. For the dynamic mechanical characterization of the material itself, small copper disks with a diameter of 3.97 mm and 0.5 mm thickness were employed to transform the stress wave pulse to exhibit a bilinear profile and produce a uniform stress state within the short cylinder samples. The strain gages on the incident and transmission bars are positioned at distances of 1.5 m and 0.75 m, respectively, from the interface where the specimen is located.

Appropriate alignment is crucial for the bar components in the SHPB apparatus to produce purely planar one-dimensional stress waves. The calibration process ensures the proper alignment of the SHPB apparatus by verifying the uninterrupted propagation of an incident stress wave through all the bar components without any detected reflections from
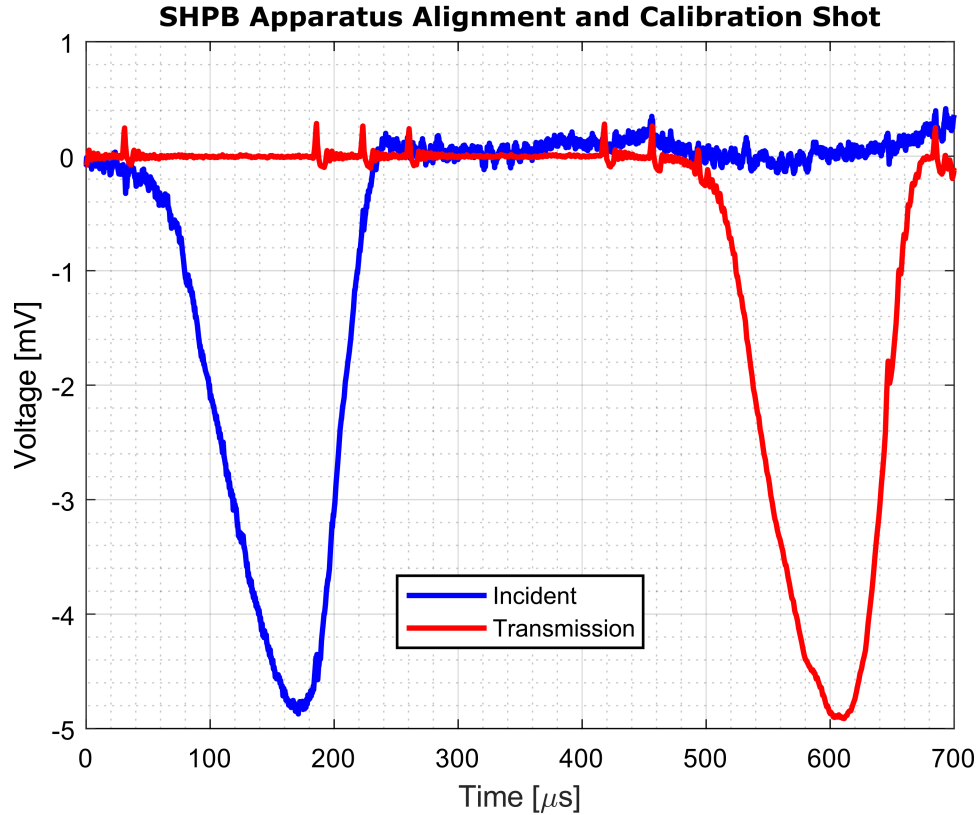
Figure 3.5. Voltage history of the incident and transmission bar strain gages observing a calibration shot using a representative triangular stress wave. Calibration of the SHPB apparatus involves observing the propagation of a stress wave across the incident/transmission bar interface. Reflections recorded by the incident bar strain gage or a significant change in the profile amplitude of the transmitted stress wave will denote misalignment. Shown here is a properly aligned SHPB apparatus.

the strain gages. Applying petroleum jelly at the bar interfaces can help aid in the complete transfer of energy transfer between bar components. While the utilization of petroleum jelly is beneficial in enhancing the transmission of stress waves at the interfaces of the bar components, it is crucial to emphasize that it should not be regarded as a replacement for precise alignment. This calibration process is done in the absence of a specimen at the bar interfaces, for example, a striker producing an incident wave with a triangular profile typically produced for the piezoresistivity investigation. For example, Figure 3.5 shows complete transmission, and the lack of a reflected stress wave on the strain gages on the incident bar indicates a well-align SHPB apparatus.

3.2.2 Steady-State and Wave Packet Vibration Excitation

Upon attaching electrodes to the nanofiller-modified rods, a steel bolt was affixed to one end of the rod with a piece of electrical tape separating physical contact between the bolt and rod specimen. Electrical tape was applied as a precautionary measure to mitigate the potential for electrical shorting through the shaker system, while the steel bolt served the purpose of securely mounting the rod to the shaker system, ensuring proper and stable positioning. This basic specimen mounting preparation and configuration established the means to utilize a model F4/F7 electromagnetic/piezoelectric shaker system (Wilcoxon Research, Frederick, MD, USA) to mechanically excite the prepared specimens through the bolted end with steady-state and wave packet vibrations as seen in Figure 3.6.

One-dimensional strain waves were induced at the bolted end of the nanofiller-modified rods. A range of frequencies on the order of $10^2 - 10^4$ Hz was investigated for steady-state vibration testing. The chosen excitation frequencies in this study do not aim to represent a specific application. Instead, the objective was to explore the potential of piezoresistive elastodynamics across a broad frequency range. Longer aspect ratio piezoresistive rods with a small cross-sectional area were manufactured, and electrodes were applied to the surface of the rods to provide spatially distributed sensing. The aim of this investigation was to explore the possibility of utilizing piezoresistive materials to track guided wave packets across the length of the rods and deduce any structural-level or mechanical state information, such as strain history. This enhanced investigation involved injecting nanofiller-modified rods with highly controlled 5.5-cycle modulated-wave packets with the modulated frequency in the structural vibration range (e.g., 26.5 kHz to 55 kHz).

3.3 Piezoresistive Measurements

In general, observing a nanofiller-modified material's piezoresistive response is uncomplicated. The deformation of a piezoresistive nanocomposite leads to changes in its electrical resistance, which can be detected as variations in the measured voltage under constant current conditions. The difficult aspect lies within the nature of capturing or observing this behavior during a dynamic experiment where a wave propagation phenomenon is expected to

occur. The following section outlines the specific techniques employed to take piezoresistive measurements in SHPB testing and controlled wave packet injection.

3.3.1 Split-Hopkinson Pressure bar

Two SHPB setups were employed to study nanofiller-modified epoxy rods' transient piezoresistive response. The initial set of experiments involved employing all the bar components within the SHPB apparatus. In this specific arrangement of the bar components, the incident stress wave remains in compression upon reflection at the specimen interfaces with the SHPB bar components. The second set of experiments involved removing or excluding the transmission bar from the SHPB apparatus. In this specific arrangement, one end of the nanofiller-modified epoxy rod is a free-end (the specimen end attached to the transmission bar). This interface serves as a free boundary condition that allows the stress wave propagating in the nanofiller-modified epoxy rod to reflect in the opposite sign (e.g., incoming compression wave reflected as a tension wave). Furthermore, the reflected tension wave will serve to self-separate the rod from the incident bar/specimen interface and contain the stress wave within the rod specimen. This will produce reflecting stress waves that alternate between compression and tension, which can be observed through the voltage measurements from the three surface-mounted electrodes via the piezoresistive effect. Increasing striker speeds were also considered for each series of experiments.

To ensure proper transmission of the incident wave and electrical isolation of the rod from the SHPB bar components, a thin layer of petroleum jelly and a single layer of electrical tape were applied to the interfaces between the SHPB bars and the nanocomposite rod. The combination of the three-electrode configuration on the nanofiller-modified epoxy rod (i.e., grounding the outside electrodes and injecting current in the middle electrode) and electrical tape at the interfaces of the specimens guarantees electrical current is injected into the electrode region. This approach mitigated the potential to produce an electrical short of the nanofiller-modified epoxy rod through the SHPB bars. To maintain the placement and alignment of the nanofiller-modified epoxy rod, a collar was 3D printed to fit around the SHPB bar and the nanocomposite rod specimens. Furthermore, a Precision 6221 direct

current source (Keithley Instruments, Cleveland, OH, USA) and infiniiVision MSOx3104T mixed-signal oscilloscope (Keysight Technologies, Santa Rosa, CA, USA) were employed to inject current and to measure voltage changes between electrodes due to stress waves passing underneath the electrode region due to stress waves passing underneath. The specific current injection amplitudes were carefully selected to leverage the maximum voltage offset and vertical scale precision of the Keysight Oscilloscope (i.e., 15 V and 50 mV/div). Furthermore, it is worth mentioning that carbon nanofiller-modified composites demonstrate linear current-voltage relationships when electron transport mechanisms primarily occur through direct nanofiller contact as opposed to electron tunneling behavior, as supported by references [101] [102] [103]. The data acquisition system of the SHPB utilized an MDO3014 mixed domain oscilloscope (Tektronics Inc., Beaverton, OR, USA) to record the bar instrumentation response and two DET10A Si photodetectors (THORLABS, Newton, NJ, USA) to determine the speed of the striker bar and serve as a trigger source to initialize the data collection window of the oscilloscopes.

3.3.2 Steady-State Vibration

Procedurally, a standalone waveform generator produces a sinusoidal output into a voltage amplifier before being transmitted to the shaker system and injected into the nanofiller-modified rod specimen. Piezoresistive measurements from the rod specimen were taken after steady-state conditions were established in the form of voltage history from a modified Wheatstone bridge circuit. The Wheatstone bridge circuit utilized the rod electrodes as a leg component, while a variable resistor was used to achieve a balanced initial configuration of the circuit. Changes in the resistance between the electrodes due to steady-state vibration will manifest as a change in voltage measured from the Wheatstone bridge circuit.

3.3.3 Wave Packet Excitation

The transient excitation of the nanofiller-modified epoxy rods was investigated through piezoresistive measurements between electrode pairs. The same shaker system utilized in the steady-state vibration investigation was employed with significant modification to account

for the increased experimental complexity. Procedurally, a trigger signal is transmitted from an infiniiVision MSOx3104T mixed-signal oscilloscope to a standalone waveform generator. Then the waveform generator transmitted the 5.5-cycle modulated-wave packet to the shaker system by means of a voltage amplifier. Finally, the force and accelerometer output of the shaker system were recorded by the data acquisition device of a PSV-500 laser vibrometer system (Polytec, Horsching, Austria), which also simultaneously measured the voltages from the nanofiller-modified rod specimen electrode pairs and the velocity of the rod at the tip through the laser scanning head. The decision to utilize an external trigger and waveform generator source was made due to the fact that appreciable cross-talk was found between the PSV-500 DAQ input channels and its internal waveform generator module. Therefore, a delay between sending the trigger signal and the transmission of the wave packet was implemented to eliminate this effect. This decision has a secondary benefit, allowing the previous injected wave packet to dissipate before the next wave packet was injected.

A two-point probe method was employed to inject constant current and measure the piezoresistive response of the rod in the form of recorded voltages. A separate isolated electrical circuit was employed to provide power to the Precision 6221 direct current source via a DC battery supply and DC-AC inverter. This isolated circuit provided the benefit of mitigating possible electromagnetic interference due to the power draw of the voltage amplifier. A total of six electrode measurement pairing schemes were employed to investigate the effect of electrode-spacing-induced mechanical filtering. This was achieved by adjusting the distance between the electrode measurement pairs. In this approach, 'adjacent' measurements denote voltage measurements were taken from the nanofiller-modified epoxy rod between electrode pairs directly next to each other. The electrode spacing number, n, denotes the number of electrodes between the driving electrodes. For example, $n = 1$, $n = 2$, and $n = 16$ indicate there are one, two, and sixteen electrodes between the two electrodes where current injection and voltage measurements are conducted. Thus, as n increases, the distance (and volume of material) between the measurement electrodes also increases. Due to the closed-loop nature of the experimental design, wave packets can be repeatedly injected into the rod while simultaneously collecting precisely timed data. Exploiting this fact, ensemble averaging [104] [105]

was applied to a total of 1024 separate measurements, taken from each electrode pairing, to increase the signal-to-noise ratio and quality of collected data dramatically.

3.4 Computational Modeling

Two sets of finite element models were also used in this thesis. The first set employed an ABAQUS explicit elastodynamic model of the rods employed in the wave packet excitation contribution to accurately simulate the applied transient deformation of the rod. The second set involved a steady-state diffusion model, which simulated the voltage-current relationship between the electrodes using the complete electrode model (CEM) framework. More specifically, the CEM was employed to determine an implicit relationship or geometric correction factor that accounts for the measured difference in resistance between surface-mounted and equivalent prismatic resistance measurements. The following subsection will outline the approach to computationally model the transient piezoresistive effect via finite element integration.

3.4.1 Analytical Piezoresistivity Model

The piezoresistive effect for self-sensing applications has attracted considerable attention to describing deformation-dependent conductivity changes. This thesis employs an analytical piezoresistivity model based on first-principle physics of electron transport properties initially outlined by Takeda et al. [106]. Tallman and Wang [61] [65] later expanded this work for finite element integration to investigate structure-property relationships in nanofiller-modified epoxy material systems.

$$\sigma_p = \sigma_m + \frac{4Pvl_f}{3\pi\lambda^2 d_f^2 \left[\frac{4l_f}{\pi d_f^2 \sigma_f} + \frac{h^2 t}{Ae^2\sqrt{2m\phi}} \exp\left(\frac{4\pi t}{h}\sqrt{2m\varphi} \right) \right]} \tag{3.7}$$

The analytical conductivity model, equation (3.7), relies on accurate material properties of the matrix and nanofiller material to predict nanocomposite conductivity, σ_p. This includes conductivity and density of the matrix material, σ_m and ρ_m, respectively. Additionally, the filler density ρ_f, filler conductivity σ_f, filler length l_f, filler diameter d_f, and

filler waviness ratio λ. Physical constants are also required for model calculations: Planck's Constant h, the potential barrier height φ, the mass of an electron e_m, and the charge of an electron e_c.

The analytical piezoresistivity model depends on a power law relation to predict the effect of arbitrary deformations on the percolation. Percolation probability is given by the power law relation $P = K(v - v_c)^\psi$ where K is the constant of proportionality given by $K = (1 - v_c)^{-\psi}$. The proportionality constant is carefully constructed to ensure the percolation probability is equal to one when the nanofiller volume fraction, v, equals the critical nanofiller volume fraction, v_c. The exponent of the power law relation is $\psi = 0.4$ for three-dimensional systems. Within an elasticity framework, the piezoresistive effect is a deformation-dependent phenomenon. Deformation is accounted for in the analytical piezoresistivity model through variations in the average inter-filler separation distance,

$$t = \gamma(\nu - \nu_c)^\beta \tag{3.8}$$

Where,

$$\gamma = A + \frac{B}{1 + \exp\left(-C\left(\frac{\nu}{\nu_c} - 1\right)\right)} \tag{3.9}$$

The expression for the average inter-filler spacing, equation (3.8), takes on a sigmoidal form through equation (3.9). This ensures the analytical piezoresistivity model maintains a smooth behavior across the critical volume fraction threshold, ν_c. The parameter values in the sigmoidal expression are in relation to the principal strain state: $A = \alpha(1 + \epsilon_1)$ and $B = \alpha(\epsilon_1 - \epsilon_3)$. The parameter C governs the behavior of the sigmoidal relation near the critical volume fraction. In this work, $C = 50$ was utilized. The parameters and β can be found through a curve-fitting process with experimentally collected conductivity data for specific material systems for a highly calibrated analytical piezoresistivity model.

3.4.2 Complete Electrode Model

The complete electrode model (CEM) consists of solving Laplace's equation, a second-order partial differential equation in n dimensions ($n = 2, 3$) for steady-state electrical

diffusion in a domain, $\Omega \subset \mathbb{R}^n$, with a smooth boundary and domain conductivity, $\sigma : \Omega \to \mathbb{R}^{n \times n}$. It should be noted that the CEM boundary conditions are not readily available in commercial solvers, so all diffusion code used in this thesis was written by the author in Matlab. Let Γ_E and Γ_N be two disjoint sets representing the domain boundary (i.e., $\partial\Omega = \Gamma_E \cup \Gamma_N$). Within the framework of the CEM, Γ_E refers to the boundary electrodes, whereas Γ_N denotes the domain boundary excluding the electrodes. A crucial assumption in equation (3.10) is that internal current sources are absent. It is important to note that index notation is used as a generalization according to the dimension of the problem, and summation is implied according to index variable pairs. Furthermore, the domain conductivity is expressed as a tensor to accommodate electrical anisotropy.

$$\frac{\partial}{\partial x_\mathrm{i}}\sigma_\mathrm{ij}\frac{\partial\phi}{\partial x_\mathrm{j}}\bigg|_\Omega = 0 \tag{3.10}$$

Above, ϕ is the domain potential. Consider the inclusion of boundary conditions on equation (3.10): Equation (3.11) represents the voltage drop between the electrodes and the domain due to contact impedance. This boundary condition incorporates the effect of the contact impedance or resistance between the assumed perfectly conducting electrodes and domain. Equation (3.12) enforces the conservation of charge through the electrodes involved in current injection and voltage measurement. In other words, the sum of the current injected into the domain through the current-driving electrodes must be equivalent to the current passing through all the electrodes attached to the domain. Furthermore, equation (3.13) states the domain boundary not involved with active current injection or voltage measurement is perfectly electrically insulating. In these equations, n_j, z_l, V_l, and E_l are the unit normal vector, contact impedance, the voltage of the l'th electrode, and the length or area of the l'th electrode (depending on the dimensionality of the problem), respectively.

$$\sigma_\mathrm{ij}\frac{\partial\phi}{\partial x_\mathrm{i}}n_\mathrm{j}\bigg|_{\Gamma_E} = \frac{1}{z_l}(V_l - \phi) \tag{3.11}$$

$$\sum_{l=1}^{L} \int_{E_l} \sigma_{\mathrm{ij}} \frac{\partial \phi}{\partial x_{\mathrm{i}}} n_{\mathrm{j}} dS_l \bigg|_{\Gamma_E} = 0 \tag{3.12}$$

$$\sigma_{\mathrm{ij}} \frac{\partial \phi}{\partial x_{\mathrm{i}}} n_{\mathrm{j}} \bigg|_{\Gamma_N} = 0 \tag{3.13}$$

The finite element method is a convenient tool to solve equations (3.10)–(3.13) through the discretization of the domain and electrodes. The CEM consists of four individual matrices, $\boldsymbol{A}_M$, $\boldsymbol{A}_Z$, $\boldsymbol{A}_W$, and $\boldsymbol{A}_D$. These matrices are succinctly expressed in equation (3.14) and their general finite element integration expressions denoted in equations (3.15)–(3.18). In this expression, $\boldsymbol{\Phi}$, $\boldsymbol{V}$, $\boldsymbol{0}$, and $\boldsymbol{I}$ represent the domain potential vector, the vector of voltages at the boundary electrodes, the vector of zeros, and the vector of injected currents, respectively.

$$\begin{bmatrix} \boldsymbol{A}_{\mathrm{M}} + \boldsymbol{A}_{\mathrm{Z}} & \boldsymbol{A}_{\mathrm{W}} \\ \boldsymbol{A}^{T}_{\mathrm{W}} & \boldsymbol{A}_{\mathrm{D}} \end{bmatrix} \begin{bmatrix} \boldsymbol{\Phi} \\ \boldsymbol{V} \end{bmatrix} = \begin{bmatrix} \boldsymbol{0} \\ \boldsymbol{I} \end{bmatrix} \tag{3.14}$$

$$A^{\mathrm{e}}_{M\ \mathrm{ij}} = \int_{\Omega_{\mathrm{e}}} \frac{\partial w_{\mathrm{i}}}{\partial x_k} \sigma_{kl} \frac{\partial w_{\mathrm{j}}}{\partial x_l} \ \mathrm{d}\Omega_{\mathrm{e}} \tag{3.15}$$

$$A_{Z\ \mathrm{ij}} = \sum_{l=1}^{L} \int_{E_l} \frac{1}{z_l} w_{\mathrm{i}} w_{\mathrm{j}} \ \mathrm{d}S_l \tag{3.16}$$

$$A_{W\ l\mathrm{i}} = - \int_{E_l} \frac{1}{z_l} w_{\mathrm{i}} \ \mathrm{d}S_l \tag{3.17}$$

$$A_{D\ l\mathrm{i}} = \mathrm{diag}\left(\frac{E_l}{z_l} \right) \tag{3.18}$$

In the finite element method (FEM), interpolation or basis functions are mathematical functions that are used to construct an assembly of elements that approximates the behavior of a continuum. Put into different words, a continuum can be discretized into elements using functions that can be used to interpolate behavior within an element that is approximately close to the exact solution. Equation (3.15) is utilized to construct i'th row and j'th column

of the stiffness diffusion matrix for e'th element in terms of basis functions, w. This work uses linear interpolation functions to discretize the domain into triangular or tetrahedral elements. Equations (3.16)–(3.18) originate from the boundary conditions above. These boundary conditions impose additional degrees of freedom due to the contact impedance of the electrodes and the current injection scheme. A more detailed derivation for these equations is presented in the Appendix.

3.5 Summary

This chapter describes the manufacturing techniques and testing methods employed in this thesis. Long prismatic nanocomposite rod structures were manufactured with three nanofiller types through a cast manufacturing method and characterized under dynamic loading conditions. The nanofillers utilized herein are CB, CNF, and MWCNT at various weights. The electrical and mechanical properties of the nanocomposite were measured during the injection of stress waves produced by SHBP striker bar impacts or highly controlled wavepackets generated through a piezo/electromagnetic shaker system. The next chapter presents the experimental results for each type of nanocomposite utilized in SHPB testing and controlled wave packet excitation as well as the results obtained by conducting a preliminary piezo-inversion of the collected data to estimate the strain-response history of the rods.
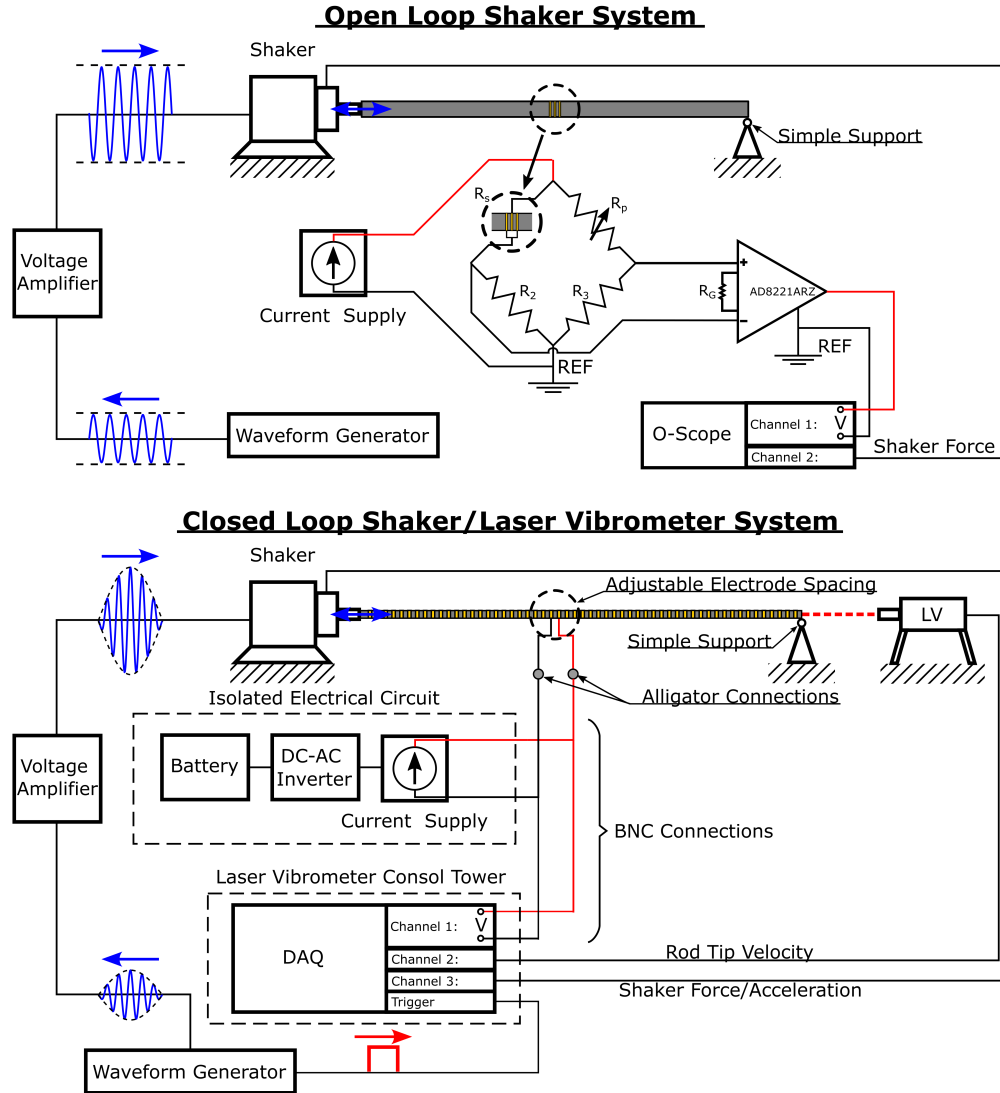
Figure 3.6. (Top) An open-loop system test arrangement was set up to investigate the piezoresistive behavior of a nanocomposite rod subject to steady-state sinusoidal excitation provided by an electromagnetic/piezoelectric shaker. The attached electrodes from the rod specimen were utilized as a leg within a Wheatstone bridge circuit. An AD8221ARZ circuit ($G = 1000$) was employed to magnify piezoresistivity-induced voltage changes. (Bottom) A closed-loop system test arrangement was set up to investigate the piezoresistive behavior of a nanocomposite rod subject to steady-state sinusoidal excitation behavior of a nanocomposite rod subject to small-amplitude wave packets. The piezoresistive behavior of the rod is examined across its length by adjusting the placement and spacing of the alligator connections to the surface-mounted electrodes. A laser vibrometer system was employed to measure and verify the transmission of the wave packets. Due to the closed-loop configuration of this setup, highly-repeatable measurements can be taken from the rod via the data acquisition system.

Nominal SHPB Apparatus
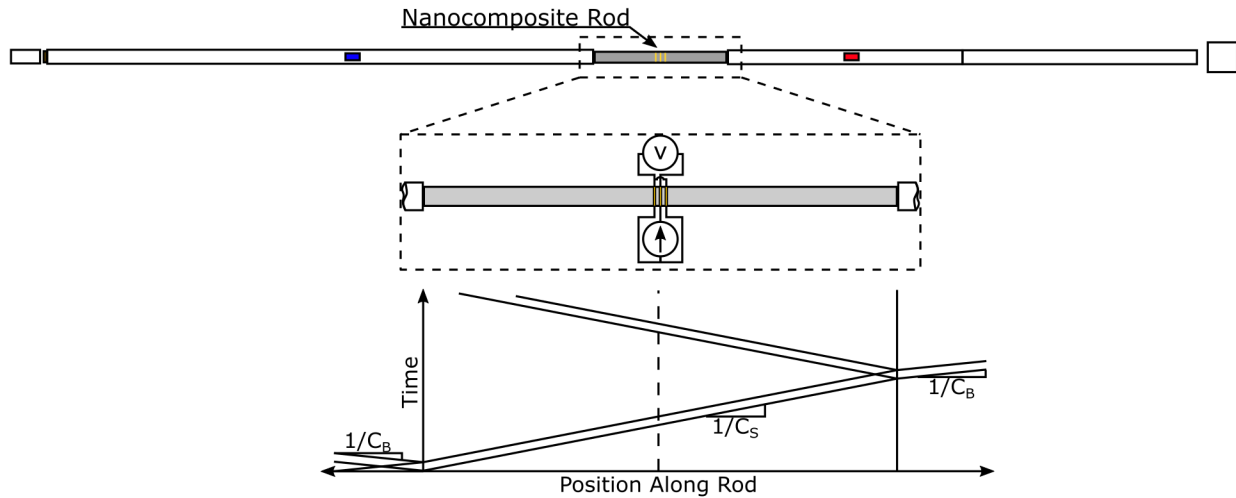
Modified SHPB Apparatus
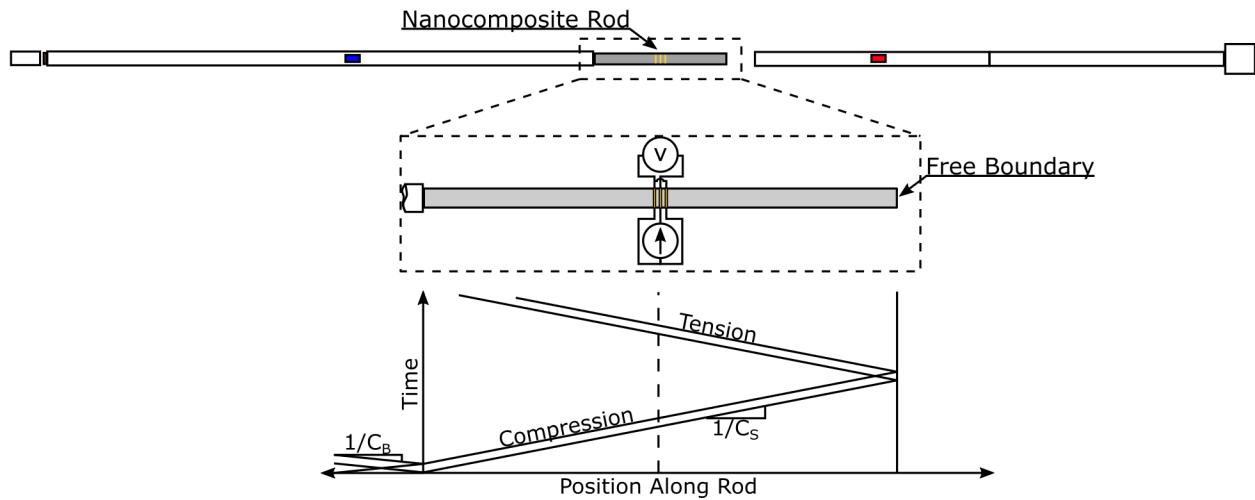
Figure 3.7. (Top) When all the components of an SHPB apparatus are employed, the stress wave transmitted into the nanocomposite rod will remain entirely in compression. Internal reflections will transmit a portion of the stress wave's energy into the bar components. (Bottom) When the transmission and momentum bar is removed or separated from the apparatus, the internal stress wave reflections will alternate signs between tension and compression due to the free boundary condition of the nanocomposite rod.

4. EXPERIMENTAL RESULTS AND ANALYSES

4.1 High Strain-Rate Impact Testing

4.1.1 SEM Imaging of Manufactured Nanofiller Material

Nanocomposite rods were manufactured using three different types of nanofillers: CB, CNF, and MWCNT. Sample material underwent cryogenic fracturing, followed by the application of an atomic layer coating of platinum. Representative scanning electron microscopy (SEM) images of the produced material were taken by a ThermoFisher Teneo System at various magnifications, as seen in Figure 4.1.

4.1.2 Stress Wave-Induced Piezoresistive Behavior of Rods

Monitoring the piezoresistive behavior of the nanofiller-modified epoxy rods while subject to transient elastic wave loading was conducted by applying a constant current and measuring the changes to inter-electrode voltages. When all the components of the SHPB apparatus are utilized, as seen in Figure 3.7 (top), it produces the effect of maintaining the compressive state of the stress wave transmitted into the nanocomposite rod. Due to this, examining the piezoresistive behavior of the rod while experiencing stress wave reflections that are only in compression is possible. This behavior is due to the mechanical impedance mismatch between the rod specimen and the SHPB components [96][98][99]. However, each reflection will result in a loss in the stress wave amplitude as a portion of the reflected wave's energy will be lost to transmissions into the SHPB components. In the next series of experiments, where the transmission bar is decoupled from the nanocomposite rod, as seen in Figure 3.7 (bottom), the absence of the transmission bar creates a free-end for the stress wave to reflect

Material	Electrode Resistance	Current Magnitude	Electrode Voltage
CB/Epoxy	71.33 kΩ	210 μ A	14.98 V
CNF/Epoxy	882.9 Ω	14 μ A	15.01 V
MWCNT/Epoxy	10.71 kΩ	1.41 μ A	15.10 V

Table 4.1. Initial inter-electrode resistance, current magnitude, and resulting voltage across the measurement region.
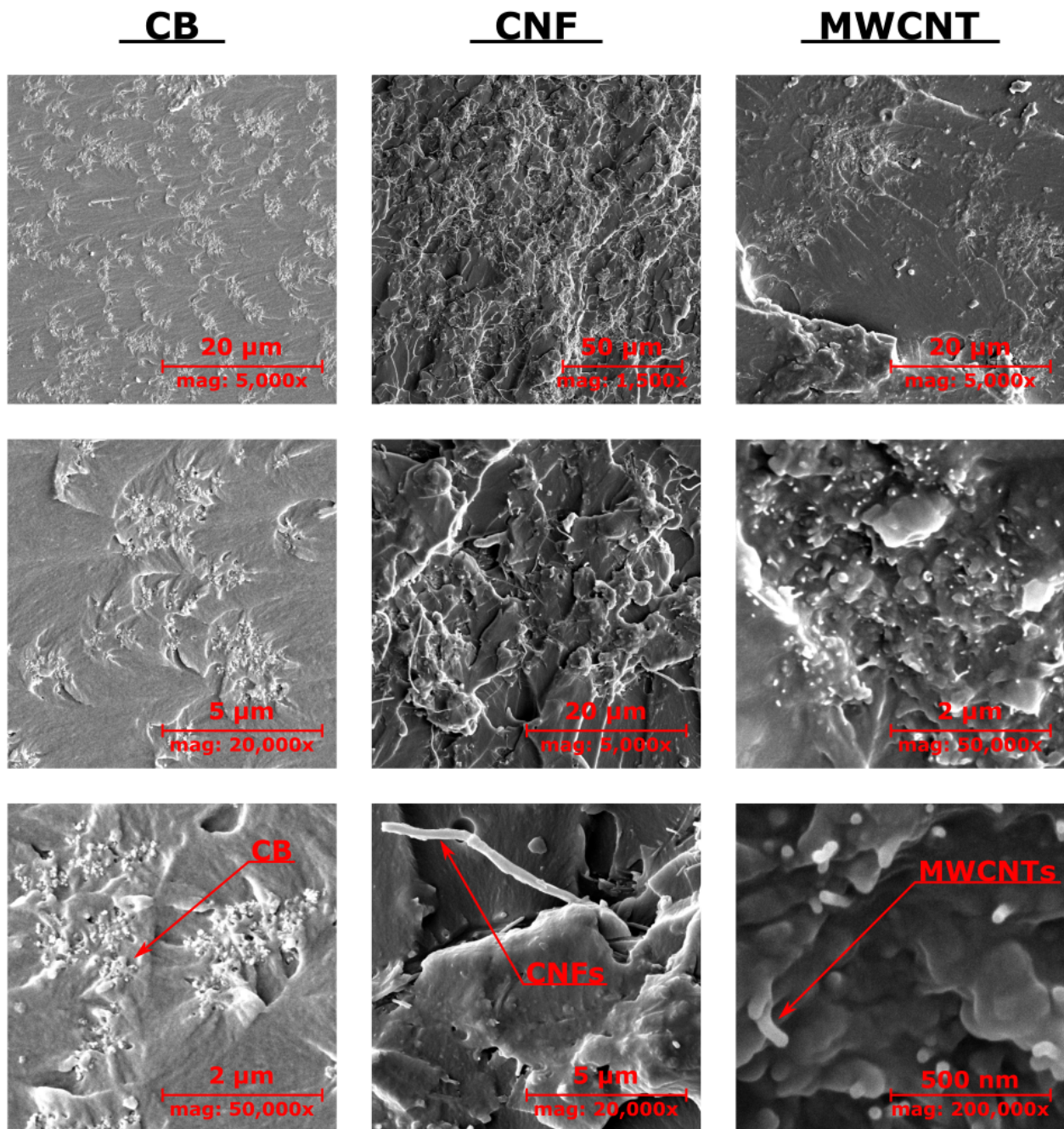
Figure 4.1. SEM images revealed the representative morphology of CB (left column), CNF (center column), and MWCNT (right column) nanofillers. The lowest magnification (top row) demonstrates that ultrasonication is an effective method of distributing carbon nanofillers within an epoxy material system. At the highest magnifications (bottom row), each nanofiller's distinct physical morphology or geometrical characteristics are readily apparent.

in the opposite sign (i.e., incoming compression into reflected tension). For the second pass, the tension stress wave serves to physically decouple the nanofiller-modified epoxy rod from the SHPB apparatus and fully contain the transmitted stress wave within until the specimen material completely absorbs its energy.

The piezoresistive response of nanocomposite rods made with CB, CNF, and MWCNT was determined by continuous voltage measurements between the electrodes under constant current conditions. The piezoresistive response was calculated as a percent change in resistance as the stress wave passes, as shown below. The baseline resistance of rods between the electrodes is collected in Table 4.1.

$$\frac{\Delta R}{R_0} = \frac{R(t) - R_0}{R_0} \cdot 100\% \tag{4.1}$$

The piezoresistive behavior of the impacted rods is presented in Figure 4.2, showcasing several interesting observations that merit examination. First, the triangular stress wave was clearly captured as the loading passed through the electrode measurement region in the piezoresistive rod for the three types of nanofillers used in this investigation. The time between successive peaks in the observed piezoresistive behavior will later be shown to correlate to the elastic speed of sound for the material system. This observation is noteworthy as it demonstrates piezoresistivity can be used as a tool for real-time tracking of elastic waves in self-sensing materials. Second, the profile of the normalized resistance change curves for each of the nanocomposite rods closely approximates the characteristics of the injected stress wave. Recall copper disks were utilized as pulse shapers to modify the incident stress wave to have a bilinear or triangular profile. This observation provides significant evidence for the piezoresistive effect to recover precise wave features under dynamic or transient conditions, such as shape or profile. Third, the sign of the wave can be discerned in terms of tension or compression stress states. Recall when all the components of the SHPB apparatus are employed, the stress waves reflecting inside the nanocomposite rod specimens are purely compressive in nature. This is reflected by periodic decreases in the relative resistance measurements taken at the electrodes, as seen in Figure 4.2. This distinction is made possible by a well-known feature of *positive* piezoresistivity, where the average inter-nanofiller distance
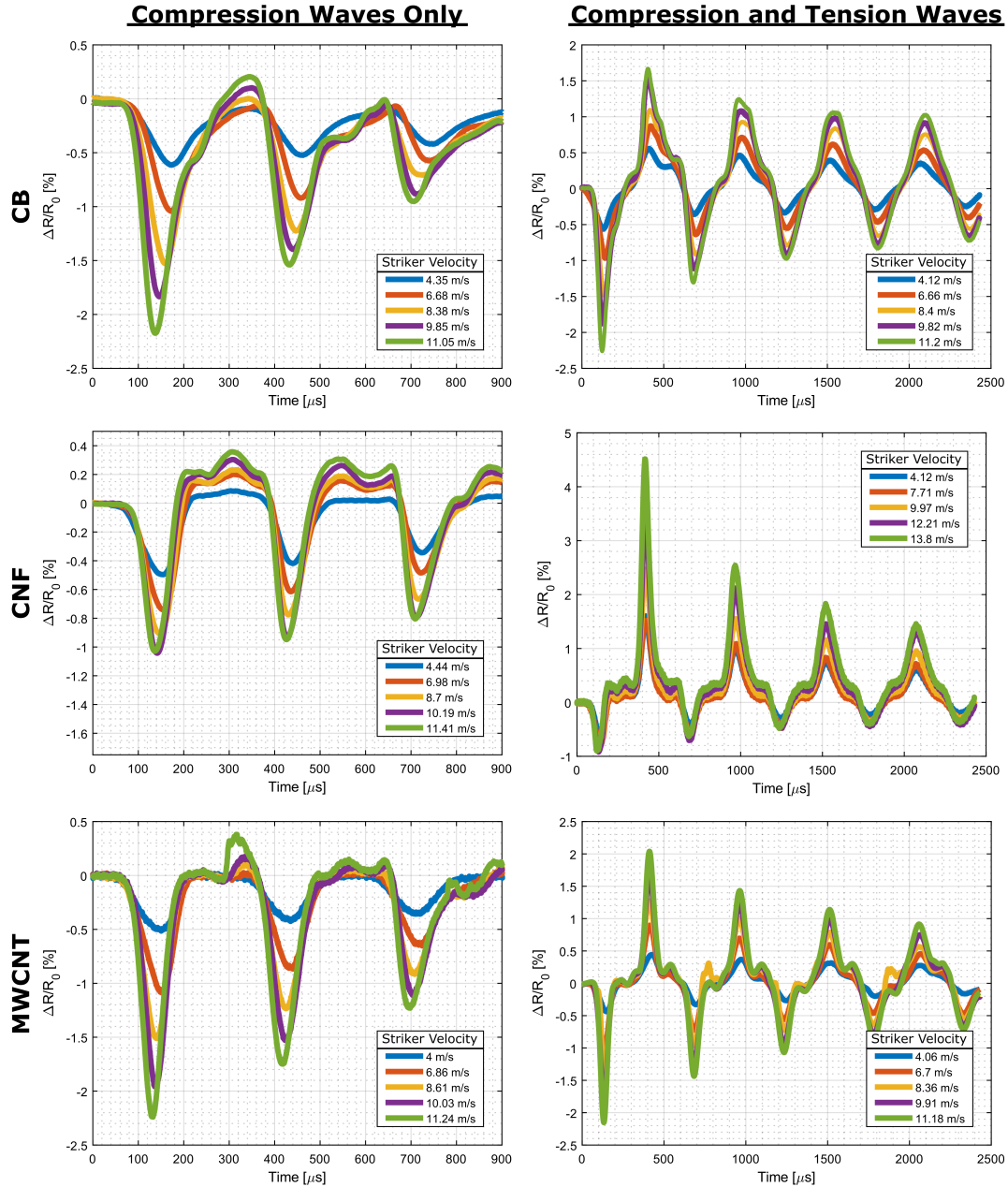
Figure 4.2. The piezoresistive effect in response to transient elastic stress wave propagation is measured at the mid-span of the nanofiller-modified epoxy rods. Piezoresistive behavior is reported as normalized resistance changes. Left column: All components of the SHPB apparatus produce purely compressive stress wave reflections within the rod, which is observed as periodic decreases in resistance measurements when the stress wave travels under the electrode region. Right column: Disconnecting the transmission bar (e.g., a modified SHPB apparatus) results in stress wave reflections within the specimen rod alternating between compression and tension. Piezoresistive measurements clearly indicate this behavior with alternating decreases and increases in resistance measurements.

decreases or increases under compression or tensile deformation. This results in a respective decrease or increase in the resistance experienced by electrons which in turn is reflected as measurable changes in bulk electrical properties. In contrast, *negative* piezoresistivity [107] [108] [109] manifests (in rare circumstances) as increases or decreases in electrical resistivity in response to compression or tensile loading, respectively. In the modified SHPB apparatus setup when the transmission bar is physically detached from the specimen, the injected stress wave will alternate between compression and tension. The behavior is clearly shown in the right column of Figure 4.2. Again, this matches the expectation that positive or negative resistance measurements can be used to deduce the stress wave sign. This capability may be particularly important for assessing the likelihood of damage in composite materials due to unknown dynamic loading. Fourth, the magnitude of the measured resistance changes appears to decrease with time. This is suspected to be due to the overall energy of the stress wave also decaying with time, thereby producing a lower strain magnitude and, consequently, a diminished piezoresistive response. And fifth, there is an evident positive relationship between piezoresistive measurement amplitude and striker impact velocity. This is sensible as striker impact velocity and strain are proportional and can be observed through piezoresistive measurements. This may be a useful method to determine the energy or velocity of unknown impactors.

The preceding discussion outlines observations from the experimental data collected. The following discussion delves into a deeper examination of the collected data to garner greater insights into the material behavior of the nanocomposite rods. Specifically, we consider i) the speed of sound in the material, ii) the decay of stress wave magnitude, and iii) striker velocity in the following discussions.

Elastic Wave Speed Determination

Given that the piezoresistive effect is a phenomenon that depends on local deformations (i.e., local strains), the elastic wave speed can be determined by analyzing the resistance measurements at the electrodes. With this in mind, the elastic speed of sound can be calculated by taking into account the time elapsed when the wave passes directly underneath

the electrode region and the total distance traveled by the wave. Revisiting Figure 4.2, the time elapsed between wave passes is defined as the time separation between the maximum peak amplitudes of relative resistance measurements. On account of the electrode region being at the mid-span of the specimen, the total distance traveled by the wave is equivalent to the overall length of the nanocomposite rod. This is because after the wave passes under the electrode region of the rod, the wave must then travel to and reflect from the interfaces of the specimen/bar before being measured again. The size of the measurement window to record compression-only reflections was limited to three to avoid constructive interference from a re-transmission of the reflected wave from the incident bar.

In contrast, the modified SHPB apparatus (with the transmission bar detached from the specimen) allowed for a larger investigation window due to the fact the rod entirely captured the transmitted wave. In other words, lacking concern for the injection of reflected waves from the SHPB bar components into the specimen enabled capturing the piezoresistive response from the rod for a longer duration of time and subsequently observing a greater number of wave reflections between tension and compression stress states. The speed of sound is then calculated as the ratio of the distance traveled by the strain wave to the elapsed time between determined resistance peaks. As shown in Chen et al. [98], the piezoresistivity-predicted speed of sound can be validated via the SHPB from the compression-only experiments by using the measured peaks in the strain gauge voltage response of the incident (t_I) and transmission (t_T) bar signals with the following expression.

$$C_{rod} = \frac{L_S}{(t_T - t_I) - \left(\frac{L_I + L_T}{C_B}\right)} \tag{4.2}$$

Where C_{rod} is the calculated speed of sound of the nanofiller-modified epoxy rod. The parameters L_I and L_T are the distances of the strain gages on the incident and transmission bars to the bar/specimen interfaces. The piezoresistivity-predicted speed of sound and elastic speed of sound, as determined by the SHPB strain gage components, are presented in Table 4.2.

Nanofiller Type	Piezoresistivity Predictions		SHPB Validation
	Compressive Loading	*Alternating Loading*	
CB	1723.9±125.9 m/s	1772.4±61.8 m/s	1782.1±18.8 m/s
CNF	1757.5±57.9 m/s	1787.7±67.5 m/s	1763.3±14.0 m/s
MWCNT	1781.6±59.8 m/s	1786.5±37.0 m/s	1755.1±17.4 m/s

Table 4.2. The elastic wave speed was predicted from piezoresistivity measurements on a nanofiller-modified epoxy rod for various nanofiller types and for two loading conditions: 1) Compression-only and 2) Alternating compression and tension. Predictions were validated through the SHPB apparatus using the strain gages on the incident and transmission bars. It can be seen that there is good agreement between piezoresistivity predictions and SHPB validations. This indicated piezoresistivity may be a useful tool to assess the time of flight of propagated stress waves transmitted into nanocomposite structures.

Decay of Stress Wave Magnitude

Next, successive passes of the stress wave are considered in relation to the decay in amplitude in the collected piezoresistive measurements. Under purely compressive loading, the stress wave propagates along the bar components until it encounters an interface. At the specimen/SHPB component interface, a portion of the stress wave's energy is transmitted into the SHPB components and reflected back into the specimen. As a result, each reflection results in an appreciable loss in the stress wave intensity that is observed as a reduction of the stress wave amplitude. In relation to the piezoresistive effect, a reduced stress wave amplitude will produce a similar (but nonlinear) reduction in the change of resistance after each reflection, as seen in the left column of Figure 4.3. In the second loading condition, where there are no losses into the SHPB components and the reflections alternated between compression and tension stress states, observed decreases in amplitude in the piezoresistive measurements can be attributed to the damping or attenuation behavior of the nanofiller-modified epoxy material itself. Illustrated in Figure 4.3, the extracted maximum and minimum amplitude values for each nanofiller type and striker velocity are plotted with respect to the number of times the stress wave passes under the electrode region. The maximum and minimum amplitude values correspond to the peaks of the stress wave under tension and compression. Several noteworthy observations can be made by visualizing the decay of the stress wave magnitude in this way. First, the magnitude changes in normalized resistance measurements decrease with increasing time. This is attributed to the damping or attenuation behavior of the material system. Second, examining the case of alternating compression and tension waves more closely, the resistance change magnitude due to tension is greater than that of compression. This agrees with a well-established understanding of piezoresistive behavior in nanocomposites; piezoresistivity exhibits greater sensitivity in tension than in compression due to the highly nonlinear behavior of electron tunneling resistance [110] [65]. A third interesting observation pertains to the qualitatively similar responses of MWCNT and CB-modified epoxy rods in purely-compression loading and alternating loading conditions. It can be seen the behavior of these two nanofiller systems produces approximately equal piezoresistive response magnitudes due to the traveling

stress wave. However, the CNF-modified epoxy rod produces a distinctive response. In the alternative SHPB apparatus configuration, the CNF/epoxy rod exhibits a decay of the stress wave magnitude from a piezoresistivity standpoint, but this decay is of much lesser magnitude than the tensile curve. The exact cause of this distinction is unknown, but one possible explanation for this behavior may involve the method of nanofiller dispersion. The authors speculate the CNF nanofillers were dispersed into epoxy more effectively than the MWCNT and CB nanofillers. As a consequence, the change in resistance magnitude is attributed to greater electron tunneling between individual CNF particles as opposed to between agglomerations. Alternatively, the total quantity of energy from ultrasonication may have served to sever and reduce the aspect ratio of fragile MWCNTs and produce a conductive nanofiller matrix that is comparable to one made from CB nanofillers. A more careful examination of these hypotheticals is necessary to understand this result.

Striker Velocity

Next, the relationship between striker velocity and the observed magnitude of resistance change is explored. In order to isolate this behavior, the magnitude of the first measured resistance change from Figure 4.2 is extracted and plotted as a function of impactor velocity, as seen in Figure 4.4, for both loading cases of only-compression and alternating stress states. In both loading cases, the first wave pass through the electrode region was in a compressive state, thereby allowing us to assess the repeatability of these observations. The alternate presentation of the data leads to several important observations. First, a positive correlation exists between resistance change magnitude and striker velocity. Higher striker velocity generates stress waves with larger amplitudes. Due to the fact the piezoresistive effect is a deformation-driven phenomenon, greater amplitude stress waves will deform the nanofiller epoxy material more significantly and produce a larger measurable local change in electrical properties and hence greater changes in inter-electrode resistance measurements. Second, the resistance change magnitude is approximately the same for both cases of pure-compression waves and alternating stress wave states. This suggests piezoresistivity is a potential method to determine unknown impact velocities reliably. Importantly, this also
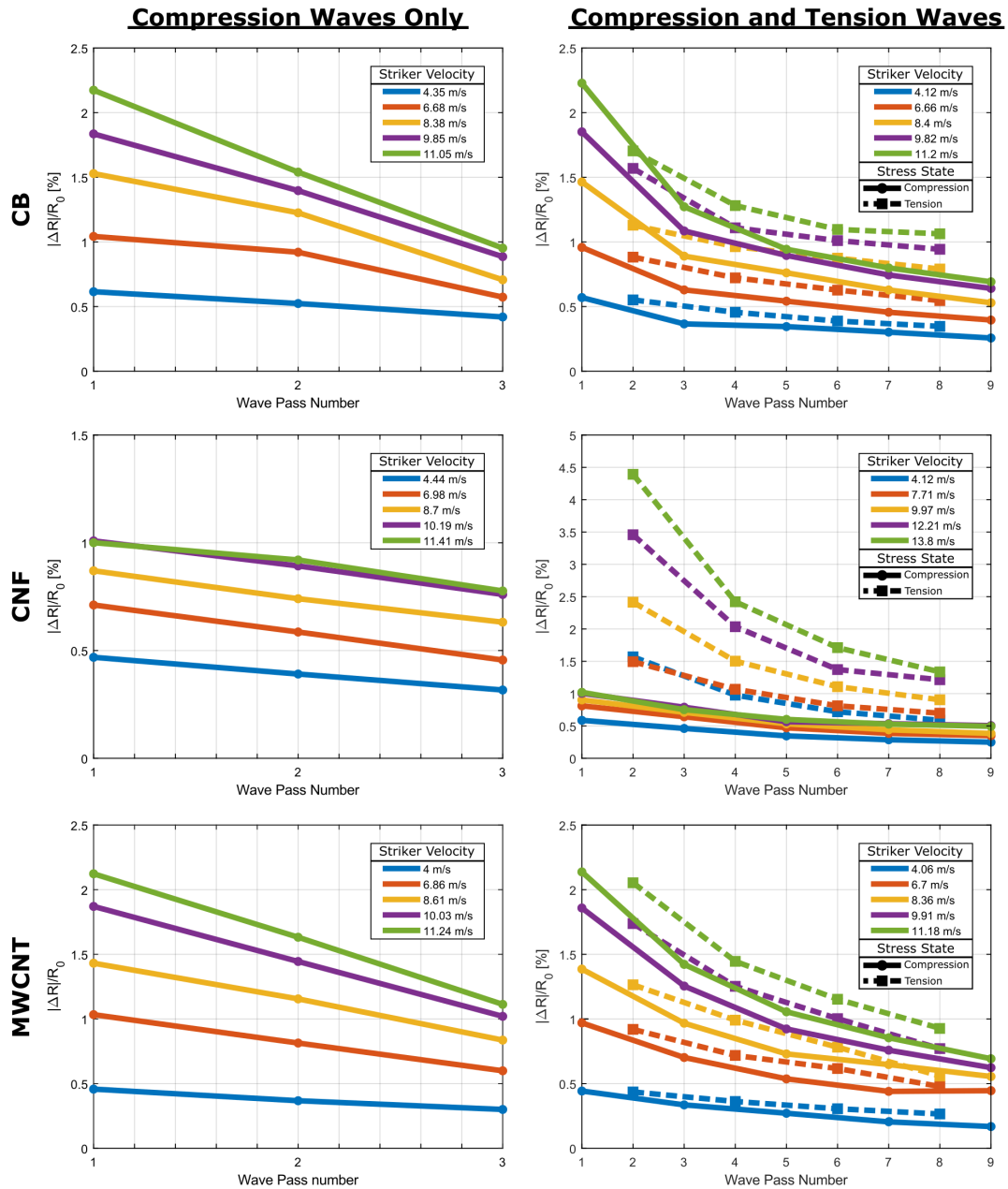
Figure 4.3. The maximum amplitudes of the raw piezoresistivity data collected from the rods are presented as a function of the increasing number of wave passes. (Left) The valleys (or maximum change in relative resistances) are extracted from the compression-only testing. (Right) The second loading condition produces alternating compression and tensile loading, which manifests as valleys and peaks in the collected data. The decay in amplitude is plotted for the compression and tension waves as solid and dashed lines, respectively, for increasing striker velocity.
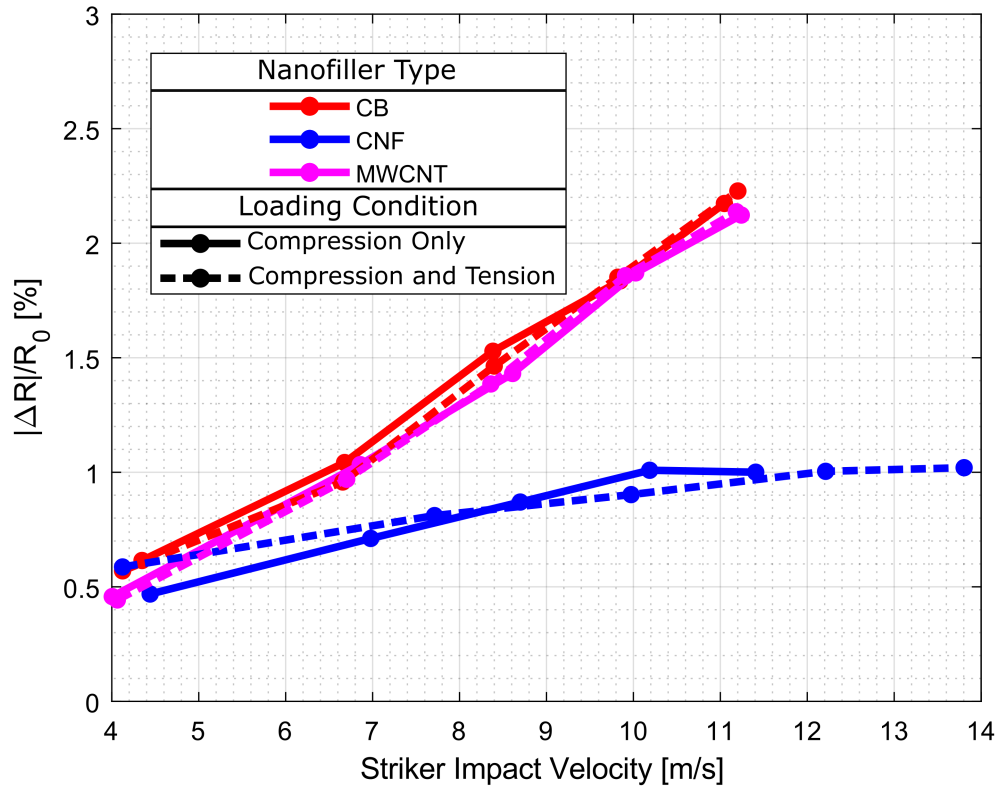
Figure 4.4. The magnitude of the piezoresistive response for the first pass of the stress wave under the electrode region in the nanofiller-modified epoxy rods are compared against increasing striker velocity. It can be seen there is a positive correlation between striker impact velocity and piezoresistive measurement magnitude.

confirms that the loading is indeed in the elastic regime since the observed responses are repeatable. Building upon the second observation, the third observation concerns the apparent flattening effect of piezoresistive behavior for striker velocities greater than 10 m/s. This saturation of piezoresistive behavior is speculated to be a consequence of increasing compression magnitude beyond a certain threshold and does not produce appreciable changes in material conductivity. This is a physical consequence of nanofiller movement where adjacent nanofillers being pushed together indefinitely do not yield measurable changes in the resistance of the conductive network as been observed in literature for cases for infinitesimal strain regime [110] [111] [112] [113].

4.1.3 Dynamic Mechanical Characterization of Nanocompsites

Leveraging the full capabilities of an SHPB experimental apparatus, conventional experiments were conducted to obtain the dynamic mechanical properties of the nanofiller-modified epoxy material. According to Chen et al. [98], conventional SHPB experiments require careful design of the incident stress wave to produce constant strain-rate deformation and stress equilibrium within specimens for dynamic mechanical characterization. The specimen, striker bar, and pulse shaper dimensions are described in the experimental procedures section of this thesis. A total of 35 specimens were tested per nanofiller type. The mean and standard deviation of the stress histories from the incident and transmission bar is presented in Figure 4.5 for MWCNT-modified epoxy. These responses are very similar regardless of nanofiller type, and low standard deviation values indicate good repeatability was achieved. The stresses on both ends of the specimen were directly compared to assess the dynamic stress equilibrium. Equations (3.1) and (3.2) were evaluated using the measured strains from the SHPB bar components and directly compared (the green and blue curves in Figure 4.5, respectively). Second, a homogenization ratio, $R(t)$, was calculated to quantify the stress variation across the specimen as a quotient of the stress gradient with respect to the mean stress through the specimen thickness. In this approach, equilibrium is satisfied after an initial "ringing" period in which the specimen experiences a rapid build-up to stress. It was calculated that the mean homogenization ratio ranged between 3% and 10% for the nanofiller-modified epoxy materials utilized in this investigation. This degree of homogenization was determined to be sufficiently low to simplify Equations (3.3)–(3.5) with $\epsilon_T(t) = \epsilon_I(t) + \epsilon_R(t)$ for the investigation window of 100–250 μs [98] [114].

After satisfying dynamic stress equilibrium, the average stress within a short cylindrical specimen can be calculated with Equation (3.5). Figure 4.6 shows the mean stress-strain relationship for all nanofiller-modified epoxy specimens. Unmodified epoxy specimens were prepared as a baseline comparison. Note the specimens did not experience catastrophic failure during experimentation. This is indicated by a steady and fairly linear stress-strain relationship. The dynamic stiffness (i.e., rate-dependent stiffness), E_d, was determined through a linear regression curve fit in the linear-elastic region of the loading phase. The results in
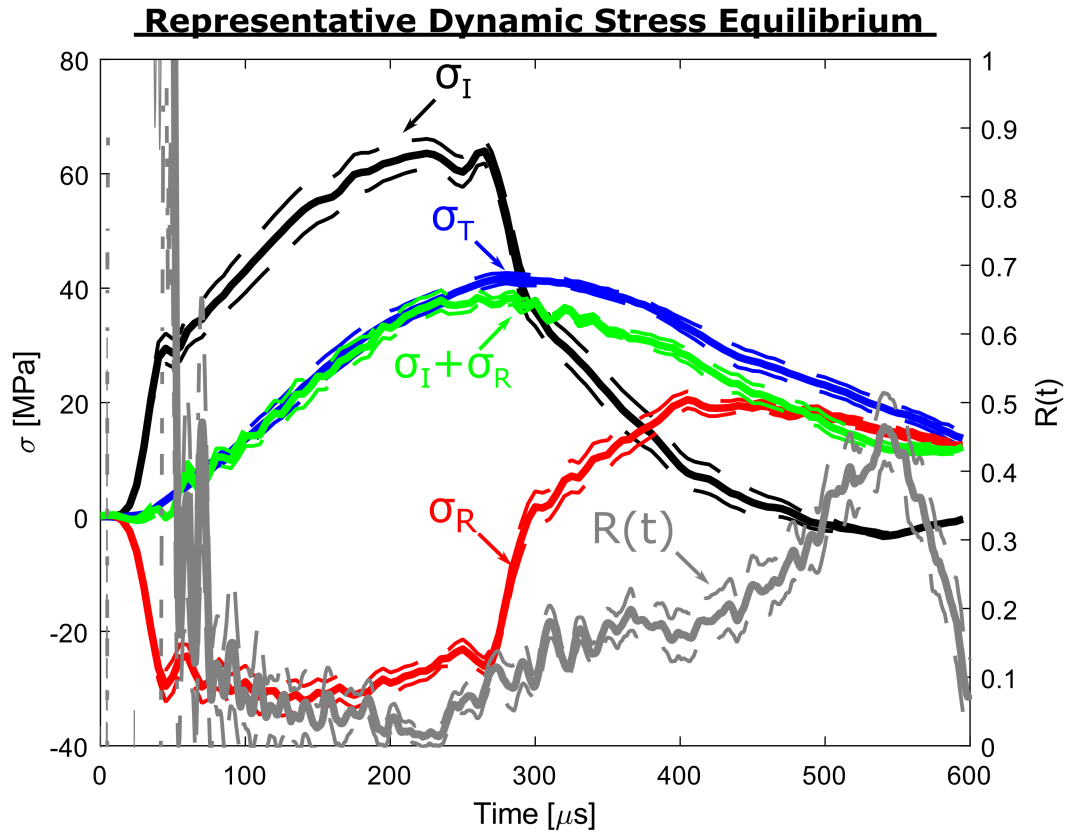
Figure 4.5. Conventional SHPB testing necessitates stress equilibrium at either specimen end (green and blue curves). Stress equilibrium can also be examined through a homogenization ratio, R(t). Shown here is representative stress equilibrium development in MWCNT-modified epoxy. The solid and dashed lines are the mean and standard deviation, respectively. The left y-axis references stresses and the right y-axis references the homogenization ratio. Dynamic equilibrium occurs after the initial ramping period and before unloading (i.e., in the window of 100–250 μs).

Dynamic Elastic Modulus of Nanocomposite Samples
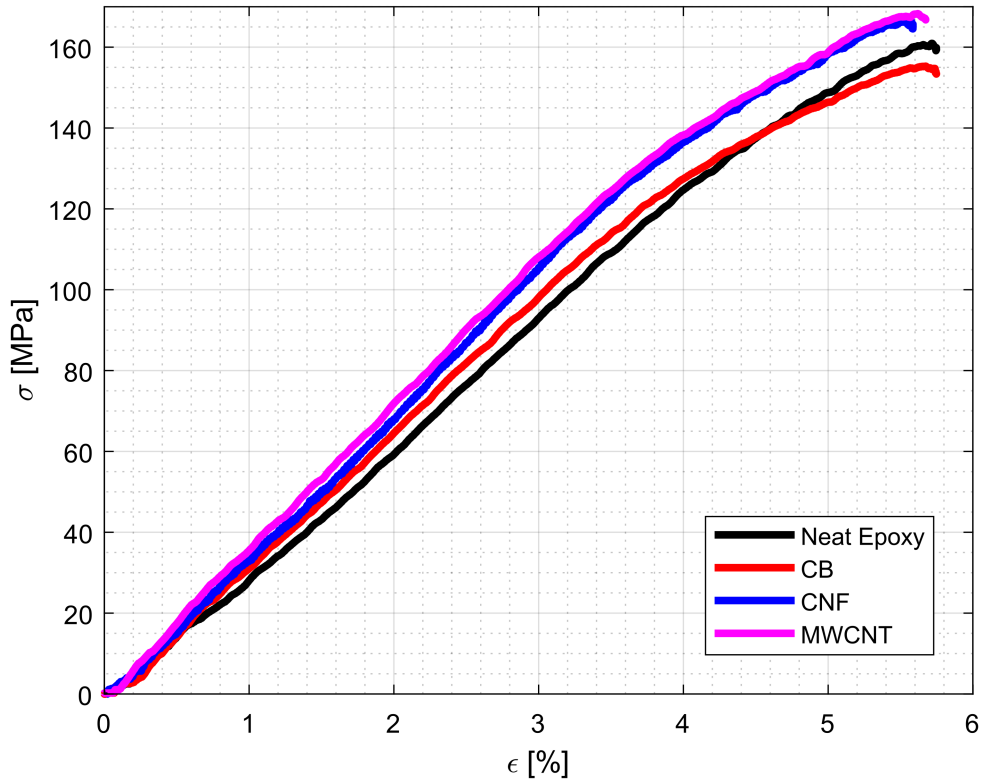
Figure 4.6. The mechanical response of neat and nanofiller-modified epoxy material can be examined through dynamic stress vs. strain curves. The dynamic stiffness is the slope of this curve in the linear region. Figure adapted from [117].

Table 4.3 show modest improvements to the nanofiller inclusions. These results are in agreement with works published in the literature investigating low quantities of carbon nanofiller inclusions that provide slight benefits to mechanical properties at high strain rates [115] [116].

4.2 Steady-State Vibration

It was demonstrated the piezoresistive effect is well-suited to capture high-strain rate impacts and establish an upper bound in terms of loading rate for this thesis. The following investigation focused on intermediate loading rates within the range of structural vibrations. Notably, steady-state vibration is a common dynamic loading condition faced by structural

Material	[GPa]	$\dot{\epsilon}\,[s^{-1}]$
Neat Epoxy	3.24 ±0.53	235 ±32
CB/Epoxy	3.37 ±0.35	234 ±31
CNF/Epoxy	3.56 ±0.23	230 ±17
MWCNT/Epoxy	3.59 ±0.21	233 ±18

Table 4.3. Dynamic Stiffness of carbon nanofiller-modified epoxy material at high strain rates.

elements. In order to study the potential for the piezoresistive effect to detect and extract useful information from vibrating structures, the CNF-modified epoxy rod structure used in the high-rate impact loading investigation was repurposed in a new experiment. The CNF/epoxy rod was utilized in this investigation for its superior strain-sensing capabilities in both tension and compression. Additionally, the low baseline resistance measurement between the electrodes, 937 Ω, allowed for the specimen to be easily incorporated within a modified Wheatstone bridge circuit, presented in Figure 3.6. The remaining three components of the bridge circuit utilized fixed-value resistors and a manually adjustable potentiometer resistor for circuit balancing. On account of being connected to the Wheatstone bridge circuit, piezoresistive-induced changes in the circuit resistance will result in measurable voltage changes that are then amplified by an AD8221 operational amplifier. The op-amp was configured to produce a gain of approximately 1000 to magnify expected small voltage variations due to the low force output of the shaker system.

In this experiment, the shaker system excited the CNF/epoxy rod specimen at frequencies spanning on the order of 10^2 to 10^4. This frequency range falls within the operational capabilities of the shaker system and does not represent a specific structural or diagnostic application. The representative piezoresistive response at the electrodes from the CNF/epoxy rod specimens for a low, moderate, and high frequency are shown in Figures 4.7–4.9. The figures are divided into three subplots. The top subplot presents the amplified Wheatstone bridge response in the form of voltage changes before and after applying a band-pass filter. Examining the raw data reveals there is significant noise collected through the Wheatstone bridge from the rod. This behavior is most prominent at the lowest frequency, where the largest window of data collection occurs. The cause is suspected to be electromagnetic
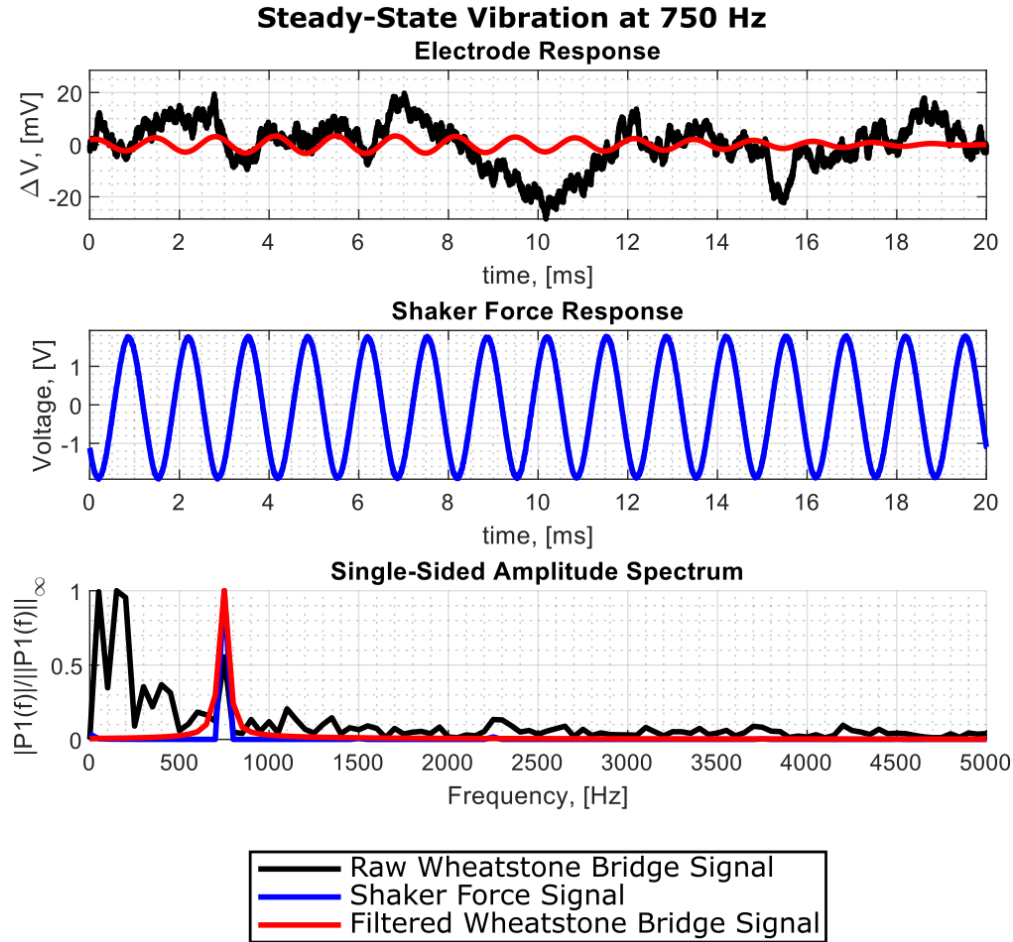
Figure 4.7. (Top) The change in Wheatstone bridge voltage response demonstrates the piezoresistive behavior of the 1.5 wt.% CNF/epoxy rod was recorded during testing, shown in black, and a bandpass filter was applied to the raw voltage data, shown in red. (Middle) The shaker force response illustrates the mechanical loading onto the mounted rod at a low excitation frequency (blue). (Bottom) An FFT was applied to the collected signals to reveal important characteristics in the frequency domain.

interference (EMI), where the conductive CNF/epoxy rod behaves as an antenna and introduces environmental noise into the collected piezoresistive measurements. On account of this, a digital band-pass filter was applied to the raw data using MATLAB's signal processing toolbox. This was achieved by first conducting a fast Fourier transform of the raw signal. Second, discarding the low-frequency contributions as it was speculated to be due to environmental factors such as EMI. Third, the frequency belonging to the most prominent
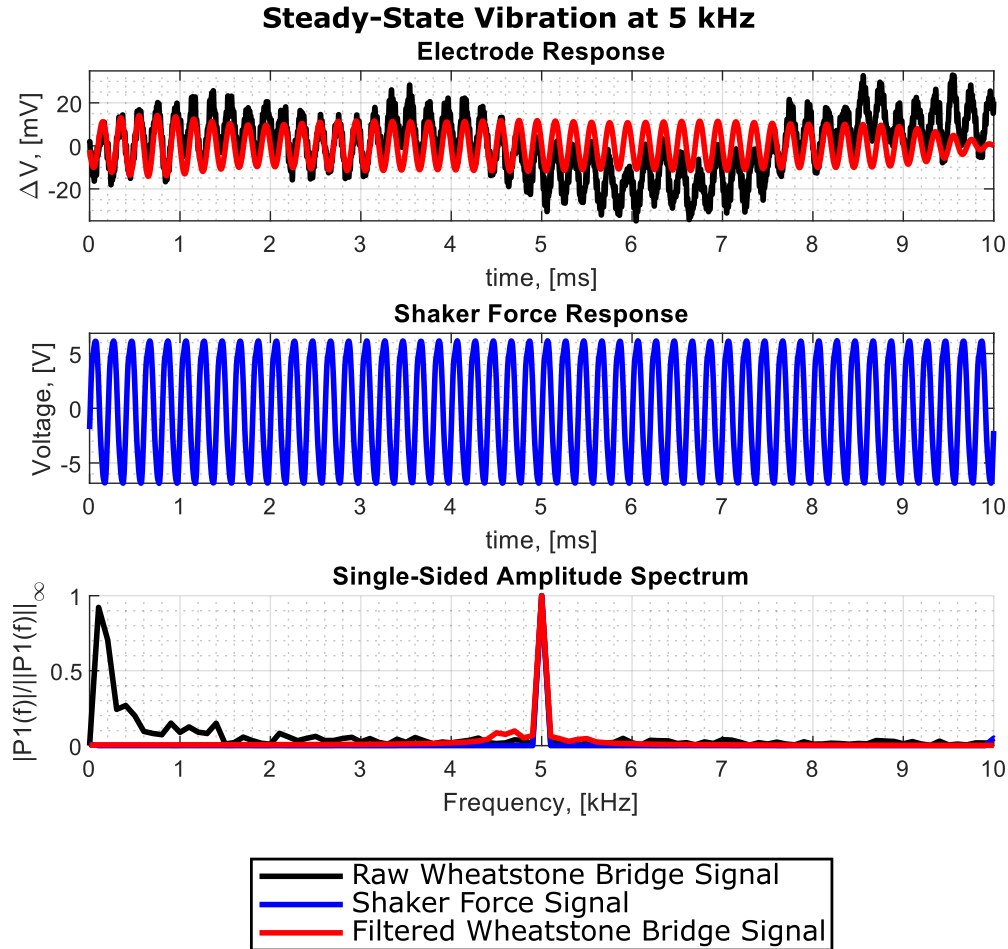
Figure 4.8. (Top) The change in Wheatstone bridge voltage response demonstrates the piezoresistive behavior of the 1.5 wt.% CNF/epoxy rod was recorded during testing, shown in black, and a bandpass filter was applied to the raw voltage data, shown in red. (Middle) The shaker force response illustrates the mechanical loading onto the mounted rod at a moderate excitation frequency (blue). (Bottom) An FFT was applied to the collected signals to reveal important characteristics in the frequency domain.

peak was identified. Finally, a digital filer was created with a pass-band centered around ± 10% of the determined frequency. Implementing this approach to signal processing resulted in noticeable improvements and clearly showed the excitation signal embedded in the raw data, presented as the red curve in the first subplot. Qualitative comparison to the shaker system output force sensor corroborates the piezoresistive measurements, as shown in the second subplots of Figures 4.7–4.9.

Several observations can be made when examining the collected and filtered signals in the frequency domain. First, the raw Wheatstone bridge signal presents significant low-frequency contributions around 60 Hz, a common frequency for environmental EMI. However, the raw signal still presents a clear and distinguished frequency response that is in agreement with the frequency response of the shaker force sensor. This is an encouraging sign, as even a noisy piezoresistive response signal carries essential information under steady-state loading conditions. This leads to the second observation, where employing simple or modest signal processing techniques can lead to significant improvements in the filtered signal in both the time and frequency domains. However, these benefits are not as apparent for high-frequency testing because a smaller data collection window artificially suppresses the effects of low-frequency noise in favor of more accurately capturing high-frequency behavior. At higher frequencies, the effect of low-frequency noise is minimal or absent, and this allows for piezoresistive behavior to be observed more directly from the raw data. This is supported by distinct responses or poles in the frequency domain. This serves as a confirmation that the piezoresistive effect can be effectively utilized for tracking elastic strain waves in nanofiller-modified materials.

4.3   Wave Packet Excitation

Drawing from the insights gained in the prior contributions outlined in this thesis, the following contribution sought to directly determine material-state dynamics from piezoresistive measurements of highly controlled wave packets. In order to pursue this investigation, slender long rods with a diameter of 12.6 mm and 685.8 mm in length ($\approx$ 54.5 aspect ratio) were cast and prepared with evenly spaced surface-mounted electrodes along the rod length. Rods were manufactured with nanofiller concentrations of 0.5 wt.%–1.5 wt.% CNFs. Furthermore, the shaker system experimental setup was modified into a closed-loop configuration and employed an isolated electrical circuit to provide power for a high-precision current supply. The benefits of these adjustments are two-fold: first, a closed-loop system allows for highly-repeatable measurements to be taken from the CNF/epoxy rod. This was a necessary adjustment to capture highly transient and low-strain amplitude wave packet transmission
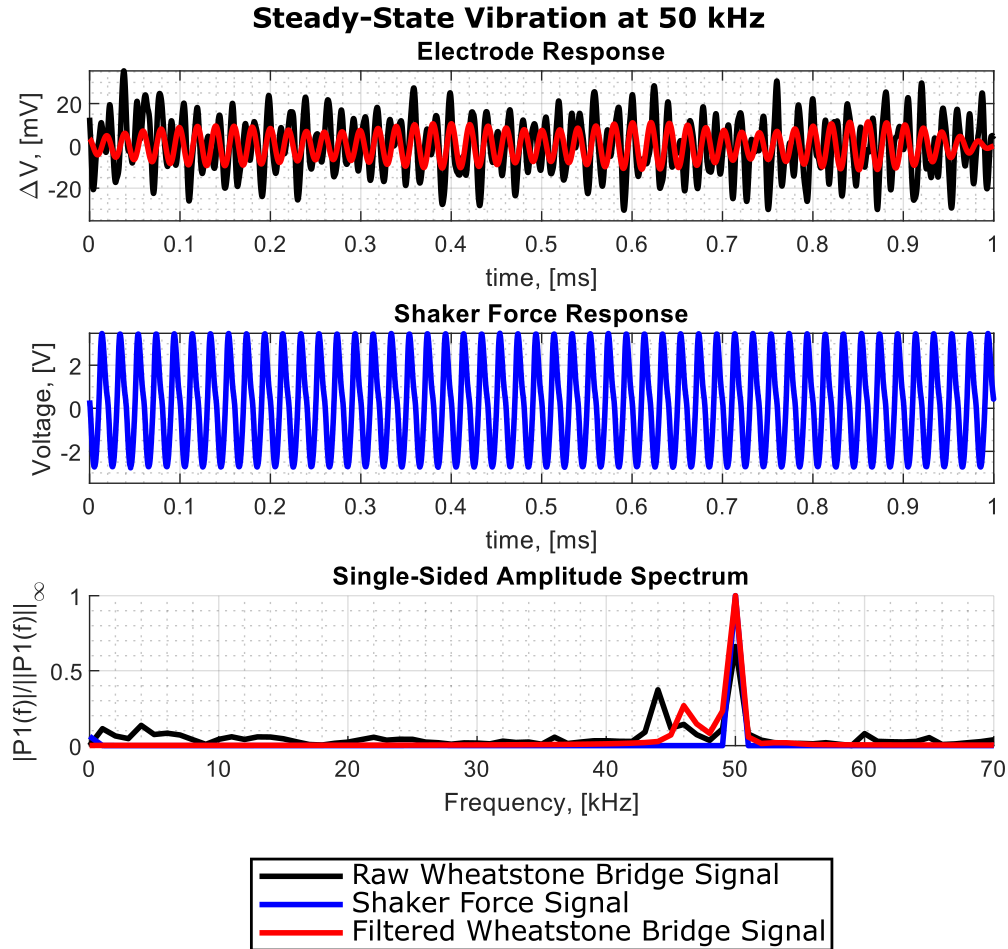
Figure 4.9. (Top) The change in Wheatstone bridge voltage response demonstrates the piezoresistive behavior of the 1.5 wt.% CNF/epoxy rod was recorded during testing, shown in black, and a bandpass filter was applied to the raw voltage data, shown in red. (Middle) The shaker force response illustrates the mechanical loading onto the mounted rod at a high excitation frequency (blue). (Bottom) An FFT was applied to the collected signals to reveal important characteristics in the frequency domain.

into the CNF/epoxy rods due to the fact that preliminary testing observed significant noise from the piezoresistive measurements. This also enabled basic signal processing techniques, such as ensemble averaging on the data collected, to significantly improve the signal-to-noise ratio of piezoresistive measurements for further analysis. And second, the isolated electrical circuit mitigated potential common mode voltage noise seen in preliminary measurements taken from the rod that was due to the power draw of the shaker voltage amplifier. The

impacts of this noise are apparent for very sensitive measurements, as was the case for this investigation involving low amplitude wave packet transmission into a piezoresistive rod.

4.3.1 Spatially-Distributed Sensing

Remote wave packet excitation was conducted on CNF rods with nanofiller concentrations of 0.5 wt.%, 1.0 wt.%, and 1.5 wt.% during the initial stages of testing. It was found that the CNF/epoxy rod with the smallest quantity of CNF nanofillers could not reliably track the propagation of the wave packet stress wave. Measurements produced an identical response across all electrode pairs and injection patterns, indicating that the rod behaved as an antenna and was susceptible to picking up EMI produced by the electromagnetic/piezo-electric shaker. As a result, an additional 1.25 wt.% epoxy rod was manufactured. The decision to avoid using a higher concentration of CNFs was driven by the significant increase in the viscosity of nanofiller-modified epoxy mixtures. This increased mixture viscosity posed substantial challenges in the cast manufacturing process of rod specimens. The baseline resistances of the 1.0 wt.%, 1.25 wt.%, and 1.5 wt.% CNF/epoxy rods with different injection schemes are visually presented in Figure 4.10. Tables 4.4-4.6 provide concise statistical data summarizing the baseline resistances for each injection scheme. Baseline electrical measurements show significant variability of electrical properties for all rods. This variability is most prominent in the adjacent injection scheme, as most measurements from the rod are taken along the rod with the smallest distance between electrode pairs. This variability in electrical properties primarily results from inconsistent nanofiller dispersion. However, air bubbles or voids introduced during casting may also produce a similar spatially-varying distribution. As the spacing between measurement electrode pairs increases (i.e., larger n), the baseline resistance also increases as a larger volume of material contributes to the measurement and more accurately represents the bulk electrical properties of the material through the rods. To overcome the nonuniform nanofiller distribution issue, the piezoresistive behavior of the CNF/epoxy rods will be assessed through relative changes in resistance, as evaluated in equation 4.1.

	Injection Scheme					
	Adjacent	n=1	n=2	n=4	n=8	n=16
Mean [kΩ]	5.6545	8.3054	10.8573	15.6447	25.2740	40.7641
Medium [kΩ]	4.2690	6.9106	9.5752	15.1466	24.6301	39.4317
Standard Deviation [kΩ]	4.5752	4.2766	4.1619	4.4091	5.2747	5.4172
Range [kΩ]	25.6047	24.8720	25.6721	27.9172	31.0169	30.9284

Table 4.4. Statistical data for the measured baseline resistance between electrode pairs along the length of the 1.0 wt.% CNF/Epoxy rod via a two-point probe method of direct current injection and voltage measurement.

	Injection Scheme					
	Adjacent	n=1	n=2	n=4	n=8	n=16
Mean [kΩ]	5.0671	7.1887	9.8628	14.6117	23.5837	41.9799
Medium [kΩ]	2.9618	4.8213	7.7834	12.1430	21.4621	40.4199
Standard Deviation [kΩ]	6.7752	6.6696	7.7333	8.8787	9.0550	9.6432
Range [kΩ]	42.9580	37.9003	45.6357	53.2149	54.1091	52.6795

Table 4.5. Statistical data for the measured baseline resistance between electrode pairs along the length of the 1.25 wt.% CNF/Epoxy rod via a two-point probe method of direct current injection and voltage measurement.

	Injection Scheme					
	Adjacent	n=1	n=2	n=4	n=8	n=16
Mean [kΩ]	1.7577	2.8492	3.9901	6.2088	10.5872	19.1022
Medium [kΩ]	1.5545	2.6468	3.8782	6.0416	10.5216	19.1581
Standard Deviation [kΩ]	0.5669	0.6685	0.7500	0.9008	1.0145	0.7432
Range [kΩ]	2.3561	2.6520	3.4569	3.8233	3.5118	2.4047

Table 4.6. Statistical data for the measured baseline resistance between electrode pairs along the length of the 1.5 wt.% CNF/Epoxy rod via a two-point probe method of direct current injection and voltage measurement.

(a)

(b)

(c)

Figure 4.10. The electrical resistance measurements were obtained from three different CNF/epoxy rods: (a) 1.0 wt.%, (b) 1.25 wt%, and (c) 1.5 wt.%. The electrical resistance measurements represent the baseline or reference state for the set of injection schemes or electrode spacing explored. Due to wave packet excitation, piezoresistive measurements will be presented as relative changes in resistance, normalized to the baseline resistance.

Wave packets, in the form of a 5.5-cycle Hanning function, were transmitted into the CNF/epoxy rod specimens while simultaneously interrogating piezoresistive measurements from the surface-mounted electrodes along the length of the rods. This investigation employed wave packets with carrier/modulation frequencies ranging from 2.5 kHz/27.5 kHz to 5.0 kHz/55 kHz, with carrier frequency increments of 100 Hz. To account for the different units and substantially different magnitudes in the responses from the force sensor, laser vibrometry (LV) measurement, and piezoresistive responses, these signals were appropriately scaled to allow for a clearer interpretation of a one-dimensional wave packet. It is important to note that aside from ensemble averaging of 1024 independent and separate measurements, the only additional signal filtering employed was a 15-point moving mean average on the collected data to diminish very high-frequency noise. The piezoresistive responses from the CNF/epoxy rods for the 2.5/27.5 kHz wave packet for the different injection schemes considered are shown as space-time plots in Figures 4.11–4.13. It should also be noted that the extrinsic measurements (e.g., force sensor and laser vibrometer) were collected at both ends of the rod to provide a clearer understanding of the transmission and propagation of the wave through the rod.

The space-time plots presented in Figures 4.11–4.13 provide multiple interesting observations for discussion. First, the CNF/epoxy rods can effectively track dynamic behavior, as indicated by the piezoresistive measurements along the length of the rod, indicating different arrival times of the wave packets. This can be attributed to the embedded and distributed sensing capabilities enabled by the piezoresistive effect, where local changes in electrical properties can be monitored in real-time through surface-mounted electrodes. This suggests that it is possible to incorporate piezoresistivity as a multifunctional tool in certain vibration-based NDE applications where the subsurface nanofiller network is accessible.

Second, there is a noticeable reduction in the overall magnitude of the piezoresistive response as the wave packet propagates through the rod. This behavior may be attributed to the energy-dispersive properties inherent in viscoelastic materials, like epoxies, that attenuate the strain magnitude of highly-dynamic behavior, such as wave packets. On account that piezoresistivity is a deformation-driven phenomenon, the reduction of the overall strain magnitude would lead to a similar reduction movement of nanofillers within the matrix material

1.0 wt.% CNF/Epoxy Rod with Adjustable Electrode Spacing
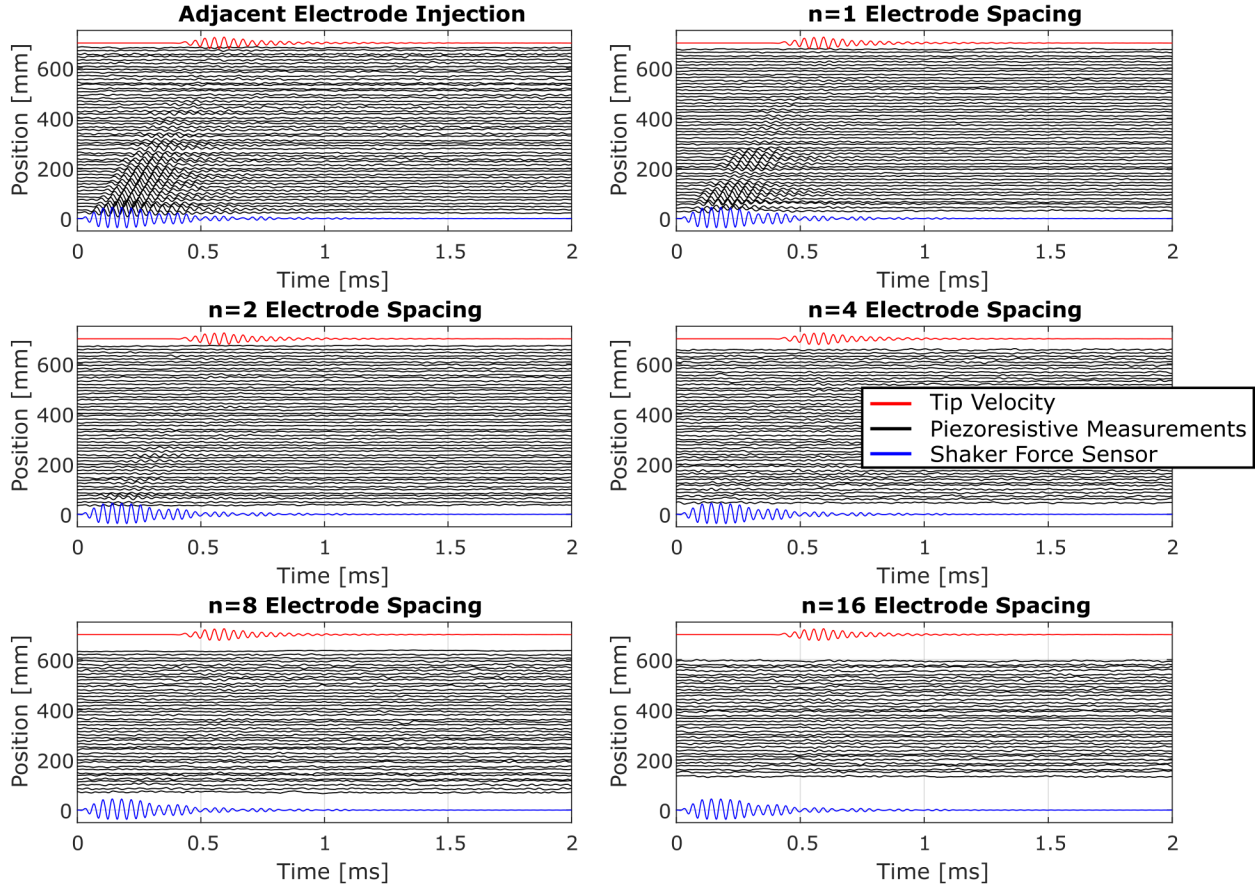
Figure 4.11. Space-time plots for a 5.5 cycle modulated-wave packet, with 2.5/27.5 kHz (f_c/f_m) excitation, were produced for the six different injection schemes considered. The force sensor, piezoresistive responses along the length of the 1.0 wt.% CNF/epoxy rod and particle velocity at the tip are shown as the blue, black, and red curves, respectively. The collected signals are scaled accordingly for qualitative comparison.

and ultimately lead to a smaller change in measurable electrical properties. Furthermore, closely examining the extrinsic responses of the experimental setup (e.g., the shaker force sensor and laser vibrometry measurements) supports this hypothesis. The data collection window was carefully chosen to observe the initial transmission and several reflections of the wave packet within the rod. However, it can be clearly seen that the wave packet was only recorded once with either set of extrinsic measurement devices. This is a notable observation because there appears to be a practical limitation to this combined conductivity/vibration

76

1.25 wt.% CNF/Epoxy Rod with Adjustable Electrode Spacing
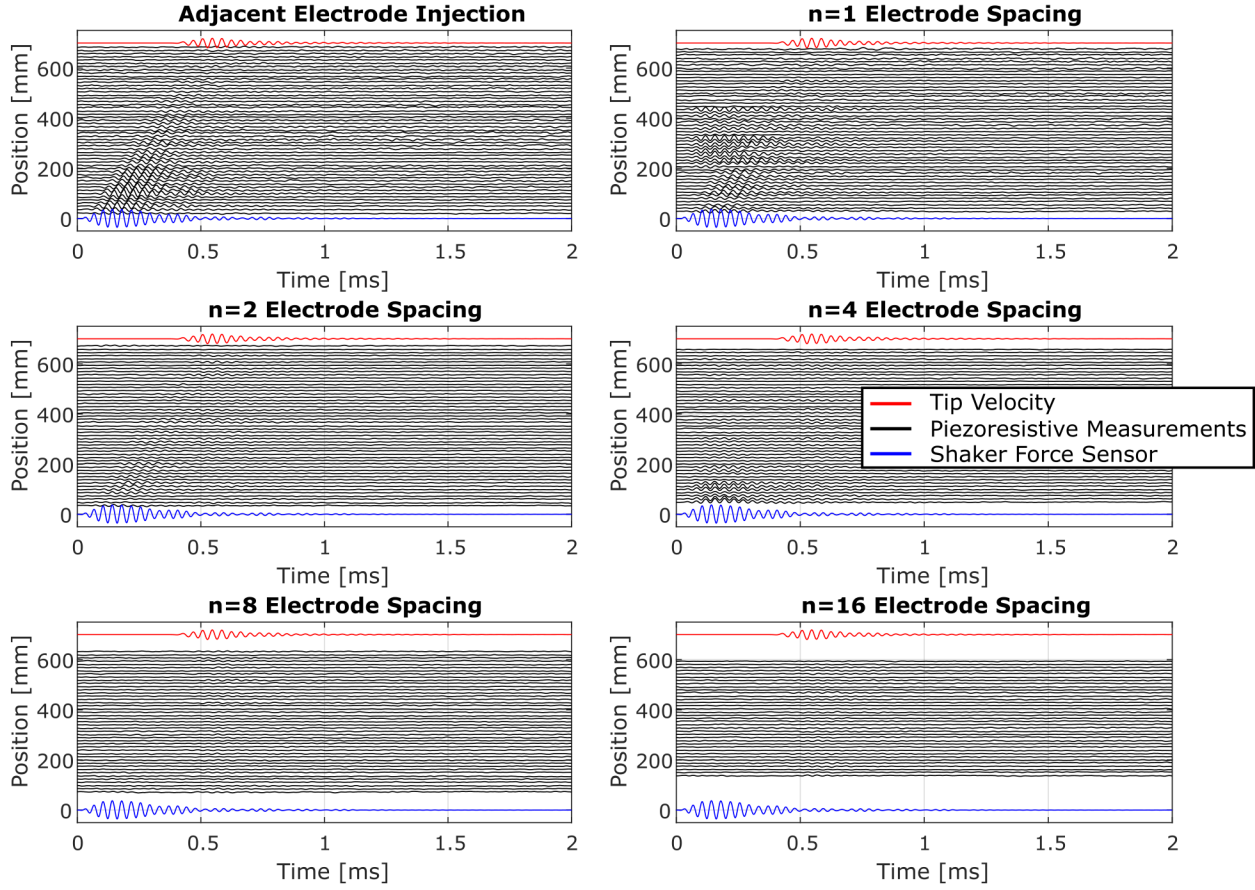
Figure 4.12. Space-time plots for a 5.5 cycle modulated-wave packet, with 2.5/27.5 kHz (f_c/f_m) excitation, were produced for the six different injection schemes considered. The force sensor, piezoresistive responses along the length of the 1.25 wt.% CNF/epoxy rod and particle velocity at the tip are shown as the blue, black, and red curves, respectively. The collected signals are scaled accordingly for qualitative comparison.

method approach to embedded sensing using remote excitation where the piezoresistive response is indistinguishable from background noise. However, continued refinement of this method may overcome this apparent limitation.

Third, from a qualitative standpoint, despite the CNF/epoxy being a viscoelastic material, the adjacent electrode injection scheme shows very little dispersion of the wave packet occurs. In other words, piezoresistive measurements clearly demonstrate the ability to monitor the wave packet propagating through the entire length of the structure when in com-

77
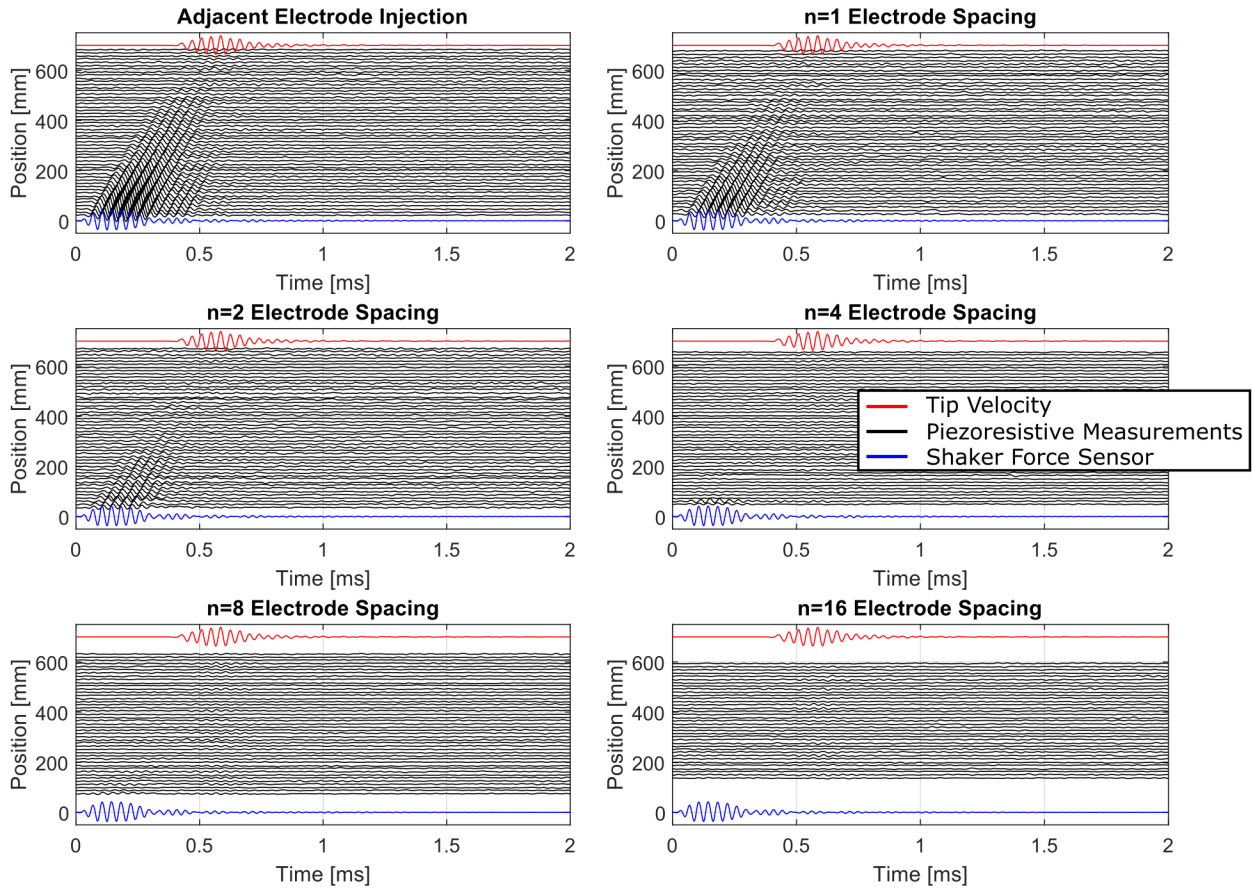
Figure 4.13. Space-time plots for a 5.5 cycle modulated-wave packet, with 2.5/27.5 kHz (f_c/f_m) excitation, were produced for the six different injection schemes considered. The force sensor, piezoresistive responses along the length of the 1.5 wt.% CNF/epoxy rod and particle velocity at the tip are shown as the blue, black, and red curves, respectively. The collected signals are scaled accordingly for qualitative comparison.

parison to the instance the wave packet was injected into the rods through the shaker force sensor and the arrival of the wave packet at the end through the laser vibrometer tip velocity measurements. Put differently, the propagation of the wave packet seems to travel at a linear velocity without significant deformation of the overall profile of the wave packet.

Fourth, the impact of nanofiller concentration seems to have a negligible or no correlation with the magnitude of the excitation response. To more clearly illustrate this observation, the piezoresistive response using the first electrode pair of the adjacent injection scheme is

examined in Figure 4.14 (left column). It is more apparent that the relationship between the magnitude of the shaker and piezoresistive response is not proportional. Here, the 1.5 wt.% and 1.0 wt.% CNF/epoxy rods exhibit a larger magnitude piezoresistive response for the same apparent input excitation than the 1.25 wt.% CNF/epoxy rod. This observation challenges conventional wisdom because it counters established wisdom that positive piezoresistivity demonstrates greater stimulus-response sensitivity when nanofiller concentration approaches the percolation threshold. However, this is predicated on the basis of the formation of a uniform and well-connected nanofiller network where the piezoresistive effect is primarily driven by interactions between adjacent (but physically separated) nanofillers through the effect of deformation on electron tunneling resistance changes. In reality, the uniform dispersion of nanofillers is unattainable. As a result, piezoresistive-driven changes to electrical properties are a combination of alterations in electron tunneling resistance and contact impedance of direct nanofiller-to-nanofiller junctions. To the best of the author's knowledge, directly isolating this behavior is experimentally impracticable without careful consideration.

Finally, adjustable electrode spacing successfully enabled artificial signal filtering from the CNF/epoxy rods. To elaborate on this point, it is worth noting that a larger volume of material contributes to the electrical measurement as the number of electrodes between the measurement electrodes, n, increases. As a consequence, the spacing between the measurement electrodes exceeds the wavelength of the modulation or encompasses an ever-larger portion of the entire wave packet. The small strain amplitude and alternating tensions/compression of the wave packet have an averaging effect, increasing the difficulty of discerning the exact piezoresistive effect from noise. Greater insights can be gleaned by examining the effect of electrode spacing-induced signal filtering by analyzing the first electrode measurement pair for each injection scheme through a fast-Fourier transform (FFT), as seen in Figure 4.14 (right column). Additionally, an FFT was conducted on the extrinsic measurements, such as the shaker force sensor and the laser vibrometer. Analysis of the collected signals in the frequency domain uncovers two additional discoveries. First, the piezoresistive and extrinsic measurements are in agreement in the frequency domain for the adjacent, n=1, and n=2 injection schemes. Second, the injection schemes with larger electrode spacing exhibit

significant low-frequency noise that is comparable to or greater than the signal transmitted at the known modulation frequency of 27.5 kHz. This definitively proves that dynamic signal filtering is achievable through a passive method, such as adjusting the electrode spacing.
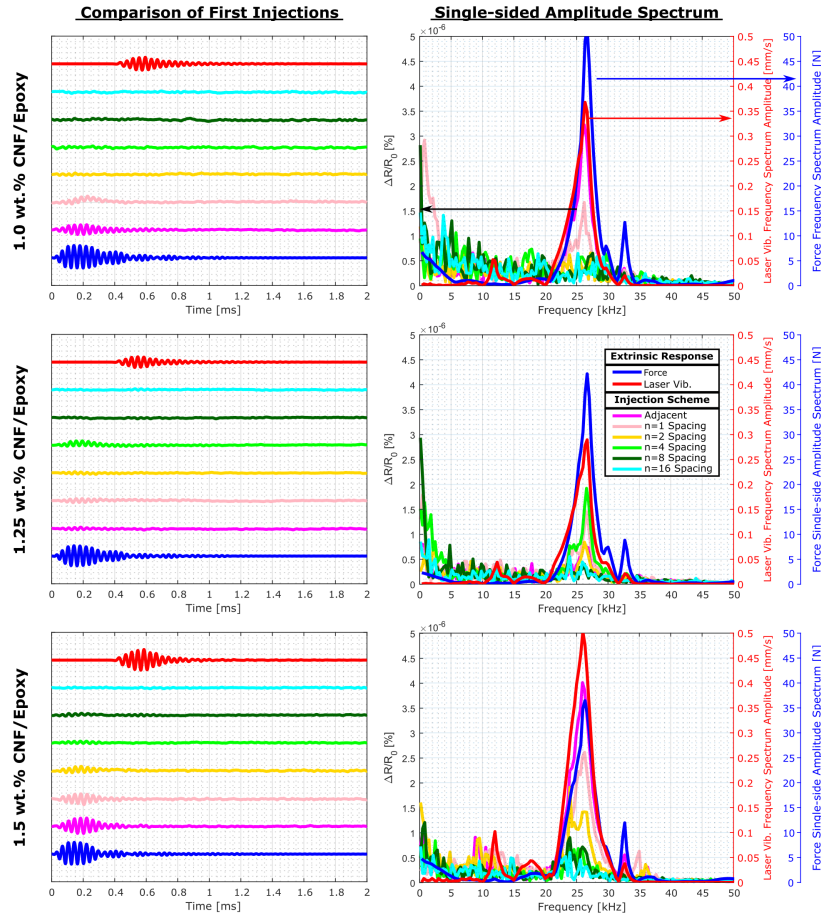
Figure 4.14. (Left column) The piezoresistive response of the first electrode measurement pair and injection schemes, along with the shaker force and laser vibrometer tip velocity, are compared for 2.5/27.5 kHz (f_c/f_m) wave packet excitation. The collected signals are scaled accordingly for qualitative comparison. (Right column) A fast-Fourier transform was applied to the collected signals for qualitative comparative analysis in the frequency domain. A triple y-axis plot shows the amplitude contributions for a range of frequencies for the piezoresistive measurements (black, left axis), force sensor (right, blue axis), and LV measurement (right, red axis).

4.3.2 Group Velocity Determination

By transmitting wave packets with a range of modulation frequencies, the dynamic characteristics of the CNF/epoxy rods can be assessed in relation to the group velocity. Conceptually, the approach to determining the group velocity of the wave packets bears a resemblance to the high strain-rate impact testing, where the arrival times for the triangular stress wave under the electrode measurement region were utilized to determine the elastic wave speed. Here, the response from the wave packet excitation will be utilized. Procedurally, the wave packet envelope's time of flight (ToF) is determined from the peak of a Hilbert transform of the collected signals. For the extrinsic measurements (i.e., force and LV signals), the group speed is calculated as the length of the rod divided by the ToF. However, a different approach is employed for the piezoresistive responses to mitigate the effect of noise on the analysis. For the piezoresistive measurements, only the first ten electrode measurement pairs for each injection scheme were used to calculate the group velocity as opposed to one. In this particular approach, the ToF for each measurement is determined from a Hilbert transform for the signal magnitude. Then, the obtained ToF is plotted against the location of the measurements along the rod. In other words, the arrival times for the peak magnitude of the wave packet are correlated with the position of the measurement on the rod. A linear regression curve (i.e., $y = mx + b$) is fitted against the relation between ToF and position. The group velocity, as determined from the piezoresistive measurements, was calculated from the slope of the fitted for all CNF/epoxy rods and injection schemes. The results of these calculations are shown in Figure 4.15.

The results bring to light several notable observations. The first observation pertains to the results determined using the extrinsic response of the shaker force sensor and the laser vibrometer at the tip of the rods. The calculated group velocities from the extrinsic response signals indicate a range of 1500–2200 m/s for the group velocity of the wave packets for the span of modulation frequencies explored. While this larger range is unexpectedly large, the previously determined elastic wave speed determined from SHPB falls within this range. The calculated group velocities from the piezoresistive response signals are unreliable in accurately estimating the group velocity when compared to extrinsic verification. Partic-

ularly, no discernible estimation can be made from the 1.0 wt.% and 1.25 wt.% CNF/epoxy rods. The sole exception of the 1.5 wt.% CNF/epoxy rod approaching the possibility of providing an adequate job in estimating the group velocity. Nevertheless, even in this set of experiments, no discernible estimations are possible for modulation frequencies beyond 40 kHz or for injection schemes with n = 4, n = 8, or n = 16 electrode spacing. One possible explanation may be due to the limitations of the shaker system, where higher frequency excitation may not yield strain amplitudes large enough to elicit a measurable piezoresistive response, and thus employing a Hilbert transform may not be the best technique to conduct this type of analysis with these conditions.

4.3.3 Strain State Determination

Several tools computational tools were employed to achieve the goal of recovering the strain state from recorded electrical measurements: 1) An analytical closed-form piezoresistivity model [65] was chosen to inversely determine the strain state of the 1.5 wt.% CNF/epoxy rod. This model was chosen due to the fact that change in electrical resistivity has been shown to be predicted accurately for the CNF/epoxy material systems. Furthermore, due to the simple experimental strain state (e.g., axial deformation only), it is possible to establish an inverse relationship between the strain state and piezoresistive behavior. 2) To assist in the piezo-inversion process, the CEM was integrated with the analytical piezoresistivity model to determine a geometric correction factor. The geometric correction factor is to account for the difference in resistance measurements between prismatic and surface-mounted electrodes. Employing a geometric correction factor is motivated by the need to relate normalized resistance measurements taken by surface-mounted electrodes to changes in resistivity in the measurement region, as would be determined if end electrodes were employed for prismatic measurements of the same cylinder volume. 3) In parallel, a "digital twin" of the CNF/epoxy rod was created on ABAQUS commercial finite element analysis (FEA) software to conduct an explicit elastodynamic simulation. This dynamic simulation will serve as a method to obtain the full-field strain state of the nanocomposite rod with repli-
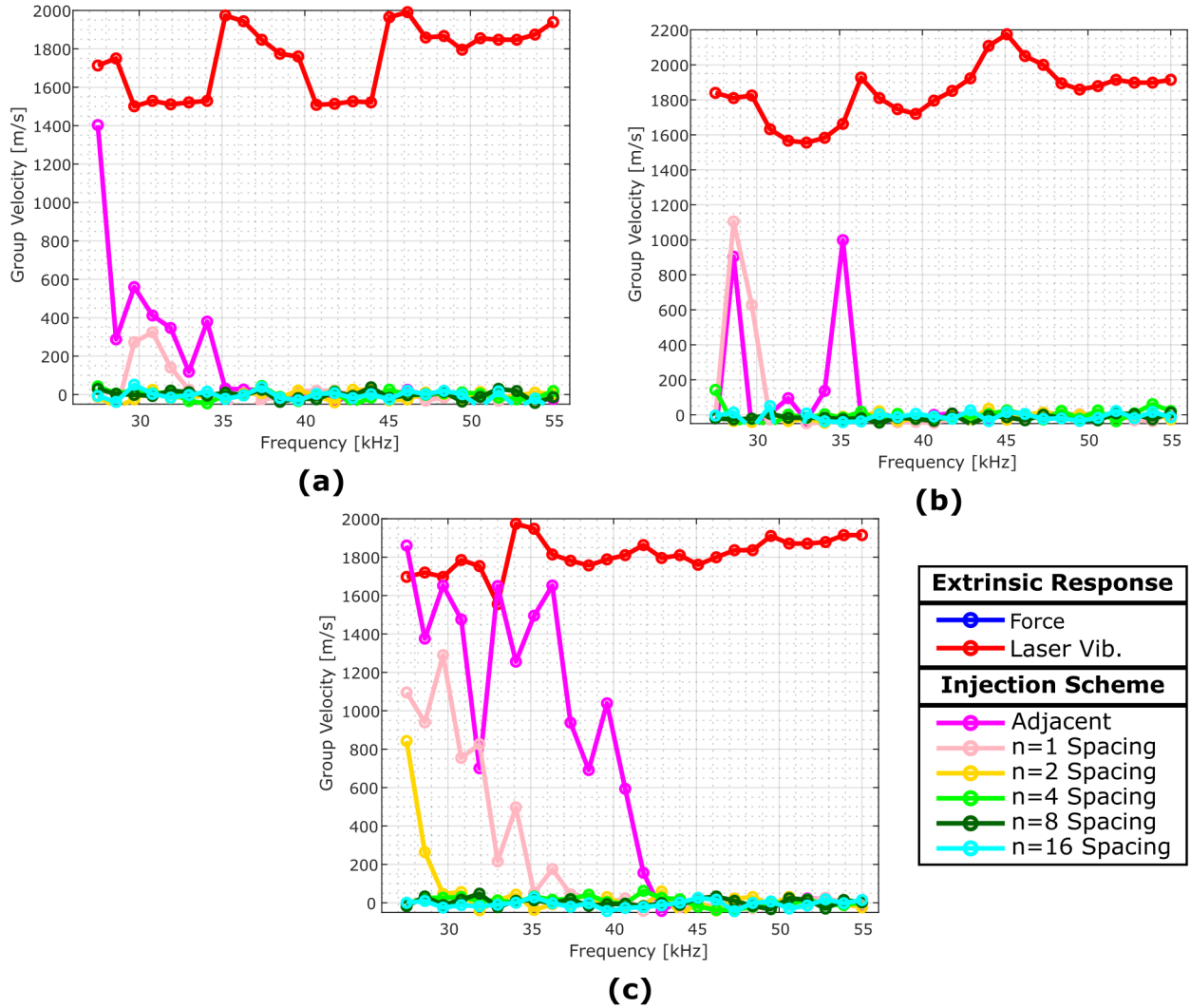
Figure 4.15. The group velocity estimations from three different CNF/epoxy rods: (a) 1.0 wt.%, (b) 1.25 wt% and (c) 1.5 wt.%. The group velocity of the wave packet is calculated from piezoresistive and extrinsic measurements. It can be seen that there is significant variability, and in most cases, piezoresistive measurements are unable to provide a discernible estimate or trend.

cated loading and boundary conditions. The resulting strain field from the FEA simulation is then compared to the obtained strains from the piezo-inversion process.

Analytical Piezoresistivity Model

The analytical piezoresistivity model, equation (3.7), employed the following material properties for the matrix and fiber: $\rho_m = 1134$ k/g^3, $\nu_m = 0.351$, $\sigma_f = 10^5$ S/m, $l_f = 50$ μm,
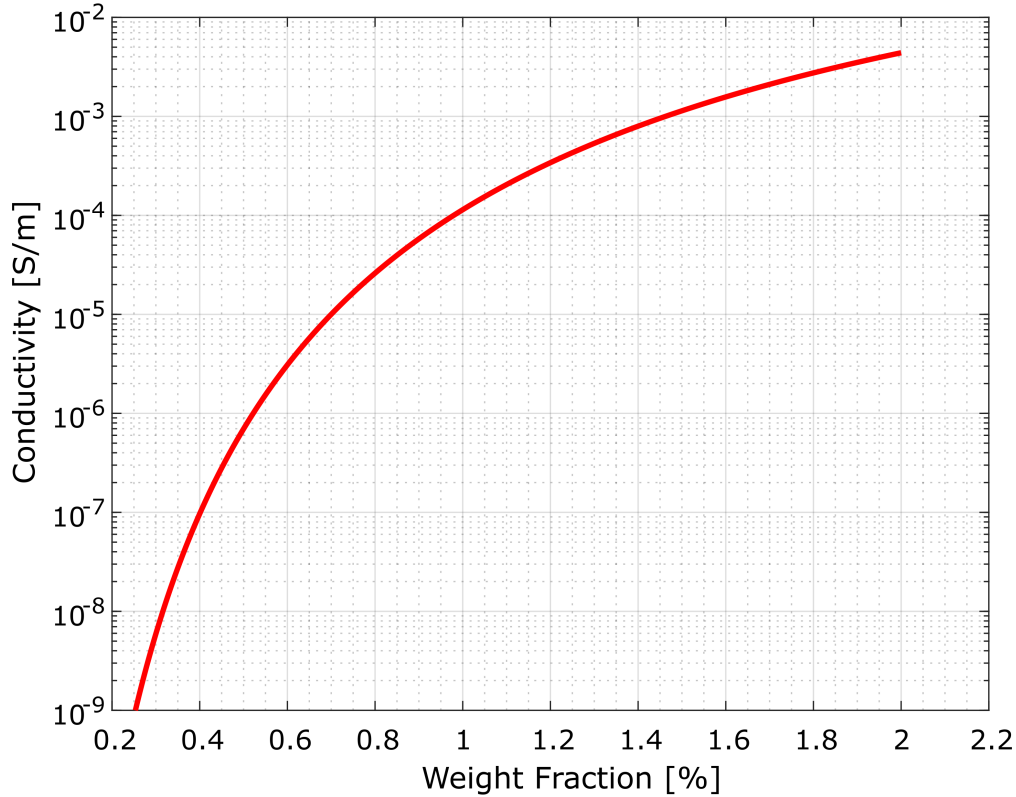
Figure 4.16. Analytical conductivity predictions of CNF-modified epoxy nanocomposites can be made with experimentally collected conductivity data. Hassan and Tallman et al. calibrated the analytical piezoresistivity model for CNF/epoxy material system.

$d_f = 100$ nm, and $\lambda = 1$. Prior work by Hassan and Tallman [118] determined the calibrated fitting values to be $\alpha = 1.58$ and $\beta = -0.28$ for CNF/epoxy material systems, allowing for the conductivity of a nanocomposite to be estimated as a function of weight fraction, as shown in Figure 4.16. The calibrated piezoresistivity model can then be employed to predict the effects of applied axial strain on the resistivity changes of a representative body element, as illustrated in the schematic subplot of Figure 4.17.

The piezoresistive behavior of the representative body element for an infinitesimal strain range of ± 50 $\mu\epsilon$ using the calibrated analytical model is presented in Figure 4.17. A linear curve fit (i.e., $y = mx + b$) was applied on the determined normalized resistivity change curve as a function of axial strain. The linear regression analysis was deemed to be an appropriately chosen model due to its exceptionally high coefficient of determination value,

$R^2 = 0.99999$. A high value for the coefficient of determination denotes a strong agreement between the model data and the fitted curve. This allows us to approach piezo-inversion, or the ability to inversely determine the strain state from normalized resistivity measurements, using the simple linear relationship as opposed to attempting to invert the nonlinear analytical piezoresistivity expression in equation (3.7) to obtain the strain state. Examples of more challenging approaches to solve the conductivity-to-mechanics inverse problem are contained in references [61] [88] [118] [119]. Given that both the representative body element and the CNF/rod are subjected to a simple strain state, specifically a principal strain state, it is justified to employ this approach. This relatively simple approach to piezo-inversion is infeasible for relatively large strains and combinatorial loading states (i.e., a non-diagonal strain tensor). Therefore, as opposed to inversely obtaining the exact strain state from the analytical piezoresistivity model, the strain state is instead determined from the fitted curve instead.
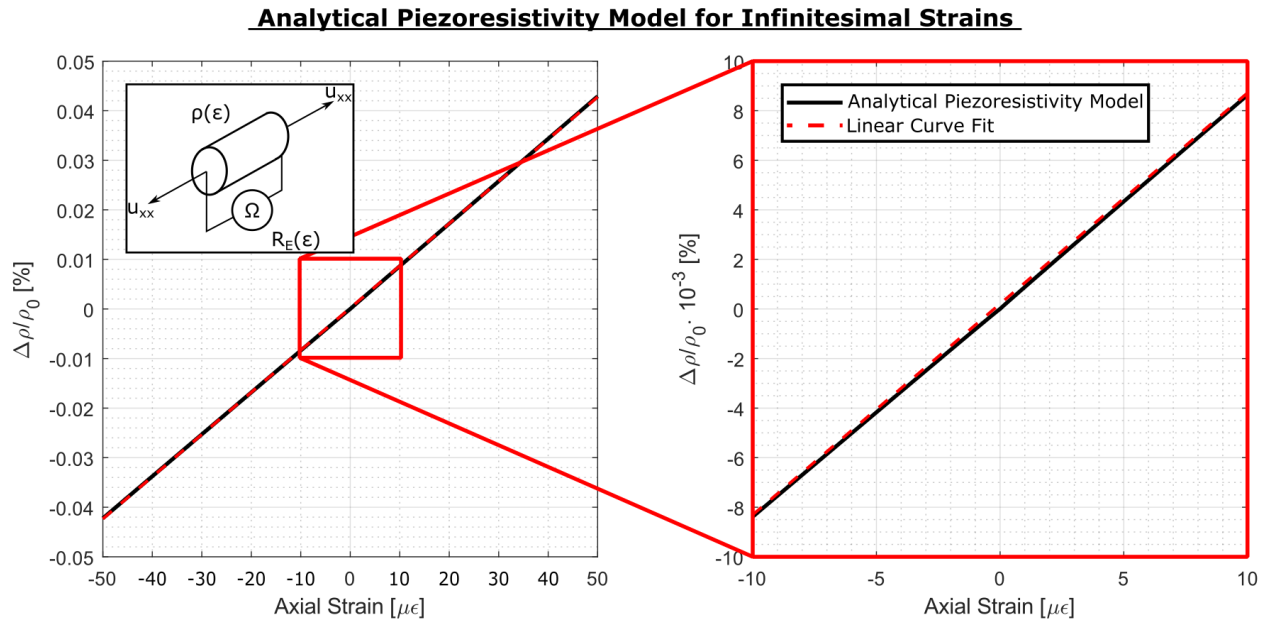
Figure 4.17. (Top-left schematic subplot) The calibrated analytical piezoresistivity model was leveraged to estimate the change in electrical properties for a CNF/epoxy nanocomposite experiencing a simple and infinitesimal strain state. A linear regression analysis (dashed red line) was performed on the piezoresistive response (black solid line) of the representative body element in response to axial strain. The curve fit was determined to be: $\Delta\rho/\rho_0 = (8.4593 \cdot 10^{-4}) \cdot \mu\epsilon + 3.0370 \cdot 10^{-4}[\%]$.

Geometric Correction Factor

The electrical resistance measured between "end-covering" vs. "surface-mounted" electrodes would differ significantly if taken from the same representative volume. The benefit of taking electrical measurements through the entire prismatic volume is that the intrinsic electrical properties can be directly calculated with geometric considerations of the body (i.e., cross–sectional area and cylinder height). However, measurements taken from the surface, while easier, do not permit a similar determination of intrinsic electrical properties. An implicit geometric correction factor was introduced in this work to allow the electrical measurements from "surface-mounted" electrodes to relate to changes in intrinsic electrical properties. By applying the appropriate geometric correction factor, the experimentally collected normalized resistance measurements can be accurately converted to equivalent normalized resistivity measurements and thereby enable the piezo-inversion process outlined in the previous section.

The first step to obtaining the geometric correction factor is to model a cylindrical volume that is a physically accurate representative body of the CNF/epoxy rod between a pair of surface-mounted electrodes, as seen in the simple schematics of Figure 4.18 (top right). The cross-sectional dimensions and width of the surface-mounted electrodes, w_E, were held constant as the spacing between the electrodes, L_s, was adjusted to obtain a relation for the geometric correction factor. The CEM and analytical piezoresistivity model are integrated for FEA of the cylinder. The CEM was constructed to obtain the resistance measurements from "end-covering" and "surface-mounted" electrodes on the same cylinder model using a baseline resistivity prediction for 1.5 wt.% CNF/epoxy provided by the analytical piezoresistivity model. The end-covered electrodes represent a prismatic measurement through the entire volume of the cylinder, and the electrical resistance calculated from the CEM will be equivalent to the theoretical resistance of the cylinder. The cylinder's theoretical resistance was then compared to the resistance measurements from the surface-mounted electrodes found by the CEM. In regard to piezoresistive behavior, it is desired to enforce an equivalency between the relative changes in measured resistance between surface and end-covering
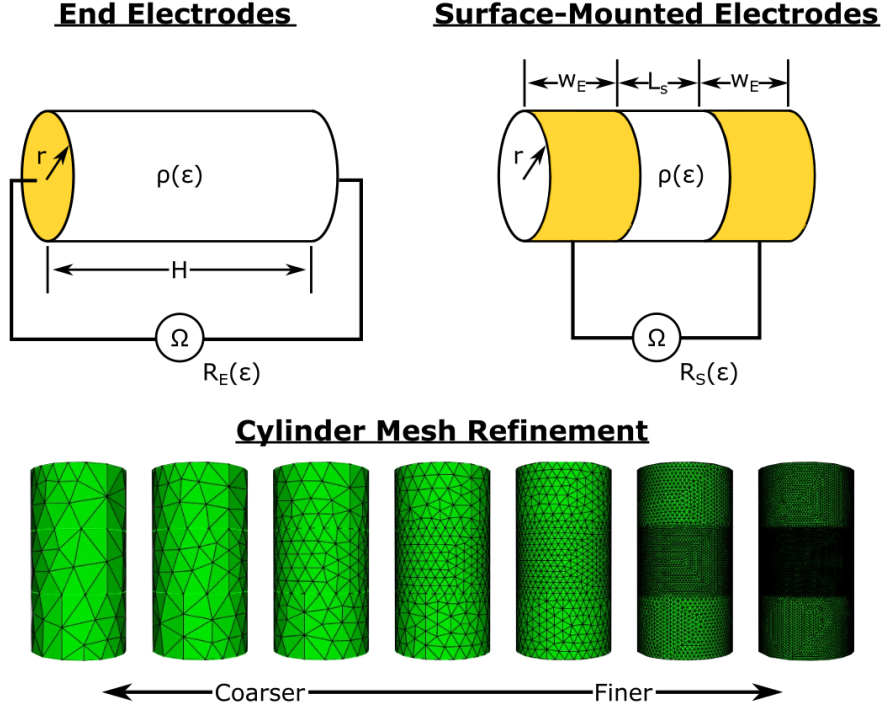
Figure 4.18. The CEM was applied to a representative cylinder body with end electrodes (top left) and surface-mounted electrodes (top right). Electrodes are shaded yellow for clarity. (Bottom) A representative cylinder with a range of mesh refinement is presented.

electrodes. The calibration factor will represent the equivalence between piezoresistive measurements taken by end-covering and surface-covering electrodes,

$$\frac{\Delta R_S}{R_{S,0}} \approx k_c \frac{\Delta R_E}{R_{E,0}} = \frac{\Delta \rho}{\rho_0} \tag{4.3}$$

Here, the geometric correction factor, k_c, is defined as the ratio of the baseline resistances of the surface and end-covering electrodes, $k_c = R_{S,0}/R_{E,0}$ and is treated similarly as the gauge factor for strain gages relating relative changes in electrical resistance to mechanical strain. The geometric correction factor enables the change in resistivity of the cylinder to be estimated and is then combined with the analytical piezoresistivity model to obtain the strain within the measurement region.

$$\frac{\Delta \rho}{\rho_0} \approx \frac{1}{k_c} \frac{\Delta R_S}{R_{S,0}} \tag{4.4}$$
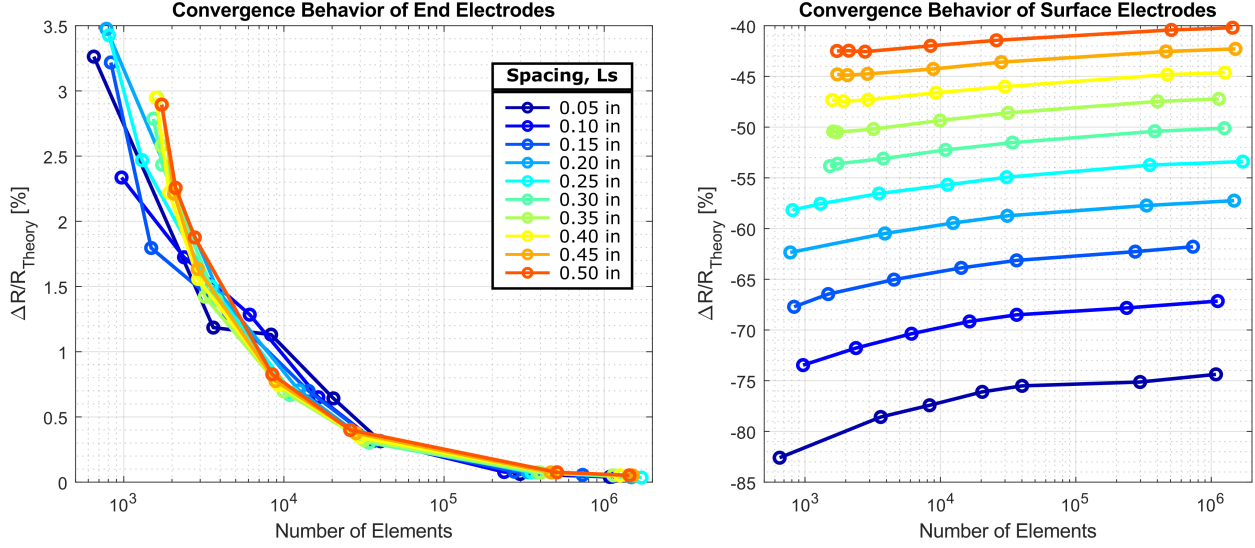
Figure 4.19. The convergence behavior of electrical resistance measurements from the end-covering (left) and surface-mounted electrodes (right) on a representative cylindrical body for various electrode spacing values.

The expression above facilitates strain state determination from surface-mounted electrical resistance measurements. It is important to note the limitations of this approach, particularly in regard to an implicit assumption of a constant strain state throughout the volume of the cylinder. This assumption becomes violated where there is a spatially varying strain distribution within the cylinder. For example, highly oscillatory wave propagation when the wavelength is smaller than the electrode separation distance. This was the premise motivating the exploration of electrode spacing-induced signal filtering in earlier investigations.

To determine the geometric correction factor as a function of electrode spacing (L_s), a finite element model (FEM) approach was employed. The analysis involved the use of 10 cylinder models, each with a different electrode spacing ranging from 0.05 in (1.27 mm) to 0.50 in (12.7 mm), in 0.05 in (1.27 mm) increments, while maintaining a constant electrode width of 0.25 in (6.35 mm). This specific range of electrode spacing distance was selected to explore the evolution of the geometric calibration factor in the neighborhood of the electrode spacing for the adjacent injection scheme. Furthermore, this specific scheme had the most pronounced piezoresistive behavior and minimized the violation of the critical assumption

of a non-varying strain state in the measurement region under dynamic wave packet loading conditions. Convergence analysis of the electrical resistance measurements from the electrode pairs was conducted for each cylinder model. The need for convergence analysis stems from the desire to obtain a more precise and reliable determination of the geometric correction factor. The overall mesh for the cylindrical body was refined with the finest discretization between the surface-mounted electrodes, as seen in Figure 4.18 (bottom). The process of producing a finer mesh discretization enables a potentially highly varying potential field to be adequately captured and resolved, which may influence the resistance measurements between the electrodes. In this convergence analysis effort, mesh refinement from $10^3 - 10^6$ elements was considered. Computational efficiencies that sped up these simulations are described in the Appendix.

The results of the convergence analysis for end-covering electrodes and surface-mounted electrodes are presented in Figure 4.19. A total of seven mesh refinements were conducted for each cylindrical model. The inter-electrode resistance measurements are normalized with respect to the theoretical resistance of the representative cylindrical body. The convergence behavior of the end-covering electrodes approaches a value of zero percent. This result is unsurprising on account of the resistance measurements from the end-covering electrodes are prismatic through the entire representative cylindrical body. Therefore, taking into account the defined physical geometry of the cylinder, the intrinsic resistivity will be calculated to be approximately equivalent to the analytical piezoresistivity model predictions for 1.5 wt.% CNF/epoxy. This observation is consistent across the various electrode spacing values explored for end-covering electrodes. However, the rate of convergence for the surface-mounted measurements is highly dependent on the inter-electrode spacing distance. It can be observed that mesh refinement produces a more accurate measure of the electrical resistance between the surface-mounted electrodes on account of large variations of the domain potential becoming better represented. Furthermore, convergence does occur as mesh refinement leads to smaller improvements in the measured resistance from the surface-mounted electrodes. In comparison to the theoretical resistance calculations, the placement of the surface-mounted electrodes consistently underestimates the resistance of the representative cylindrical body. This observation is consistent with the understanding current travels the path of least re-
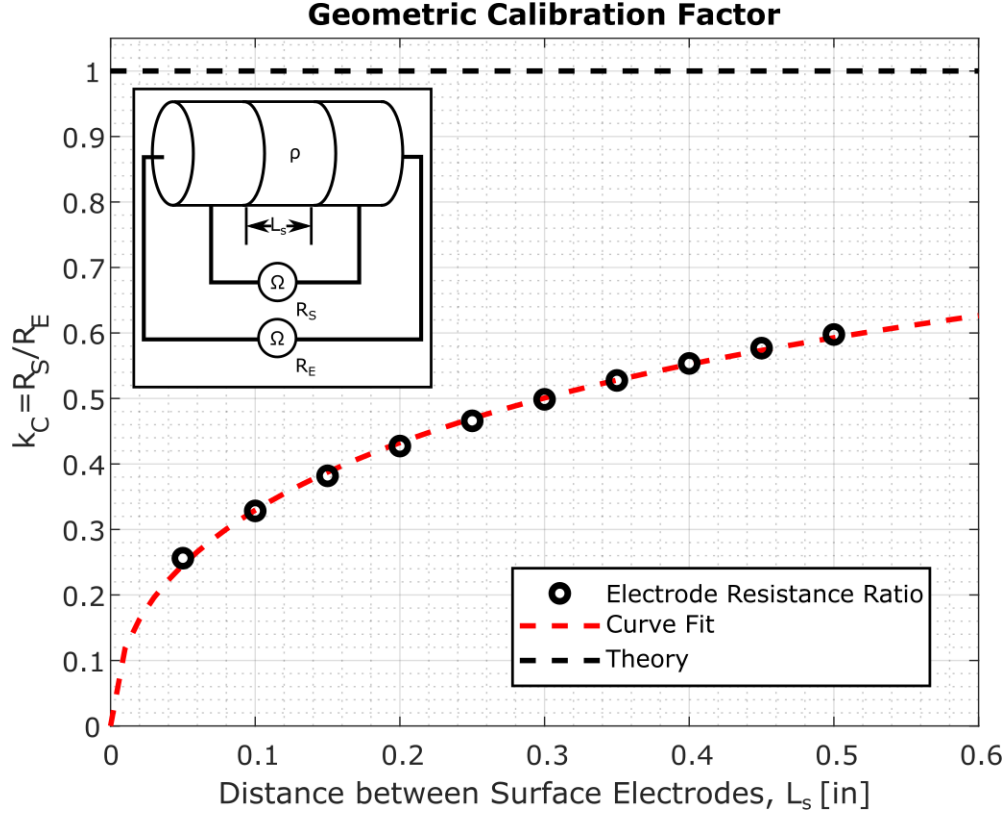
Figure 4.20. The geometric calibration factor is defined as the ratio of the resistance measurements taken from surface-mounted and end-covering electrodes on a representative cylindrical body (shown in the top-left schematic subplot). A ratio value of one denotes that the resistance measured by both sets of electrodes is equivalent. The geometric calibration factor is fitted onto an exponential curve $k_c = 1 - \exp(a \cdot L_s^b)$ with the fitting constants of $a = -1.273$ and $b = 0.5031$.

sistance. In the case of end-covering electrodes, electrons must travel through the entire material. For surface-mounted electrodes, electron movement covers a reduced distance.

Convergence of the electrical resistance measurements was determined based on the criteria that the relative improvement from the previous mesh refinement was less than 1% for end-covering and surface-mounted electrodes, respectively. Further improvements are possible but come at the expense of intense computational resources for marginal gains. As a result, electrical resistance measurements taken from the finest mesh were used to determine the geometric calibration factor. The quotient of the surface-covering and end-covering electrode resistance measurement as a function of the distance between the surface electrodes,

L_s, is plotted in Figure 4.20. An exponential function, $y = 1 - \exp(ax^b)$, was fit to the data points resulting in constants of $a = -1.273$ and $b = 0.5031$. The choice of fitting the data with the exponential equation was motivated to provide a physically meaningful interpretation of the data. The limits of the expression represent two distinct behaviors. At zero electrode spacing, the calibration factor is equal to zero and physically represents an electrical short across the surface-mounted electrodes. As the separation distance between the surface-mounted electrodes approaches infinity, the geometric correction factor approaches a value of one and physically represents nearly similar or identical resistance measurements between end-covering and surface-mounted electrodes. Furthermore, the coefficient of determination for the exponential curve fit is 0.9980; the high value of the coefficient of determination denotes good agreement between the data and the fit curve. For the purpose of piezo-inversion to determine the strain state from surface-mounted electrical resistance measurements, the geometric correction factor for a 0.25 in (6.35 mm) spacing is $k_c = 0.4695$.

ABAQUS Digital Twin

Digital twins are motivated by the need to accurately simulate and predict physical behavior through a virtual representation or model. Employing a digital twin enables enhanced understanding and interpretation of real-world data. To create a digital twin of the rod in ABAQUS, the initial step involves preprocessing of input signals and the estimation of material characteristics. In this work, the recorded behavior of the shaker system was utilized as the input to the model. More specifically, the ABAQUS model utilized a Dirichlet boundary condition at the mount via the double integration of the shaker accelerometer output as the applied displacement history. Prior to integrating the signal, a digital high-pass filter was applied to the recorded acceleration signal to eliminate offset DC bias. Employing a pass filter is an important preprocessing step to ensure that accumulated errors in integration are not included in the model. The high pass filter was created using MATLAB's digital signal processing toolbox with the following characteristics: 1 kHz stopband frequency, 60 dB stopband attenuation, 15 kHz passband frequency, 1 dB passband ripple, and sampling

frequency of 1.28 MHz. The effect of the high pass filter and the resulting displacement history used in ABAQUS is presented in Figure 4.21.

Given polymeric epoxy materials are well-known to have energy-dissipative properties under dynamic loading conditions, it is important to consider a method to incorporate these characteristics in the ABAQUS digital twin model. The most common computational method to incorporate the effect of energy-dissipative behavior in FEM software is the Rayleigh damping model. Rayleigh damping is a convenient method to incorporate energy-dissipative behavior by introducing a damping matrix, $[C] = \alpha[M] + \beta[K]$, into the equations of motion solved by FEM software. The damping matrix is constructed as a linear combination of the model matrices for mass, $[M]$, and stiffness, $[K]$, and the parameters α and β are independently defined. The mass-proportional coefficient α introduces damping forces that are proportional to particle movement or velocities and simulates energy loss through viscous behavior. The stiffness-proportional coefficient β introduces damping forces that are proportional to particle acceleration or strain rate and simulates damping associated with the material itself [120].

Gresil and Giuriguitiu [121] outlined the process to experimentally predict the Rayleigh damping coefficients using guided wave propagation in a carbon fiber reinforced polymer composite. The process was adapted for this work and is briefly outlined here. Consider the relationship between the wave damping coefficient, η, and the Rayleigh damping coefficients as a function of angular frequency, ω, as seen in the following equation,

$$\zeta = \frac{1}{2}\left(\frac{\alpha}{\omega} + \beta\omega\right) \tag{4.5}$$

Taking into account the experimental setup, vibrations are injected into the suspended CNF/epoxy rod at one end, and the rod is supported at the opposite end. This particular setup has the following two advantages for modeling purposes: 1) the prismatic geometry of the specimen allows the rod to behave as a waveguide, and 2) the adjacent media of the rod is air (excluding the mount and the tip). Therefore, it can be safe to assume energy-dissipative behaviors are due to the rod material as opposed to energy losses to the surrounding area
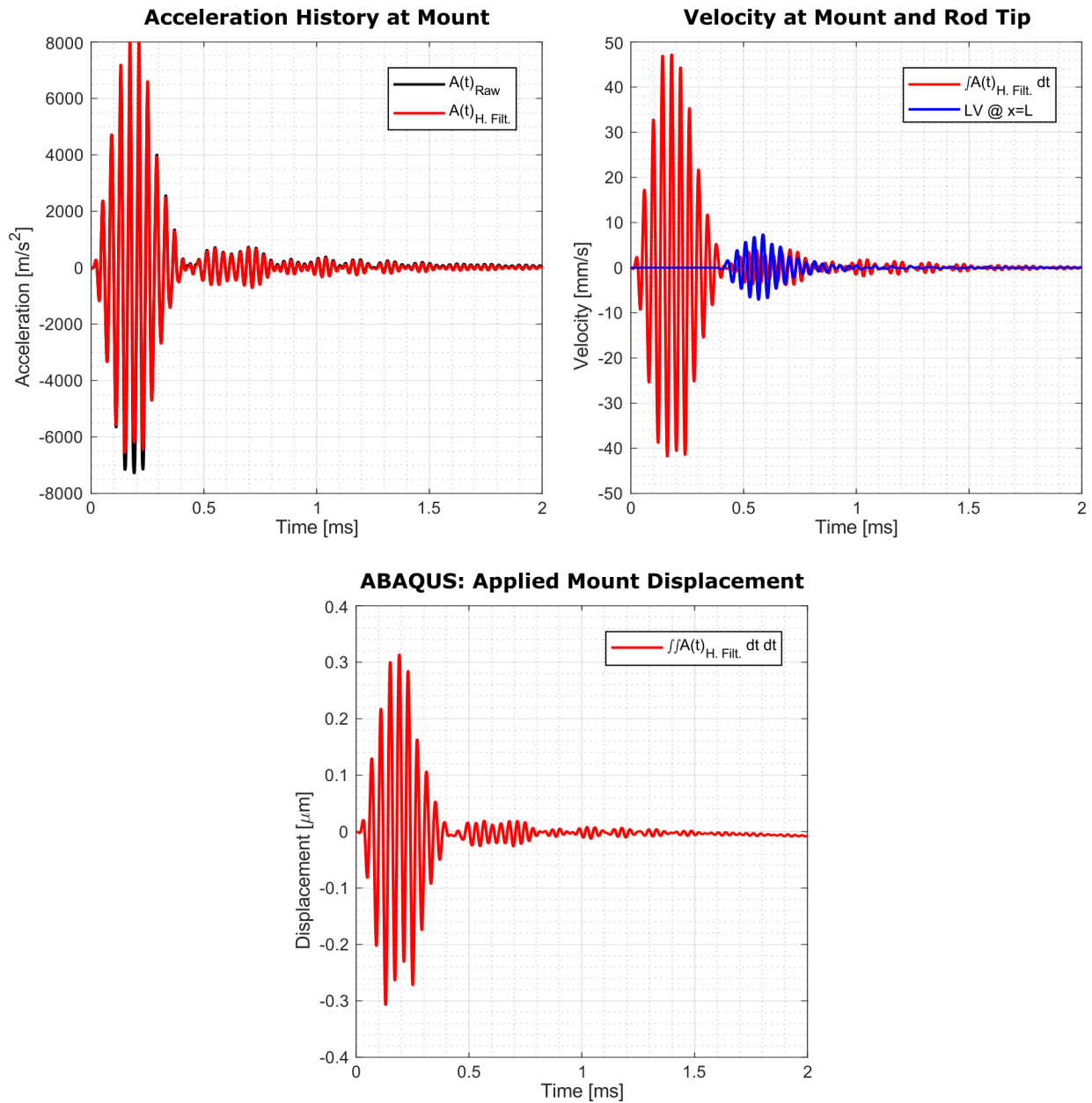
Figure 4.21. (a) A high pass filter is applied onto the raw shaker accelerometer output, shown in black. The filtered accelerometer signal, shown in red, has the bias voltage removed. (b) The velocity at the rod mount, calculated by integrating the filtered accelerometer signal once, is compared to the velocity at the rod tip, shown in blue, recorded by the LV system. (c) The displacement history used in ABAQUS at the mount was calculated by integrating the filtered accelerometer signal twice.

or the geometric spread of the wavefront. In the case of single-frequency wave propagation in the rod and energy-dissipative material, wave motion will take the form,

$$\phi(x,t) = \phi_0 e^{-\eta x} e^{i(\omega t - \gamma x)}. \tag{4.6}$$

The variables ϕ_0, η, ω, and γ denote the initial amplitude, structural wave damping coefficient, angular frequency, and wave number, respectively. The energy-dissipative behavior of the propagating wave, $\phi(x,t)$, is captured via $e^{-\eta x}$. The structural wave damping coefficient can be determined through curve fitting of the magnitude of the received signals at discrete locations of the waveguide. In order to relate the structural wave damping coefficient to the Rayleigh damping coefficients, the energy-dissipative component of the traveling wave equation is isolated,

$$e^{-\eta x} = e^{-\eta c_0 t}. \tag{4.7}$$

Where the relation, $x = c_0 t$, between propagation distance and elapsed time is enforced. Compared to the solution of a wave at a single location,

$$x = \phi_0 e^{-\zeta \omega t} e^{i\omega t}. \tag{4.8}$$

The two energy-dissipative components can be directly compared,

$$e^{-\zeta \omega t} = e^{-\eta c_0 t}. \tag{4.9}$$

Where the relationship between the structural wave damping coefficient and the material damping ratio can be obtained,

$$\zeta \omega = \eta c_0. \tag{4.10}$$

Substituting the Rayleigh damping expression, equation (4.5), into the previous equation and organizing terms, the relationship between the structural wave damping coefficient and the Rayleigh damping coefficients can be made as a function of angular frequency,

$$\eta = \frac{1}{2c_0}(\alpha + \beta\omega^2). \tag{4.11}$$

To experimentally estimate the Rayleigh damping coefficients, first, the piezo-inversion process was applied to the collected normalized resistance measurements. Second, a Hilbert transform was utilized to generate an envelope of the strain signal. Then, an exponential curve fit was applied to the amplitude values of the wave packet envelopes to ascertain the wave-damping coefficient. Figure 4.22 showcases the attenuation behavior observed as the wave packet travels along the length of the rod from piezo-inverted strain measurements. An exponential curve was fit to the maximum envelop values to determine the wave damping coefficient for 2.5/27.5 kHz wave packet loading. This process was performed for each measurement region along the length of the rod, starting with the 2.5/27.5 kHz wave packet excitation before continuing with the first ten measurement regions, ending with the 3.4/37.4 kHz wave packet excitation. These specific frequencies and electrode pairs were chosen on the basis of having the highest signal-to-noise ratio. Despite this, certain signals were suppressed in the curve-fitting process due to outlier behavior. The structural wave damping coefficients determined for each frequency and its corresponding coefficient of determination are presented in Table 4.7. For comparison, the same process was employed to calculate the wave-damping coefficient from the extrinsic measurements of the LV system at the specimen tip and the integrated velocity signal from the shaker mount accelerometer. On account that only two extrinsic data points are known, the two fitting parameters are calculated directly. Following the determination of the structural wave damping coefficient as a function of frequency, a subsequent curve fit using equation (4.11) was applied.

Through this process, the Rayleigh damping coefficients were estimated to have the following values for piezo-inversion strains, $(\alpha, \beta)_{piezo} = (7.9664 \times 10^{-11}, 3.5701 \times 10^{-7})$, and for extrinsic values, $(\alpha, \beta)_{ext.} = (7.8843 \times 10^{-11}, 5.5202 \times 10^{-7})$. Several notable observations can be made from the process of estimating the Rayleigh damping coefficients. First, there was a general positive correlation between the structural wave-damping coefficient and excitation frequency. In the context of Rayleigh damping, this finding suggests that the energy-dissipative behavior at the range of frequencies investigated is primarily driven by
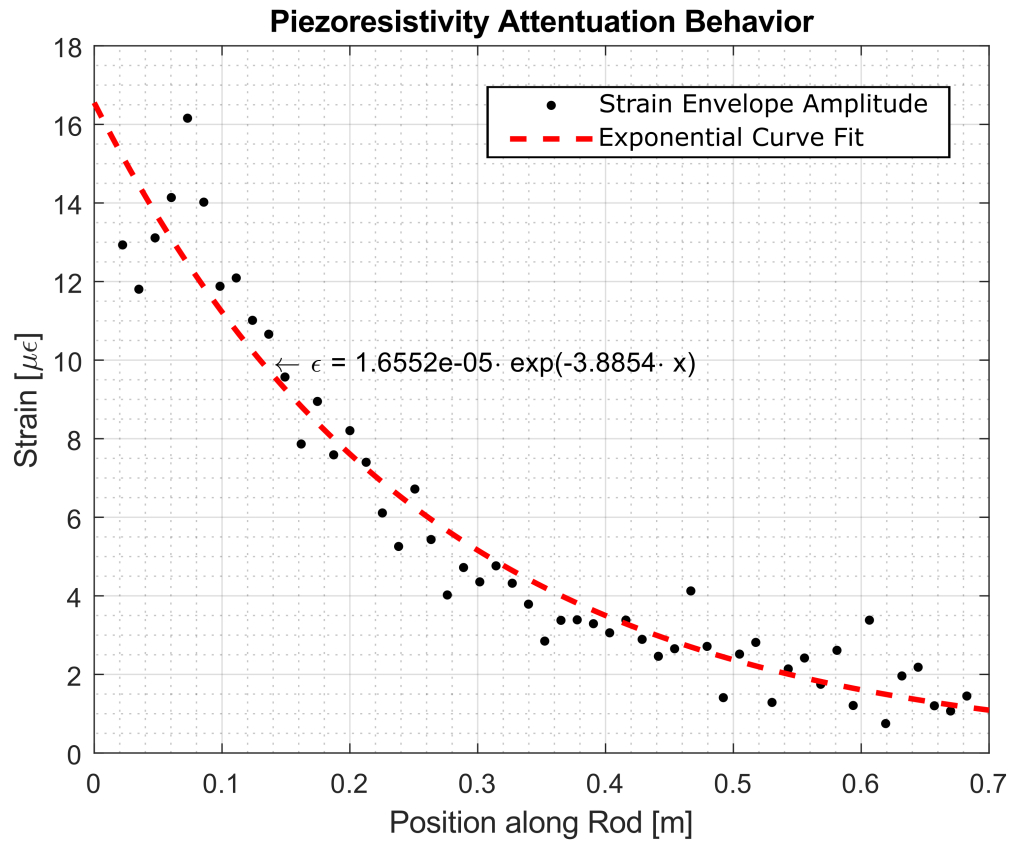
Figure 4.22. An exponential curve, $\epsilon = \epsilon_0 e^{-\eta x}$, is fitted onto the maximum amplitude of the strain history calculated from the piezo-inversion process for each measurement region of the 1.5 wt.% CNF/epoxy rod. The decay of the excitation amplitude denotes the apparent attenuation of the wave packet as it travels along the rod.

Piezo-Inversion Strain Determined Structural Damping									
f_m [kHz]	27.5	28.6	29.7	30.8	31.9	33	34.1	35.2	36.3	37.4
η_{piezo}	3.885	4.586	6.387	6.291	4.576	4.956	7.932	8.422	8.104	7.119
R^2	0.937	0.525	0.824	0.869	0.272	0.815	0.929	0.722	0.853	0.845
Extrinsic Velocity Determined Structural Damping									
$\eta_{ext.}$	2.712	3.232	3.523	3.408	3.447	3.995	4.850	4.937	5.241	5.901

Table 4.7. The structural wave damping coefficients of the 1.5 wt.% CN-F/epoxy rod was determined from piezo-inverted strains and extrinsic velocity measurements.

stiffness-proportional damping rather than mass-proportional damping. This is evident from the fact that there is a four-order of magnitude difference between the stiffness-proportional damping coefficient, β, and the mass-proportional damping coefficient, α. The larger value of β indicates that the response of the system is more influenced by strain rate or the material itself. Second, the goodness of fit was assessed through the coefficient of determination. The Rayleigh damping coefficient fitting process with the piezo-inversion determined strain signals and extrinsic measurements produced $R^2_{piezo} = 0.5432$ and $R^2_{ext} = 0.9116$, respectively. Although the coefficient of determination value from the piezo-inversion determined strain signals is not particularly high, the fit can still be considered satisfactory as the values of the estimated Rayleigh coefficients are comparable to extrinsic validation.

An explicit elastodynamic ABAQUS analysis was carried out on a simulated 1.5 wt.% CNF/epoxy rod to evaluate the capability of the proposed piezo-inversion process to recover the strain state within the electrode measurement region accurately. As a digital twin, the virtual representation of the nanocomposite rod was designed to accurately reflect the physical and loading conditions of the real-world experiment. The model was constructed with the material and simulation parameters defined in Table 4.8. The value of the modulus of elasticity utilized in this model corresponds to the dynamic modulus determined from previous high-strain-rate impact testing. The contribution of nanofillers to the density of the CNF/epoxy material is assumed to be negligible, and this physical property was extracted from the material data sheet provided by the manufacturer. The Poisson's ratio was not directly evaluated in this investigation, but Koo and Tallman [59] conducted mechanical characterization for the same Class 2000 Laminating Epoxy System (FibreGlast) with CNF
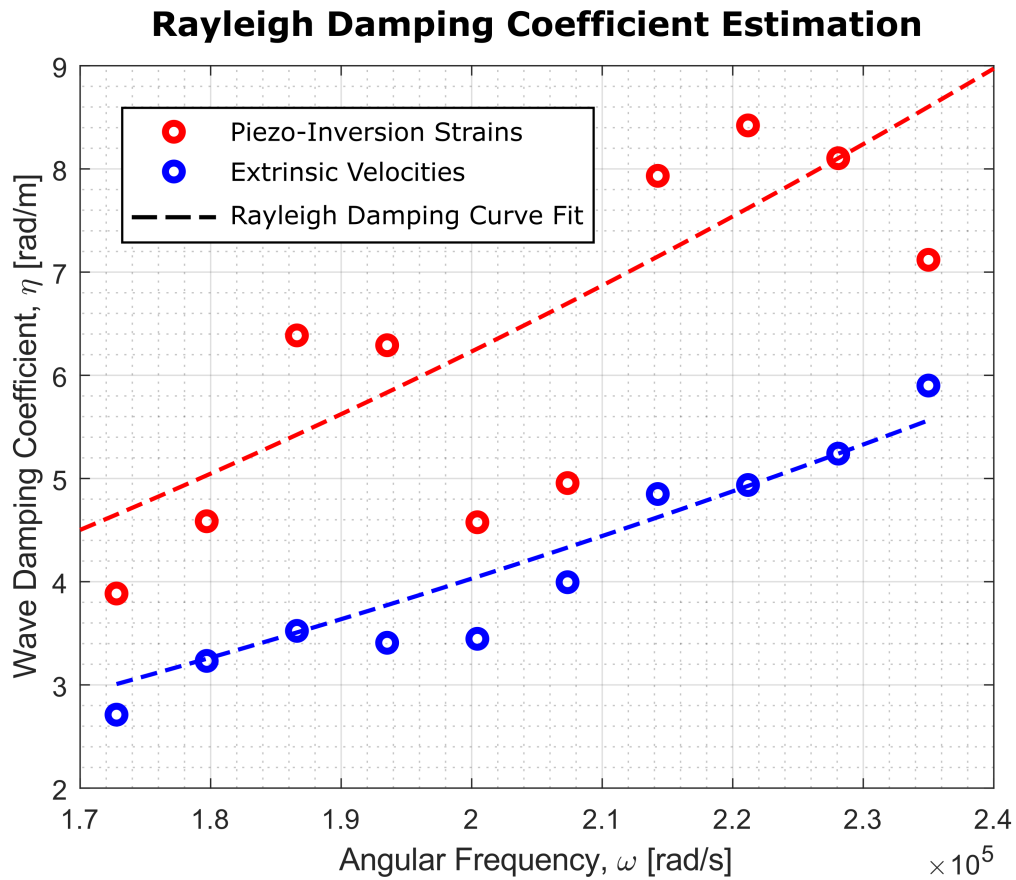
Figure 4.23. The Rayleigh damping coefficients were estimated from piezo-inversion strain and extrinsic measurements. The wave damping coefficients were determined from the attenuation of the collected piezoresistivity measurements on the 1.5 wt.% CNF/epoxy rod.

Model Material Property	
E [GPa]	3.56
ν [$\sim$]	0.351
ρ [kg/m^3]	1134
ABAQUS Explicit Simulation Parameters	
Number of elements	43,220
Number of nodes	9,984
Step time, Δt [μs]	0.02
α [1/s]	0, 7.8843$\times 10^{-11}$, 7.9664$\times 10^{-11}$
β [s]	0, 5.5202$\times 10^{-7}$, 3.5701$\times 10^{-7}$

Table 4.8. Material properties for 1.5 wt.% CNF/epoxy and simulation parameters necessary to conduct an explicit elastodynamic ABAQUS analysis.

inclusions; the experimentally determined Poisson's ratio is assumed comparable and utilized in the simulation effort. The impact of an inaccurate Poisson's ratio is negligible due to the fact that the rod is axially loaded with a planar stress wave, and axial strains are of interest for validation purposes of the piezo-inversion process. Three combinations of Rayleigh damping coefficients were investigated. 1) undamped case, 2) extrinsically-determined damping $(\alpha, \beta)_{ext.} = (7.9664 \times 10^{-11}, 3.5701 \times 10^{-7})$, and 3) piezoresistive-determined damping (via strain determination form piezo-inversion) $(\alpha, \beta)_{piezo} = (7.8843 \times 10^{-11}, 5.5202 \times 10^{-7})$. A step time of 20 ns was utilized in each elastodynamic simulation, regardless of the values of the Rayleigh damping coefficients. A small step time was utilized to ensure numerical stability and accurately capture wave propagation behavior within the model.

The ABAQUS simulation results were post-processed by first transforming the provided logarithmic strain to engineering strain and then computing the volumetric strain average of the measurement regions between surface-mounted electrodes. The motivation for these post-processing steps is to have an equivalent comparison to the strains calculated through the piezo-inversion process from surface-mounted normalized resistance measurements. The engineering strains obtained from the ABAQUS digital twin are compared to the piezo-inverted strains in Figure 4.24 at three distinct locations along the length of the rod: $x = 73$ mm, 200 mm, and 505 mm. These locations are near the mount, mid-span, and end of the rod. These locations also align with the center of the measurement region for the 4'th, 14'th, and 38'th electrode pair, respectively.
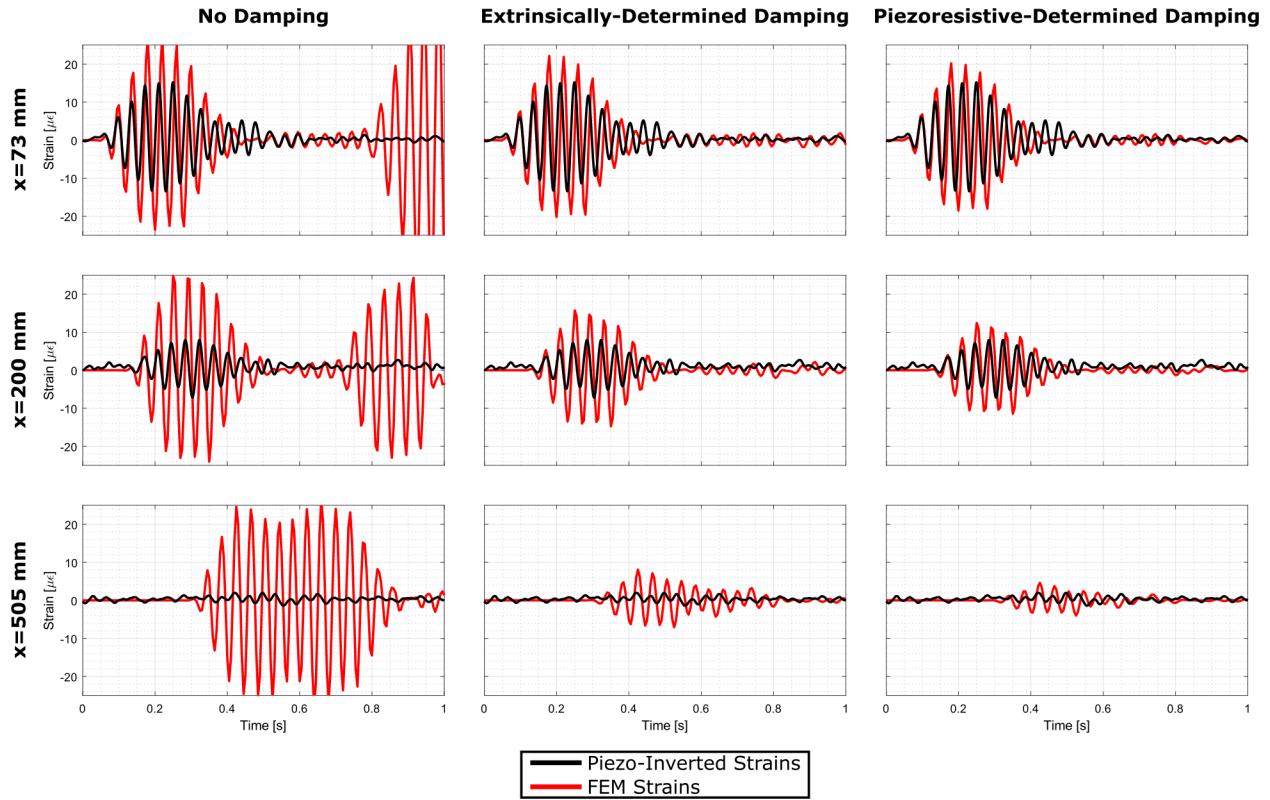
Figure 4.24. The piezo-inverted strains were compared to the strains obtained from the ABAQUS digital twin model at three locations (rows). Three cases of damping or energy-dissipative behaviors were considered: (left column) undamped, (center column) Rayleigh damping coefficients determined from the extrinsic velocity measurements $(\alpha, \beta)_{ext.}$, and (right column) Rayleigh damping coefficients determined from direct piezo-inverted strains from the rod $(\alpha, \beta)_{piezo}$. The behavior of the digital twin more closely matches piezo-inverted strains after damping was included in the elastodynamic simulation.

Numerous intriguing observations can be made when comparing the piezo-inverted strains to the strains obtained from the ABAQUS digital twin. First, the physical material properties provided in the elastodynamic FEM accurately predict the arrival of the wave packet at the measurement regions along the length of the rod. This is unsurprising as these properties are based on previously experimentally determined values and manufacturer provided. Furthermore, the Rayleigh damping coefficients do not impact the propagation velocity of stress waves and are solely a computational tool to model or simulate energy-dissipative behavior. This leads to the second important observation: incorporating the Rayleigh damping coefficients yields dramatic improvements in predicting the overall magnitude of the wave packet as it travels along the length of the rod. In other words, the attenuation behavior is observed when Rayleigh damping is incorporated. When extrinsically-determined Rayleigh damping coefficients are utilized, the piezo-inverted strain magnitude is approximately 30% smaller than the FEM strain magnitude at 73 mm from the mount. This difference increases to approximately 50% at 200 mm. However, a comparison near the end of the rod can not be made because the measurements from the rod can be considered purely noise. In contrast, the piezoresistive-determined Rayleigh damping coefficients provide a more accurate prediction of the attenuation behavior observed in the recorded measurements of the rod. This finding is anticipated considering the direct incorporation of piezo-inverted strain information into the updated digital twin model. To emphasize the significance of these observations, these results highlight an exceptionally promising capability of the modeling processes previously outlined to harness information derived from piezoresistive measurements at certain or few locations to construct a remarkably accurate digital twin model. This showcases the possibility of precise modeling of comprehensive material and full-field behavior, even from a sparse spatial sensor array and with low strain magnitude measurements.

4.4 Summary and Conclusions

This chapter presented the results of the three main experimental efforts performed in this thesis utilizing self-sensing piezoresistive nanofiller-modified epoxy-rods: 1) high strain-rate impact testing, 2) steady-state vibrations, and 3) wave packet excitation.

An SHPB apparatus was utilized to investigate the behavior of CB, CNF, and MWCNT epoxy rods under highly dynamic and transient loading conditions. Planar stress waves, with the shape of a bilinear or triangular profile, were produced by an impacting striker bar and pulse shaper on the incident bar. The planar stress waves were injected into the nanofiller-modified epoxy rods while simultaneously recording voltage changes, due to changes in material resistance, in an electrode region at the center of the rod specimens. Two SHPB apparatus configurations were utilized to investigate the effects of different rod boundary conditions on the injected stress wave: compression-only and alternating states of tension and compression. The elastic speed of sound of a longitudinal wave was calculated from the reflected stress waves observed in the piezoresistive measurements. The calculated elastic wave speeds for each material were found to be in good agreement with extrinsic validation from the SHPB incident and transmission bar components. Furthermore, The decay of the injected stress wave in compression and tension was examined to highlight nonlinear piezoresistive behavior (i.e., greater strain sensitivity in tension than in compression). Small short-aspect ratio cylindrical samples were prepared and subject to traditional SHPB testing to assess the dynamic behavior of nanofiller-modified epoxy material at high strain rates. It was found that nanofiller inclusions had a minor enhancing effect on the dynamic stiffness, from 3.24 to 3.59 GPa, compared to neat or unmodified epoxy material at strain rates between 230–235 s^{-1}.

Next, the CNF-modified epoxy rod structure used in the high-rate impact loading investigation was repurposed in a new experiment to investigate steady-state vibration behavior. The 1.5 wt.% CNF/epoxy rod was mounted in an open-loop piezoelectric/ferromagnetic shaker system and excited under harmonic sinusoidal loading conditions. To measure the piezoresistive response of the rod, the electrodes were interfaced in a modified Wheatstone bridge circuit, and the output of the bridge was amplified by 1000 through an operational amplifier before being recorded by a separate oscilloscope. Frequencies ranging from 500 Hz to 50 kHz were explored. Raw Wheatstone voltage measurements contained significant noise and were considerably low amplitude (approximately ±20 mV) despite being amplified. Analysis of the collected signals in the frequency domain revealed considerable low-frequency noise. However, a prominent peak at the expected excitation frequency was present for all

tests. Employing a bandpass filter at $\pm$ 10% of the excitation frequency led to considerable improvements and more clearly revealed the steady-state perturbation. A major insight gleaned from this contribution was that the piezoresistive response carries essential information despite the presence of EMI or other environmental factors.

Finally, wave tracking was achieved on slender long-aspect ratio CNF/epoxy rods using spatially-distributed and surface-mounted electrodes. Three specific efforts were pursued in this investigation: 1) electrode spacing-induced signal filtering, 2) characterization of dynamic behavior, and 3) strain state determination through analytical and computational means. CNF-modified epoxy rods were manufactured with weight fractions of 1.0 wt.%, 1.25 wt.%, and 1.5 wt.% CNF relative to epoxy mass. The rods were prepared, and circumferential electrodes were applied along its length. The same shaker system from the previous investigation was utilized to inject highly-controlled 5.5-cycle modulated wave packets and simultaneously measure the piezoresistive response from the rod through electrode pairs. Drawing insights gained from the previous investigation, a closed-loop system was constructed to create an experimental setup to produce highly-repeatable wave packet injection and piezoresistive measurements. These improvements enabled the utilization of ensemble averaging to improve the signal-to-noise ratio of the collected measurements dramatically. It was found that surface-mounted measurements from the CNF/epoxy rods were able to accurately track the position of a wave packet as it traveled along the length of the rod. Surprisingly, the 1.5 wt.% CNF/epoxy rod exhibited the greatest sensitivity to wave packet excitation compared to that of the 1.0 wt.% and 1.25 wt.% CNF/epoxy rods. This result is counter-intuitive as the nanofiller concentrations at weight fractions closer to the percolation threshold exhibit greater strain sensitivity. However, due to the exceptionally low amplitude excitement caused by the wave packet, it is hypothesized the main driver of piezoresistive behavior in this situation is driven by changes to the contact impedance of direct nanofiller-to-nanofiller interactions as opposed to electron tunneling behavior. Adjustable electrode spacing did indeed show an artificial filtering effect on the collected signals. This is because a larger portion of the wave packet is contained within the measurement region and the effects of alternating tension and compression balance. On account that wave packets with a span of modulation frequencies were considered, efforts were made to estimate the

group velocity to investigate possible dispersion behaviors. It was observed the piezoresistive response signals are unreliable in accurately estimating the group velocity compared to extrinsic verification. Larger magnitude wave packet citations are necessary to elicit a larger piezoresistive response to feasibly utilize the Hilbert transform approach to conduct this analysis. This leads to the final effort of this investigation; to extract axial strains from piezoresistive measurements. This was achieved by leveraging an analytical piezoresistivity model based on first-principle physics to inversely determine the strain state from the normalized resistance measurements taken from the surface-mounted electrodes. The model was calibrated for CNF/epoxy material system, and a linear curve fit was applied on the normalized resistivity curve for an infinitesimally small strain range. To aid in the piezo-inversion process, the CEM was employed to create an implicit geometric calibration factor that equates normalized resistance measurements taken from surface-mounted electrodes to the change in innate electrical resistivity in the measurement region. An ABAQUS digital twin was created to compare the piezo-inversion strains against FEM-determined strains. To aid in this process, the Rayleigh damping coefficients were estimated using the piezo-inversion strains and extrinsic measurements (i.e., shake accelerometer at the mount and velocity at the rod tip). It was found that piezo-inversion strains fairly accurately predicted the actual strain state of the rod when compared to the ABAQUS digital twin when the estimated Rayleigh damping coefficients were employed. These results open the door to a new era of insights into complex material-level dynamics or transient loading conditions.

5. SUMMARY OF SCHOLARLY CONTRIBUTIONS AND BROADER IMPACTS

5.1 Leveraging the piezoresistive-effect for sensing of high-rate and dynamic behavior

The work presented in this dissertation clearly demonstrated dynamic piezoresistivity could capture high-rate impact stress waves, steady-state vibrations, and highly–repeatable wave packets transmitted into self-sensing rod structures. This was achieved by simultaneous direct current injection and voltage measurements as the stress waves propagated through the rod structure. This is an important contribution to the state of the art because in-situ material characterization can be conducted, and insights such as the material wave speed, dynamic modulus, and excitation frequencies can be made.

5.2 Demonstration of passive signal filtering for dynamic electrical measurements applications

The design of the electrodes was illustrated to have a direct effect on the signal condition of electrical measurements from the nanocomposite rods. Adjusting the spacing between electrode pairs demonstrated a filtering effect on dynamic piezoresistivity. These findings highlight the potential to tailor electrode topology to selectively enhance or attenuate frequency components. This is an important contribution to the state of the art because signal-specific electrode topologies are an additional tool to achieve passive filtering or conditioning without ancillary electrical components (e.g., resistors, capacitors, inductors, or operational amplifiers) in the form of signal-specific electrodes.

5.3 Piezoresistivity-enabled recovery of material dynamic response and properties

The third contribution of this dissertation was to derive dynamic material responses and properties from piezoresistive measurements. By exploiting the inherent coupling between mechanical deformation and electrical resistance, piezoresistive materials enable direct monitoring of deformation-induced changes with simple electrical measurements. This unique

capability enables in-situ material-state determination in combination with an analytical piezoresistivity model to inversely determine the exact strains in highly dynamic loading conditions. Furthermore, full-field mechanics can be assessed through a digital twin.

6. RECOMMENDATIONS FOR FUTURE WORK

This thesis has presented an effort to understand the basic principles of dynamic material state awareness by the piezoresistive effect. Although the particular nanofillers utilized in the work herein are carbon-based (e.g., CB, CNF, MWCNT) and were dispersed into a thermoset epoxy, these nanocomposite materials serve merely as suitable examples to demonstrate the broader applicability of piezoresistivity in directly capturing and characterizing dynamic behavior. In other words, the piezoresistive effect enables accurate insights into the mechanical state and intrinsic mechanical properties of self-materials. This chapter identifies some of the limitations of the efforts contained in this dissertation and offers suggestions for where future research efforts can make meaningful advancements.

1. **Expand Piezoresistive Elastodynamics to 3D**: This thesis marks a significant milestone in the first-ever exploration of piezoresistive elastodynamics to obtain material state awareness through dynamic self-sensing principles. The principles developed in this thesis can be applied to real components of interest such as geological strata and mineralogy, anatomical structures and biological tissues, composite structures and cements, and energetic materials. These examples are not all-inclusive but are obviously geometrically complex and mechanically anisotropic. Undoubtedly, future studies must delve into the mechanical and geometric factors that influence elastodynamic behavior and their effect on dynamic piezoresistivity. By investigating this connection, we can recover invaluable insights into the behavior of real-world components in an unprecedented way.

2. **Obtain Full-Field Mechanics**: One possible natural extension of this thesis is to integrate dynamic piezoresistivity with tomographic methods, specifically electrical impedance tomography (EIT) [66]. EIT reconstructs the interior conductivity distribution from electrode voltage measurements at the boundary of the domain. This work has proven that dynamic piezoresistivity can capture elastodynamic behavior, and combining this insight with EIT could enable capturing internal dynamic behavior through a reconstruction of the body's change in electrical conductivity. Furthermore,

by addressing the conductivity-to-strain inverse problem to EIT domain conductivity reconstructions, it becomes possible to obtain the complete strain state and potentially garner greater or more detailed mechanical characterization.

3. **Extending Piezoresistive Elastodynamics to Adjacent Fields**: The principles of piezoresistive elastodynamics have great potential in a wide range of materials that exhibit self-sensing properties, and their extension to adjacent fields is not out of the realm of imagination. By harnessing the intrinsic coupling between mechanical deformation and electrical properties, possible applications can be envisioned in other fields, such as geological, biomedical, and highly energetic materials. For geological applications, piezoresistive elastodynamics could be combined with borehole seismic surveys and produce a novel method for resource detection under certain environmental or mineralogical conditions [122] [123]. In biomedical applications, piezoresistive elastodynamics may complement current elastography applications and improve medical diagnostic capabilities or monitor soft-tissue medical treatments [82] [83] [84] [124] [125]. Applications in highly energetic materials are a promising area as explosives or propellants undergo rapid and complex deformation processes during combustion or detonation. Integrating the piezoresistive effect into explosive binders may provide a possible method to directly monitor dynamic shock waves and other detonation characteristics [126] [127] [128]. This may be achieved by transmitting elastic stress waves across the binder or capturing acoustic emissions as it detonates and simultaneously measuring its dynamic piezoresistive behavior. Insights gained may lead to improvements in explosive yields from refinements in compaction or the design of energetic materials. In summary, the principles of piezoresistive elastodynamics have the potential to be extended well beyond the materials explored in this dissertation by recognizing that self-sensing is the base and key premise of this new and exciting field.

REFERENCES

[1] J. Achenbach, *Wave propagation in elastic solids*. Elsevier, 2012.

[2] K. F. Graff, *Wave motion in elastic solids*. Courier Corporation, 2012.

[3] K. Aki and P. G. Richards, *Quantitative Seismology: theory and methods. 1*. Freeman, 1980.

[4] D. W. Eaton, B. Milkereit, and M. Salisbury, "Seismic methods for deep mineral exploration: Mature technologies adapted to new targets," *The leading edge*, vol. 22, no. 6, pp. 580–585, 2003.

[5] J. D. Bass, S. V. Sinogeikin, and B. Li, "Elastic properties of minerals: A key for understanding the composition and temperature of earth's interior," *Elements*, vol. 4, no. 3, pp. 165–170, 2008.

[6] A. Malehmir, R. Durrheim, G. Bellefleur, *et al.*, "Seismic methods in mineral exploration and mine planning: A general overview of past and present case histories and a look into the futureseismic methods for mineral exploration," *Geophysics*, vol. 77, no. 5, WC173–WC190, 2012.

[7] B. T. Archer, Y.-h. Chao, J. M. Cormack, K. Kim, K. S. Spratt, and M. F. Hamilton, "Longitudinal motion of focused shear wave beams in soft elastic media," *The Journal of the Acoustical Society of America*, vol. 153, no. 3, pp. 1591–1599, 2023.

[8] M. Fatemi, A. Manduca, and J. F. Greenleaf, "Imaging elastic properties of biological tissues by low-frequency harmonic vibration," *Proceedings of the IEEE*, vol. 91, no. 10, pp. 1503–1519, 2003.

[9] A. Sarvazyan, T. J Hall, M. W Urban, M. Fatemi, S. R Aglyamov, and B. S Garra, "An overview of elastography-an emerging branch of medical imaging," *Current Medical Imaging*, vol. 7, no. 4, pp. 255–282, 2011.

[10] Y.-c. Fung, *Biomechanics: mechanical properties of living tissues*. Springer Science & Business Media, 2013.

[11] R. C. Asher, "Ultrasonic sensors in the chemical and process industries," *Journal of Physics E: Scientific Instruments*, vol. 16, no. 10, p. 959, 1983.

[12] M. T. M. Khairi, S. Ibrahim, M. A. M. Yunus, *et al.*, "Ultrasound computed tomography for material inspection: Principles, design and applications," *Measurement*, vol. 146, pp. 490–523, 2019.

[13] G. Chen, G. Liang, D. Xu, *et al.*, "Application of a shallow seismic reflection method to the exploration of a gold deposit," *Journal of Geophysics and Engineering*, vol. 1, no. 1, pp. 12–16, 2004.

[14] M. Markovic, G. Maries, A. Malehmir, *et al.*, "Deep reflection seismic imaging of iron-oxide deposits in the ludvika mining area of central sweden," *Geophysical Prospecting*, vol. 68, no. 1-Cost-Effective and Innovative Mineral Exploration Solutions, pp. 7–23, 2020.

[15] E. Koivisto, A. Malehmir, P. Heikkinen, S. Heinonen, and I. Kukkonen, "2d reflection seismic investigations at the kevitsa ni-cu-pge deposit, northern finland2d seismics at the kevitsa ni-cu-pge deposit," *Geophysics*, vol. 77, no. 5, WC149–WC162, 2012.

[16] A. Malehmir, C. Juhlin, C. Wijns, M. Urosevic, P. Valasti, and E. Koivisto, "3d reflection seismic imaging for open-pit mine planning and deep exploration in the kevitsa ni-cu-pge deposit, northern finland3d seismics for mine planning and exploration," *Geophysics*, vol. 77, no. 5, WC95–WC108, 2012.

[17] W. W. Symes, "The seismic reflection inverse problem," *Inverse problems*, vol. 25, no. 12, p. 123 008, 2009.

[18] J. M. Gosselin, S. E. Dosso, A. Askan, M. Wathelet, A. Savvaidis, and J. F. Cassidy, "A review of inverse methods in seismic site characterization," *Journal of Seismology*, vol. 26, no. 4, pp. 781–821, 2022.

[19] L. Sandrin, B. Fourquet, J.-M. Hasquenoph, *et al.*, "Transient elastography: A new noninvasive method for assessment of hepatic fibrosis," *Ultrasound in medicine & biology*, vol. 29, no. 12, pp. 1705–1713, 2003.

[20] R. Li, X. Qian, C. Gong, *et al.*, "Simultaneous assessment of the whole eye biomechanics using ultrasonic elastography," *IEEE Transactions on Biomedical Engineering*, 2022.

[21] C.-C. Shih, P.-Y. Chen, T. Ma, Q. Zhou, K. K. Shung, and C.-C. Huang, "Development of an intravascular ultrasound elastography based on a dual-element transducer," *Royal Society open science*, vol. 5, no. 4, p. 180 138, 2018.

[22] A. M. Alfuraih, P. O'Connor, A. L. Tan, *et al.*, "Muscle shear wave elastography in idiopathic inflammatory myopathies: A case–control study with mri correlation," *Skeletal radiology*, vol. 48, pp. 1209–1219, 2019.

[23] Y. K. Mariappan, K. J. Glaser, and R. L. Ehman, "Magnetic resonance elastography: A review," *Clinical anatomy*, vol. 23, no. 5, pp. 497–511, 2010.

[24] S. Singh, S. K. Venkatesh, Z. Wang, *et al.*, "Diagnostic performance of magnetic reso- nance elastography in staging liver fibrosis: A systematic review and meta-analysis of indi- vidual participant data," *Clinical Gastroenterology and Hepatology*, vol. 13, no. 3, pp. 440– 451, 2015.

[25] K. C. Siegmann, T. Xydeas, R. Sinkus, B. Kraemer, U. Vogel, and C. D. Claussen, "Diagnostic value of mr elastography in addition to contrast-enhanced mr imaging of the breast—initial clinical results," *European radiology*, vol. 20, pp. 318–325, 2010.

[26] L. Xu, Y. Lin, J. Han, Z. Xi, H. Shen, and P. Gao, "Magnetic resonance elastography of brain tumors: Preliminary results," *Acta radiologica*, vol. 48, no. 3, pp. 327–330, 2007.

[27] A. R. Damughatla, B. Raterman, T. Sharkey-Toppen, *et al.*, "Quantification of aortic stiffness using mr elastography and its comparison to mri-based pulse wave velocity," *Journal of Magnetic Resonance Imaging*, vol. 41, no. 1, pp. 44–51, 2015.

[28] A. F. (F. Grandt, *Fundamentals of structural integrity : damage tolerant design and nondestructive evaluation*, eng. Hoboken, N.J: J. Wiley, 2003, ISBN: 0471214590.

[29] *Structural health monitoring* (ISTE ; v.90), eng. London ; ISTE, 2006, ISBN: 1-280- 51053-6.

[30] D. Adams, *Health monitoring of structural materials and components methods with applications*, eng. Chichester, England ; John Wiley Sons, 2007, ISBN: 1-280-90089-X.

[31] C. Willberg, S. Duczek, J. M. Vivar-Perez, and Z. B. Ahmad, "Simulation methods for guided wave-based structural health monitoring: A review," *Applied Mechanics Reviews*, vol. 67, no. 1, 2015.

[32] M. Mitra and S. Gopalakrishnan, "Guided wave based structural health monitoring: A review," *Smart Materials and Structures*, vol. 25, no. 5, p. 053 001, 2016.

[33] L. Capineri and A. Bulletti, "Ultrasonic guided-waves sensors and integrated structural health monitoring systems for impact detection and localization: A review," *Sensors*, vol. 21, no. 9, p. 2929, 2021.

[34] F. Ricci, E. Monaco, N. Boffa, L. Maio, and V. Memmolo, "Guided waves for struc- tural health monitoring in composites: A review and implementation strategies," *Progress in Aerospace Sciences*, vol. 129, p. 100 790, 2022.

[35] W. Li, Y. Xu, N. Hu, and M. Deng, "Impact damage detection in composites using a guided wave mixing technique," *Measurement Science and Technology*, vol. 31, no. 1, p. 014 001, 2019.

[36] M. H. Sherafat, N. Quaegebeur, P. Hubert, L. Lessard, and P. Masson, "Experimental model of impact damage for guided wave-based inspection of composites," *Journal of Nondestructive Evaluation, Diagnostics and Prognostics of Engineering Systems*, vol. 1, no. 4, 2018.

[37] R. D. Finlayson, M. Friesel, M. Carlos, P. Cole, and J. Lenain, "Health monitoring of aerospace structures with acoustic emission and acousto-ultrasonics," *Insight*, 2001.

[38] J. Dos Reis, C. Oliveira Costa, and J. Sá da Costa, "Strain gauges debonding fault detection for structural health monitoring," *Structural Control and Health Monitoring*, vol. 25, no. 12, e2264, 2018.

[39] A. Sabato, C. Niezrecki, and G. Fortino, "Wireless mems-based accelerometer sensor boards for structural vibration monitoring: A review," *IEEE Sensors Journal*, vol. 17, no. 2, pp. 226–235, 2016.

[40] P. Ragam and N. Devidas Sahebraoji, "Application of mems-based accelerometer wireless sensor systems for monitoring of blast-induced ground vibration and structural health: A review," *IET Wireless Sensor Systems*, vol. 9, no. 3, pp. 103–109, 2019.

[41] C. K. Leung, K. T. Wan, D. Inaudi, *et al.*, "Optical fiber sensors for civil engineering applications," *Materials and Structures*, vol. 48, pp. 871–906, 2015.

[42] M. Drissi-Habti, V. Raman, A. Khadour, and S. Timorian, "Fiber optic sensor embedment study for multi-parameter strain sensing," *Sensors*, vol. 17, no. 4, p. 667, 2017.

[43] A. Huijer, C. Kassapoglou, and L. Pahlavan, "Acoustic emission monitoring of carbon fibre reinforced composites with embedded sensors for in-situ damage identification," *Sensors*, vol. 21, no. 20, p. 6926, 2021.

[44] M. Dziendzikowski, P. Niedbala, A. Kurnyta, K. Kowalczyk, and K. Dragan, "Structural health monitoring of a composite panel based on pzt sensors and a transfer impedance framework," *Sensors*, vol. 18, no. 5, p. 1521, 2018.

[45] S. Singh, J. A. Krishnaswamy, and R. Melnik, "Biological cells and coupled electro-mechanical effects: The role of organelles, microtubules, and nonlocal contributions," *journal of the mechanical behavior of biomedical materials*, vol. 110, p. 103 859, 2020.

[46] V. V. Galassi and N. Wilke, "On the coupling between mechanical properties and electrostatics in biological membranes," *Membranes*, vol. 11, no. 7, p. 478, 2021.

[47] E. Niesner, "Subsurface resistivity changes and triggering influences detected by continuous geoelectric monitoring," *The Leading Edge*, vol. 29, no. 8, pp. 952–955, 2010.

[48] F. Owusu-Nimo and F. K. Boadu, "Evaluating effective stress conditions in soils using non-invasive electrical measurements–laboratory studies," *Journal of Applied Geophysics*, vol. 174, p. 103 961, 2020.

[49] L. Jouniaux and F. Zyserman, "A review on electrokinetically induced seismo-electrics, electro-seismics, and seismo-magnetics for earth sciences," *Solid Earth*, vol. 7, no. 1, pp. 249–284, 2016.

[50] N. M. Neishtadt, L. V. Eppelbaum, and A. G. Levitski, "Application of piezoelectric and seismoelectrokinetic phenomena in exploration geophysics: Review of russian and israeli experiences," *Geophysics*, vol. 71, no. 2, B41–B53, 2006.

[51] H. H. Pan and M.-W. Huang, "Piezoelectric cement sensor-based electromechanical impedance technique for the strength monitoring of cement mortar," *Construction and Building Materials*, vol. 254, p. 119 307, 2020.

[52] D.-Y. Yoo, I. You, and S.-J. Lee, "Electrical and piezoresistive sensing capacities of cement paste with multi-walled carbon nanotubes," *Archives of Civil and Mechanical Engineering*, vol. 18, pp. 371–384, 2018.

[53] F. Panozzo, M. Zappalorto, L. Maragoni, S. K. Nothdurfter, A. Rullo, and M. Quaresimin, "Modelling the electrical resistance change in a multidirectional laminate with a delamination," *Composites Science and Technology*, vol. 162, pp. 225–234, 2018.

[54] P. Scholle and M. Sinapius, "A review on the usage of continuous carbon fibers for piezoresistive self strain sensing fiber reinforced plastics," *Journal of Composites Science*, vol. 5, no. 4, p. 96, 2021.

[55] E. T. Thostenson and T.-W. Chou, "Carbon nanotube networks: Sensing of distributed strain and damage for life prediction and self healing," *Advanced Materials*, vol. 18, no. 21, pp. 2837–2841, 2006.

[56] E. T. Thostenson and T.-W. Chou, "Real-time in situ sensing of damage evolution in advanced fiber composites using carbon nanotube networks," *Nanotechnology*, vol. 19, no. 21, p. 215 713, 2008.

[57] I. Kang, M. J. Schulz, J. H. Kim, V. Shanov, and D. Shi, "A carbon nanotube strain sensor for structural health monitoring," *Smart materials and structures*, vol. 15, no. 3, p. 737, 2006.

[58] C. Li, E. T. Thostenson, and T.-W. Chou, "Dominant role of tunneling resistance in the electrical conductivity of carbon nanotube–based composites," *Applied Physics Letters*, vol. 91, no. 22, p. 223 114, 2007.

[59] G. Koo and T. Tallman, "Higher-order resistivity-strain relations for self-sensing nanocomposites subject to general deformations," *Composites Part B: Engineering*, vol. 190, p. 107 907, 2020.

[60] T. N. Tallman, S. Gungor, K. W. Wang, and C. E. Bakis, "Damage detection and conductivity evolution in carbon nanofiber epoxy via electrical impedance tomography," *Smart Materials and Structures*, vol. 23, no. 4, p. 045 034, Mar. 2014. DOI: 10.1088/0964-1726/23/4/045034. [Online]. Available: https://dx.doi.org/10.1088/0964-1726/23/4/045034.

[61] T. N. Tallman and K. W. Wang, "An inverse methodology for calculating strains from conductivity changes in piezoresistive nanocomposites," *Smart Materials and Structures*, vol. 25, no. 11, p. 115 046, Oct. 2016. DOI: 10.1088/0964-1726/25/11/115046. [Online]. Available: https://dx.doi.org/10.1088/0964-1726/25/11/115046.

[62] F. Avilés, A. I. Oliva-Avilés, and M. Cen-Puc, "Piezoresistivity, strain, and damage self-sensing of polymer composites filled with carbon nanostructures," *Advanced Engineering Materials*, vol. 20, no. 7, p. 1 701 159, 2018.

[63] J. G. Simmons, "Generalized formula for the electric tunnel effect between similar electrodes separated by a thin insulating film," *Journal of applied physics*, vol. 34, no. 6, pp. 1793–1803, 1963.

[64] N. Hu, Y. Karube, C. Yan, Z. Masuda, and H. Fukunaga, "Tunneling effect in a polymer/carbon nanotube nanocomposite strain sensor," *Acta materialia*, vol. 56, no. 13, pp. 2929–2936, 2008.

[65] T. Tallman and K. W. Wang, "An arbitrary strains carbon nanotube composite piezoresistivity model for finite element integration," *Applied Physics Letters*, vol. 102, no. 1, Jan. 2013, 011909, ISSN: 0003-6951. DOI: 10.1063/1.4774294. eprint: https://pubs.aip.org/aip/apl/article-pdf/doi/10.1063/1.4774294/14264956/011909_1_online.pdf. [Online]. Available: https://doi.org/10.1063/1.4774294.

[66] T. N. Tallman and D. J. Smyl, "Structural health and condition monitoring via electrical impedance tomography in self-sensing materials: A review," *Smart Materials and Structures*, vol. 29, no. 12, p. 123 001, 2020.

[67] R. Guan, F. Zou, D. Li, W. Liu, and C. Wu, "Understanding the sensitivity of thin-film graphene/polymer nanocomposite strain sensors to ultrasonic waves: Analytical and experimental analysis," *Composites Science and Technology*, vol. 216, p. 109 079, 2021.

[68] P. Zhou, Y. Liao, Y. Li, *et al.*, "An inkjet-printed, flexible, ultra-broadband nanocomposite film sensor for in-situ acquisition of high-frequency dynamic strains," *Composites Part A: Applied Science and Manufacturing*, vol. 125, p. 105 554, 2019.

[69] Z. Zeng, M. Liu, H. Xu, *et al.*, "Ultra-broadband frequency responsive sensor based on lightweight and flexible carbon nanostructured polymeric nanocomposites," *Carbon*, vol. 121, pp. 490–501, 2017.

[70] P. Zhou, W. Cao, Y. Liao, *et al.*, "Temperature effect on all-inkjet-printed nanocomposite piezoresistive sensors for ultrasonics-based health monitoring," *Composites Science and Technology*, vol. 197, p. 108 273, 2020.

[71] W. Cao, P. Zhou, Y. Liao, *et al.*, "A spray-on, nanocomposite-based sensor network for in-situ active structural health monitoring," *Sensors*, vol. 19, no. 9, p. 2077, 2019.

[72] Y. Su, J. Yang, Y. Liao, *et al.*, "An implantable, compatible and networkable nanocomposite piezoresistive sensor for in situ acquisition of dynamic responses of cfrps," *Composites Science and Technology*, vol. 208, p. 108 747, 2021.

[73] Y. Su, L. Xu, P. Zhou, *et al.*, "In situ cure monitoring and in-service impact localization of frps using pre-implanted nanocomposite sensors," *Composites Part A: Applied Science and Manufacturing*, vol. 154, p. 106 799, 2022.

[74] Y. Li, K. Wang, Q. Wang, *et al.*, "Acousto-ultrasonics-based health monitoring for nano-engineered composites using a dispersive graphene-networked sensing system," *Structural Health Monitoring*, vol. 20, no. 1, pp. 240–254, 2021.

[75] F. Ubertini, S. Laflamme, H. Ceylan, *et al.*, "Novel nanocomposite technologies for dynamic monitoring of structures: A comparison between cement-based embeddable and soft elastomeric surface sensors," *Smart Materials and Structures*, vol. 23, no. 4, p. 045 023, 2014.

[76] D. García, I. Trendafilova, and D. J. Inman, "A study on the vibration-based self-monitoring capabilities of nano-enriched composite laminated beams," *Smart Materials and Structures*, vol. 25, no. 4, p. 045 011, 2016.

[77] Y. Li, Y. Liao, and Z. Su, "Graphene-functionalized polymer composites for self-sensing of ultrasonic waves: An initiative towards "sensor-free" structural health monitoring," *Composites Science and Technology*, vol. 168, pp. 203–213, 2018.

[78] M. Lowe, "Disperse: Guided wave dispersion curve calculation," *Imperial College NDT lab, nd*, 2022.

[79] T.-C. Hou, K. J. Loh, and J. P. Lynch, "Spatial conductivity mapping of carbon nanotube composite thin films by electrical impedance tomography for sensing applications," *Nanotechnology*, vol. 18, no. 31, p. 315 501, 2007.

[80] L. Chen, H. Hassan, T. N. Tallman, S.-S. Huang, and D. Smyl, "Predicting strain and stress fields in self-sensing nanocomposites using deep learned electrical tomography," *Smart Materials and Structures*, vol. 31, no. 4, p. 045 024, 2022.

[81] S. Quqa, L. Landi, and K. J. Loh, "Crack identification using electrical impedance tomography and transfer learning," *Computer-Aided Civil and Infrastructure Engineering*, 2023.

[82] M. Soleimani, "Electrical impedance tomography imaging using a priori ultrasound data," *Biomedical engineering online*, vol. 5, pp. 1–8, 2006.

[83] E. K. Murphy, J. Skinner, M. Martucci, S. B. Rutkove, and R. J. Halter, "Toward electrical impedance tomography coupled ultrasound imaging for assessing muscle health," *IEEE transactions on medical imaging*, vol. 38, no. 6, pp. 1409–1419, 2018.

[84] M. Wang, A. Zarafshani, P. Samant, J. Merrill, D. Li, and L. Xiang, "Feasibility of electroacoustic tomography: A simulation study," *IEEE transactions on ultrasonics, ferroelectrics, and frequency control*, vol. 67, no. 5, pp. 889–897, 2019.

[85] C. Siart, M. Forbriger, E. Nowaczinski, S. Hecht, and B. Höfle, "Fusion of multiresolution surface (terrestrial laser scanning) and subsurface geodata (ert, srt) for karst landform investigation and geomorphometric quantification," *Earth Surface Processes and Landforms*, vol. 38, no. 10, pp. 1135–1147, 2013.

[86] M. Hata, S. Takakura, N. Matsushima, T. Hashimoto, and M. Utsugi, "Crustal magma pathway beneath aso caldera inferred from three-dimensional electrical resistivity structure," *Geophysical Research Letters*, vol. 43, no. 20, pp. 10–720, 2016.

[87] M. Hata, N. Matsushima, S. Takakura, M. Utsugi, T. Hashimoto, and M. Uyeshima, "Three-dimensional electrical resistivity modeling to elucidate the crustal magma supply system beneath aso caldera, japan," *Journal of Geophysical Research: Solid Earth*, vol. 123, no. 8, pp. 6334–6346, 2018.

[88] H. Hassan and T. N. Tallman, "A comparison of metaheuristic algorithms for solving the piezoresistive inverse problem in self-sensing materials," *IEEE Sensors Journal*, vol. 21, no. 1, pp. 659–666, 2020.

[89] L. Homa, M. Sannamani, A. J. Thomas, T. N. Tallman, and J. Wertz, "Enhanced damage imaging in three-dimensional composite structures via electrical impedance tomography with mixed and level set regularization," *NDT & E International*, vol. 137, p. 102 830, 2023.

[90] S. Rana, R. Alagirusamy, and M. Joshi, "A review on carbon epoxy nanocomposites," *Journal of Reinforced Plastics and Composites*, vol. 28, no. 4, pp. 461–487, 2009. DOI: 10.1177/0731684407085417. eprint: https://doi.org/10.1177/0731684407085417. [Online]. Available: https://doi.org/10.1177/0731684407085417.

[91] E. A. Zaragoza-Contreras, C. A. Hernández-Escobar, A. Navarrete-Fontes, and S. G. Flores-Gallardo, "Synthesis of carbon black/polystyrene conductive nanocomposite. pickering emulsion effect characterized by tem," *Micron*, vol. 42, no. 3, pp. 263–270, 2011, ISSN: 0968-4328. DOI: https://doi.org/10.1016/j.micron.2010.10.005. [Online]. Available: https://www.sciencedirect.com/science/article/pii/S0968432810002556.

[92] K.-t. Lau, M. Lu, C.-k. Lam, H.-y. Cheung, F.-L. Sheng, and H.-L. Li, "Thermal and mechanical properties of single-walled carbon nanotube bundle-reinforced epoxy nanocomposites: The role of solvent for nanotube dispersion," *Composites science and technology*, vol. 65, no. 5, pp. 719–725, 2005.

[93] M. Šupová, G. S. Martynková, and K. Barabaszová, "Effect of nanofillers dispersion in polymer matrices: A review," *Science of advanced materials*, vol. 3, no. 1, pp. 1–25, 2011.

[94] L. Vaisman, G. Marom, and H. D. Wagner, "Dispersions of surface-modified carbon nanotubes in water-soluble and water-insoluble polymers," *Advanced Functional Materials*, vol. 16, no. 3, pp. 357–363, 2006. DOI: https://doi.org/10.1002/adfm.200500142. eprint: https://onlinelibrary.wiley.com/doi/pdf/10.1002/adfm.200500142. [Online]. Available: https://onlinelibrary.wiley.com/doi/abs/10.1002/adfm.200500142.

[95] Y. Geng, M. Y. Liu, J. Li, X. M. Shi, and J. K. Kim, "Effects of surfactant treatment on mechanical and electrical properties of cnt/epoxy nanocomposites," *Composites Part A: Applied Science and Manufacturing*, vol. 39, no. 12, pp. 1876–1883, 2008, ISSN: 1359-835X. DOI: https://doi.org/10.1016/j.compositesa.2008.09.009. [Online]. Available: https://www.sciencedirect.com/science/article/pii/S1359835X08002406.

[96] H. Kolsky, "An investigation of the mechanical properties of materials at very high rates of loading," *Proceedings of the Physical Society. Section B*, vol. 62, no. 11, p. 676, Nov. 1949. DOI: 10.1088/0370-1301/62/11/302. [Online]. Available: https://dx.doi.org/10.1088/0370-1301/62/11/302.

[97] M. M. Al-Mousawi, S. R. Reid, and W. F. Deans, "The use of the split hopkinson pressure bar techniques in high strain rate materials testing," *Proceedings of the Institution of Mechanical Engineers, Part C: Journal of Mechanical Engineering Science*, vol. 211, no. 4, pp. 273–292, 1997. DOI: 10.1243/0954406971522042. eprint: https://doi.org/10.1243/0954406971522042. [Online]. Available: https://doi.org/10.1243/0954406971522042.

[98] W. Chen and B. Song, *Split Hopkinson (Kolsky) Bar, Design, Testing and Applications*, eng, 1st ed. New York: Springer, 2010. DOI: https://doi.org/10.1007/978-1-4419-7982-7.

[99] H. Kolsky, *Stress waves in solids*. Courier Corporation, 1963, vol. 1098.

[100] D. J. Frew, M. J. Forrestal, and W. Chen, "Pulse shaping techniques for testing brittle materials with a split hopkinson pressure bar," *Experimental mechanics*, vol. 42, pp. 93–106, 2002.

[101] X. Ji, H. Li, D. Hui, K.-T. Hsiao, J. Ou, and A. K. Lau, "I–v characteristics and electro-mechanical response of different carbon black/epoxy composites," *Composites Part B: Engineering*, vol. 41, no. 1, pp. 25–32, 2010, ISSN: 1359-8368. DOI: https://doi.org/10.1016/j.compositesb.2009.05.001. [Online]. Available: https://www.sciencedirect.com/science/article/pii/S1359836809000936.

[102] A. J. Paleo, F. W. J. van Hattum, J. Pereira, *et al.*, "The piezoresistive effect in polypropylene—carbon nanofibre composites obtained by shear extrusion," *Smart Materials and Structures*, vol. 19, no. 6, p. 065 013, May 2010. DOI: 10.1088/0964-1726/19/6/065013. [Online]. Available: https://dx.doi.org/10.1088/0964-1726/19/6/065013.

[103] A. Alizadeh Sahraei, M. Ayati, M. Baniassadi, D. Rodrigue, M. Baghani, and Y. Abdi, "AC and DC electrical behavior of MWCNT/epoxy nanocomposite near percolation threshold: Equivalent circuits and percolation limits," *Journal of Applied Physics*, vol. 123, no. 10, Mar. 2018, 105109, ISSN: 0021-8979. DOI: 10.1063/1.5019347. eprint: https://pubs.aip.org/aip/jap/article-pdf/doi/10.1063/1.5019347/15209575/105109_1_online.pdf. [Online]. Available: https://doi.org/10.1063/1.5019347.

[104] J. C. Kennedy and W. E. Woodmansee, "Electronic signal processing techniques. phase 2. nondestructive testing," BOEING AEROSPACE CO SEATTLE WA, Tech. Rep., 1970.

[105] T. Thomas, "Ensemble averaging filter for noise reduction," *International Journal of Advanced Research in Computer and Communication Engineering*, vol. 5, no. 8, Aug. 2016. DOI: 10.17148/IJARCCE.2016.5852.

[106] T. Takeda, Y. Shindo, Y. Kuronuma, and F. Narita, "Modeling and characterization of the electrical conductivity of carbon nanotube-based polymer composites," *Polymer*, vol. 52, no. 17, pp. 3852–3856, 2011, ISSN: 0032-3861. DOI: https://doi.org/10.1016/j.polymer.2011.06.046. [Online]. Available: https://www.sciencedirect.com/science/article/pii/S0032386111005350.

[107] A. Todoroki, Y. Samejima, Y. Hirano, and R. Matsuzaki, "Piezoresistivity of unidirectional carbon/epoxy composites for multiaxial loading," *Composites Science and Technology*, vol. 69, no. 11, pp. 1841–1846, 2009, Experimental Techniques and Design in Composite Materials (ETDCM8) with Regular Papers, ISSN: 0266-3538. DOI: https://doi.org/10.1016/j.compscitech.2009.03.023. [Online]. Available: https://www.sciencedirect.com/science/article/pii/S026635380900133X.

[108] H. A. K. Toprakci, S. K. Kalanadhabhatla, R. J. Spontak, and T. K. Ghosh, "Polymer nanocomposites containing carbon nanofibers as soft printable sensors exhibiting strain-reversible piezoresistivity," *Advanced Functional Materials*, vol. 23, no. 44, pp. 5536–5542, 2013. DOI: https://doi.org/10.1002/adfm.201300034. eprint: https://onlinelibrary.wiley.com/doi/pdf/10.1002/adfm.201300034. [Online]. Available: https://onlinelibrary.wiley.com/doi/abs/10.1002/adfm.201300034.

[109] X. Liu, G. Su, Q. Guo, *et al.*, "Hierarchically structured self-healing sensors with tunable positive/negative piezoresistivity," *Advanced Functional Materials*, vol. 28, no. 15, p. 1 706 658, 2018. DOI: https://doi.org/10.1002/adfm.201706658. eprint: https://onlinelibrary.wiley.com/doi/pdf/10.1002/adfm.201706658. [Online]. Available: https://onlinelibrary.wiley.com/doi/abs/10.1002/adfm.201706658.

[110] N. Hu, Y. Karube, M. Arai, *et al.*, "Investigation on sensitivity of a polymer/carbon nanotube composite strain sensor," *Carbon*, vol. 48, no. 3, pp. 680–687, 2010, ISSN: 0008-6223. DOI: https://doi.org/10.1016/j.carbon.2009.10.012. [Online]. Available: https://www.sciencedirect.com/science/article/pii/S0008622309006824.

[111] G. Yin, N. Hu, Y. Karube, Y. Liu, Y. Li, and H. Fukunaga, "A carbon nanotube/polymer strain sensor with linear and anti-symmetric piezoresistivity," *Journal of Composite Materials*, vol. 45, no. 12, pp. 1315–1323, 2011. DOI: 10.1177/0021998310393296. eprint: https://doi.org/10.1177/0021998310393296. [Online]. Available: https://doi.org/10.1177/0021998310393296.

[112] G. Canavese, S. Stassi, C. Fallauto, *et al.*, "Piezoresistive flexible composite for robotic tactile applications," *Sensors and Actuators A: Physical*, vol. 208, pp. 1–9, 2014, ISSN: 0924-4247. DOI: https://doi.org/10.1016/j.sna.2013.11.018. [Online]. Available: https://www.sciencedirect.com/science/article/pii/S0924424713005724.

[113] Z. Wang, S. Wang, J. Zeng, *et al.*, "High sensitivity, wearable, piezoresistive pressure sensors based on irregular microhump structures and its applications in body motion sensing," *Small*, vol. 12, no. 28, pp. 3827–3836, 2016. DOI: https://doi.org/10.1002/smll.201601419. eprint: https://onlinelibrary.wiley.com/doi/pdf/10.1002/smll.201601419. [Online]. Available: https://onlinelibrary.wiley.com/doi/abs/10.1002/smll.201601419.

[114] A. S. Lim, Q. An, T.-W. Chou, and E. T. Thostenson, "Mechanical and electrical response of carbon nanotube-based fabric composites to hopkinson bar loading," *Composites Science and Technology*, vol. 71, no. 5, pp. 616–621, 2011, ISSN: 0266-3538. DOI: https://doi.org/10.1016/j.compscitech.2010.12.025. [Online]. Available: https://www.sciencedirect.com/science/article/pii/S0266353810004938.

[115] W. Al-Lafi, J. Jin, S. Xu, and M. Song, "Performance of mwcnt/hdpe nanocomposites at high strain rates," *Macromolecular Materials and Engineering*, vol. 295, no. 6, pp. 519–522, 2010. DOI: https://doi.org/10.1002/mame.200900374. eprint: https://onlinelibrary.wiley.com/doi/pdf/10.1002/mame.200900374. [Online]. Available: https://onlinelibrary.wiley.com/doi/abs/10.1002/mame.200900374.

[116] Y. Tian, H. Zhang, J. Zhao, *et al.*, "High strain rate compression of epoxy based nanocomposites," *Composites Part A: Applied Science and Manufacturing*, vol. 90, pp. 62–70, 2016, ISSN: 1359-835X. DOI: https://doi.org/10.1016/j.compositesa.2016.06.008. [Online]. Available: https://www.sciencedirect.com/science/article/pii/S1359835X16301865.

[117] J. Hernandez, N. Kedir, B. H. Lim, W. Chen, and T. Tallman, "An experimental study on the piezoresistive and mechanical behavior of carbon nanocomposites subject to high-rate elastic loading," *Composites Science and Technology*, vol. 198, p. 108 285, 2020, ISSN: 0266-3538. DOI: https://doi.org/10.1016/j.compscitech.2020.108285. [Online]. Available: https://www.sciencedirect.com/science/article/pii/S0266353820301287.

[118] H. Hassan and T. N. Tallman, "Failure prediction in self-sensing nanocomposites via genetic algorithm-enabled piezoresistive inversion," *Structural Health Monitoring*, vol. 19, no. 3, pp. 765–780, 2020.

[119] L. Chen, H. Hassan, T. N. Tallman, S.-S. Huang, and D. Smyl, "Predicting strain and stress fields in self-sensing nanocomposites using deep learned electrical tomography," *Smart Materials and Structures*, vol. 31, no. 4, p. 045 024, 2022.

[120] A. U. Manual, "Abaqus user manual," *Abacus*, 2020.

[121] M. Gresil and V. Giurgiutiu, "Prediction of attenuated guided waves propagation in carbon fiber composites using rayleigh damping model," *Journal of Intelligent Material Systems and Structures*, vol. 26, no. 16, pp. 2151–2169, 2015.

[122] A. Sladen, D. Rivet, J. P. Ampuero, *et al.*, "Distributed sensing of earthquakes and ocean-solid earth interactions on seafloor telecom cables," *Nature communications*, vol. 10, no. 1, p. 5777, 2019.

[123] A. D. Booth, P. Christoffersen, C. Schoonman, *et al.*, "Distributed acoustic sensing of seismic properties in a borehole drilled on a fast-flowing greenlandic outlet glacier," *Geophysical Research Letters*, vol. 47, no. 13, e2020GL088148, 2020.

[124] Y. Al-Handarish, O. M. Omisore, T. Igbe, *et al.*, "A survey of tactile-sensing systems and their applications in biomedical engineering," *Advances in Materials Science and Engineering*, vol. 2020, 2020.

[125] Y. Matsumoto, A. Katsumura, and N. Miki, "Pressure-controlled ultrasound probe for reliable imaging in breast cancer diagnosis," eng, *Japanese Journal of Applied Physics*, vol. 61, no. SD, SD1035–, 2022, ISSN: 0021-4922.

[126] N. Prakash and G. D. Seidel, "Effects of microscale damage evolution on piezoresistive sensing in nanocomposite bonded explosives under dynamic loading via electromechanical peridynamics," *Modelling and Simulation in Materials Science and Engineering*, vol. 26, no. 1, p. 015 003, 2017.

[127] E. C. Sengezer and G. D. Seidel, "Structural health monitoring of nanocomposite bonded energetic materials through piezoresistive response," *Aiaa Journal*, vol. 56, no. 3, pp. 1225–1238, 2018.

[128] K. K. Talamadupula, S. Povolny, N. Prakash, and G. D. Seidel, "Piezoresistive detection of simulated hotspots and the effects of low velocity impact at the mesoscale in nanocomposite bonded energetic materials via multiphysics peridynamics modeling," *Computational Materials Science*, vol. 188, p. 110 211, 2021.

[129] J. R. Gilbert, C. Moler, and R. Schreiber, "Sparse matrices in matlab: Design and implementation," *SIAM Journal on Matrix Analysis and Applications*, vol. 13, no. 1, pp. 333–356, 1992. DOI: 10.1137/0613024.

A. Finite Element Method Preliminaries

A.1 Introduction

The development of approximate methods for solving partial differential equations through numerical means has received concerted attention and focus from mathematicians for decades, if not centuries. Their efforts have considerably impacted adjacent fields such as physics, chemistry, and engineering. Namely, the finite element method has facilitated the analysis of complex geometries through discretizing a continuum, element-wise compatibility conditions, and enforcing boundary/initial conditions. This appendix does not aim to provide a comprehensive overview of the finite element method because plenty of literature resources accomplish that goal. However, this appendix aims to diligently treat the finite element formulation that is reflective of the work contained in this dissertation. This is because while the finite element method was a crucial component of this research, it is not necessarily its focus, nor were advancements sought in the field of solving partial differential equations through numerical means.

A.2 From Strong-Form to Weak-Form: An FEM Formulation of the Steady-State Parabolic Differential Equation

Consider a second-order parabolic partial differential equation for steady-state electrical diffusion in n-dimensions. Let the domain be defined using real numbers in space, $\Omega \subset \mathbb{R}^n$, with a spatially varying conductivity tensor that maps onto the domain, $\sigma(x) : \Omega \to \mathbb{R}^{n \times n}$. This domain has a smooth boundary, $\partial \Omega$, consisting of the union of two disjoint sets Γ_E and Γ_N (i.e., $\partial \Omega = \Gamma_E \cup \Gamma_N$). A smooth boundary also provides well-defined unit normal vectors and ensures continuous basis functions. Furthermore, within the complete electrode model framework, Γ_E refers to the boundary electrodes, whereas Γ_N denotes the domain boundary excluding the electrodes. The rules of Einstein index notation are strictly enforced unless stated otherwise. Consider the strong form expression for the second-order parabolic partial differential equation for steady-state electrical diffusion,

$$-\frac{\partial j_{\mathrm{i}}}{\partial x_{\mathrm{i}}} = \frac{\partial}{\partial x_{\mathrm{i}}} \sigma_{\mathrm{ij}} \frac{\partial u}{\partial x_{\mathrm{j}}}\bigg|_{\Omega} = f \tag{A.1}$$

Subject to the following boundary conditions:

$$\sum_{l=1}^{L} \int_{E_l} \sigma_{\mathrm{ij}} \frac{\partial u}{\partial x_{\mathrm{i}}} n_{\mathrm{j}} dS_l\bigg|_{\Gamma_E} = \sum_{l=1}^{L} I_l = 0 \tag{A.2}$$

$$\sigma_{\mathrm{ij}} \frac{\partial u}{\partial x_{\mathrm{i}}} n_{\mathrm{j}}\bigg|_{\Gamma_N} = 0 \tag{A.3}$$

$$\sigma_{\mathrm{ij}} \frac{\partial u}{\partial x_{\mathrm{i}}} n_{\mathrm{j}}\bigg|_{\Gamma_E} = \frac{1}{z_l}(V_l - u) \tag{A.4}$$

Where f denotes an internal current source, n_j is the unit normal vector, E_l is the curve or surface of the l'th electrode, I_l is the current amplitude through the l'th electrode, V_l is the voltage of the l'th electrode, and L is the total number of electrodes. The parameters, u, j_i, and σ_{ij}, are the domain potential, current density vector, and symmetric anisotropic conductivity tensor of the PDE, respectively. Equation (A.2) and Equation (A.3) denote the conservation of charge is enforced through domain boundaries. In other words, the flow of current through the driving and measurement electrodes is conserved, and the boundaries not involved in the current injection or measurement scheme are perfectly insulating. Equation (A.4) represents the domain-electrode CEM interface condition due to contact impedance.
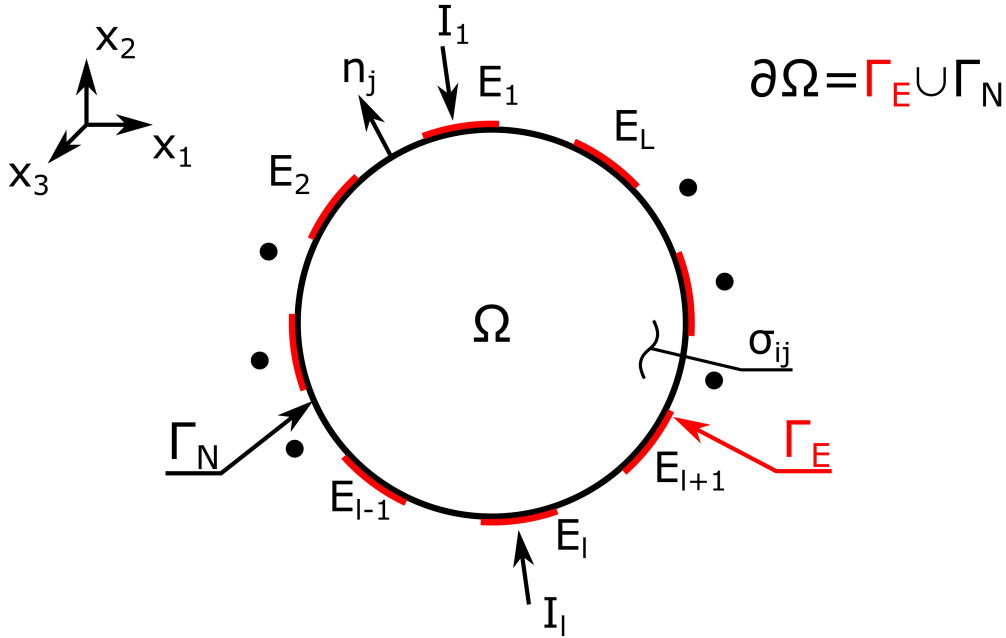
Figure A.1. Suppose a domain, Ω, in three dimensions, is examined to develop the FEM formulation of the steady-state parabolic differential equation. Electrodes (shown in red) are attached to the domain boundary, $\partial\Omega$, where current can be injected into the domain. It is assumed that the voltage across the electrode, V_l, is constant.

The infinite-dimensional strong form implies the existence of the finite-dimensional weak form. The weak form is formed by leveraging a trial function, ψ, that satisfies specified Dirichlet boundary conditions such that the exact solution, u, is approximated throughout the domain. This trial function represents the unknown behavior or variation of the found solution. By introducing the trial function, the strong form expression in Equation (A.1) can be rewritten as,

$$\int_\Omega \psi \frac{\partial}{\partial x_i} \sigma_{ij} \frac{\partial u}{\partial x_j} d\Omega = \int_\Omega \psi f d\Omega \tag{A.5}$$

The trial function can be incorporated by leveraging the product rule (Equation (A.6)) and divergence theorem/Green's second identity (Equation (A.7)).

$$\int_\Omega \left(\frac{\partial}{\partial x_\mathrm{i}} \psi \sigma_\mathrm{ij} \frac{\partial u}{\partial x_\mathrm{j}} - \frac{\partial \psi}{\partial x_\mathrm{i}} \sigma_\mathrm{ij} \frac{\partial u}{\partial x_\mathrm{j}} \right) d\Omega = \int_\Omega \psi f d\Omega \tag{A.6}$$

$$\int_{\partial\Omega} \psi \sigma_\mathrm{ij} \frac{\partial u}{\partial x_\mathrm{i}} n_\mathrm{j} dS - \int_\Omega \frac{\partial \psi}{\partial x_\mathrm{i}} \sigma_\mathrm{ij} \frac{\partial u}{\partial x_\mathrm{j}} d\Omega = \int_\Omega \psi f d\Omega \tag{A.7}$$

Rearranging the expression,

$$\int_\Omega \frac{\partial \psi}{\partial x_\mathrm{i}} \sigma_\mathrm{ij} \frac{\partial u}{\partial x_\mathrm{j}} d\Omega = \int_{\partial\Omega} \psi \sigma_\mathrm{ij} \frac{\partial u}{\partial x_\mathrm{i}} n_\mathrm{j} dS - \int_\Omega \psi f d\Omega \tag{A.8}$$

Recall that the domain boundary is the union of a disjoint set. This allows for the surface integral on the domain boundary to be split into two integrals that belong to Γ_E and Γ_N.

$$\int_\Omega \frac{\partial \psi}{\partial x_\mathrm{i}} \sigma_\mathrm{ij} \frac{\partial u}{\partial x_\mathrm{j}} d\Omega = \overbrace{\int_{\Gamma_N} \psi \sigma_\mathrm{ij} \frac{\partial u}{\partial x_\mathrm{i}} n_\mathrm{j} dS}^{0} + \int_{\Gamma_E} \psi \sigma_\mathrm{ij} \frac{\partial u}{\partial x_\mathrm{i}} n_\mathrm{j} dS - \int_\Omega \psi f d\Omega \tag{A.9}$$

The first surface integral belonging to Γ_N is set to zero by imposing the boundary condition of the perfectly electrically insulating surfaces, Equation (A.3). The second surface integral of Γ_E is then prescribed with the contact impedance condition between the domain and electrodes for the CEM model, Equation (A.4). By assuming that internal current sources are absent (e.g., $f = 0$), the weak form is shown to be derived from the strong-form.

$$\int_\Omega \frac{\partial \psi}{\partial x_\mathrm{i}} \sigma_\mathrm{ij} \frac{\partial u}{\partial x_\mathrm{j}} d\Omega = \sum_{l=1}^{L} \int_{\mathrm{E}_l} \frac{1}{z_l} (V_l - u) \psi dS \tag{A.10}$$

In order to employ the weak-form for FEM, the domain must be treated with an element-wise discretization. The domain is discretized into element sub-domains $\Omega_\mathrm{e} \subset \Omega$ and the elements represent a unique region of space without intersecting other elements $\Omega_{\mathrm{e}_\mathrm{i}} \cap \Omega_{\mathrm{e}_\mathrm{j}} = \emptyset$ (when $\mathrm{i} \neq \mathrm{j}$). Individual element sub-domains are called finite elements. These finite elements can be assembled to represent the entire domain and its boundary $\Omega = \cup_\mathrm{e} \Omega_\mathrm{e}$. Through the summation operator $\sum_\mathrm{e}(\cdot)$, the weak-form for the domain can be constructed by means of an assembly of e-number of finite elements.

$$\sum_\mathrm{e} \int_{\Omega_\mathrm{e}} \frac{\partial \psi_\mathrm{e}}{\partial x_\mathrm{i}} \sigma_\mathrm{ij} \frac{\partial u_\mathrm{e}}{\partial x_\mathrm{j}} d\Omega_\mathrm{e} = \sum_\mathrm{e} \sum_{l=1}^{L} \int_{E_l\,\mathrm{e}} \frac{1}{z_l} (V_l - u_\mathrm{e}) \psi_\mathrm{e} dS_\mathrm{e} \tag{A.11}$$

A set of nodes defines each element as vertices and a basis function, w, that interpolates the behavior of the potential solution, u, and its variation, ψ, within its interior.

$$u_\mathrm{e} = \sum_{A=1}^{N} w^A d_\mathrm{e}^A \tag{A.12}$$

$$\psi_e = \sum_{A=1}^{N} w^A c_e^A \tag{A.13}$$

Where A refers to the A'th local node number of the e'th element, and w^A denotes the A'th basis function. Quantities d_e^A and c_e^A represent the potential solution and variation at the A'th node of the e'th element, respectively. The expressions for u_e and ψ_e are substituted into the left-hand side of the finite-element expression of the weak-form in Equation (A.11). This provides the means to approach the construction of the <u>element matrix weak-form</u> for FEM using interpolation/basis functions; the assembly of the element matrices into the global matrix is elaborated in Section: **A.4 Matrix Assembly**, including an illustrated example. Henceforth, we drop the summation operator, $\sum_e(\cdot)$, to narrow the discussion to a representative finite element, Ω_e.

$$\int_{\Omega_e} \frac{\partial \psi_e}{\partial x_i} \sigma_{ij} \frac{\partial u_e}{\partial x_j} d\Omega_e = \sum_{A=1}^{N} \sum_{B=1}^{N} c_e^A \int_{\Omega_e} \frac{\partial w^A}{\partial x_i} \sigma_{ij} \frac{\partial w^B}{\partial x_j} d\Omega_e d_e^B \tag{A.14}$$

The quantities c_e^A and d_e^B are pulled out of the integration over the element domain, $\int(\cdot)d\Omega_e$, considering they are constant values. Next, the basis functions must be defined to compute their gradients. However, defining the basis functions with respect to the nodal coordinates in the global coordinate system (i.e., $w^A = w^A(x)$) will result in a computationally expensive process when the integral is evaluated. To circumvent this issue, a linear mapping between the element domain and the isoparametric domain, $\zeta : \Omega_e \leftrightarrow \Omega_\zeta$, can be employed to conduct the integration in the more practical coordinate system. Additionally, the basis functions (i.e., $w^A = w^A(\zeta)$) can be employed to describe the interior of an element, $x_i^e(\zeta)$, as a continuous function of the isoparametric variable using the nodal coordinates in the global coordinate system. Put differently, the basis functions and nodal coordinates are used to interpolate spatial position within an element.

$$x_i^e(\zeta) = \sum_{A=1}^{N} w^A(\zeta) x_{i\,A}^e \tag{A.15}$$

Where $x_{i\,A}^e$ is the i'th coordinate component of the A'th node in the e'th element. The basis function is in terms of the isoparametric variable, ζ, and is defined within the isoparametric domain with the bounds of $[0, 1]$ for triangular/tetrahedral elements and $[-1, 1]$ for square/hexahedral elements. Leveraging the chain rule for differentiation, the gradient of the basis functions is expressed as the product of two partial derivatives in terms of ζ and x.

$$\frac{\partial w^A}{\partial x_i} = \frac{\partial w^A}{\partial \zeta_j} \frac{\partial \zeta_j}{\partial x_i} \tag{A.16}$$

The partial derivatives of the basis functions, $\frac{\partial w}{\partial x}$, in the finite element weak-form in Equation (A.14) can now be expanded. However, shifting the element integrated from the original domain to the isoparametric domain requires the transformation $d\Omega_e = \det|J|d\Omega_\zeta$ and a change in integration limits. The Jacobian, $J_{ij} = \frac{\partial x_i}{\partial \zeta_j}$, physically represents a linear and

exact mapping between the element domain and the bounded isoparametric domain. The transformation produces an expression that can be computed in the isoparametric domain,

$$\int_{\Omega_e} \frac{\partial \psi_e}{\partial x_i} \sigma_{ij} \frac{\partial u_e}{\partial x_j} d\Omega_e = \sum_{A=1}^{N} \sum_{B=1}^{N} c_e^A \int_{\Omega_{e\zeta}} \frac{\partial w^A}{\partial \zeta_k} \frac{\partial \zeta_k}{\partial x_i} \sigma_{ij} \frac{\partial w^B}{\partial \zeta_l} \frac{\partial \zeta_l}{\partial x_j} \det \overbrace{\left| \frac{\partial x_m}{\partial \zeta_n} \right|}^{J_{mn}} d\Omega_{e\zeta} d_e^B \qquad (A.17)$$

Gaussian Quadrature is an effective and efficient computational tool to directly evaluate the finite element weak-form integral, especially for a finely discretized domain or when using higher-order basis functions. In the isoparametric domain, Gaussian Quadrature evaluates the integral of a function, $f(\zeta_i)$, using a number of integration points, n_{int_i}, weights, ω_{l_i}, and function evaluations at specific points, $\zeta_i^{l_i}$. The expression shown in Equation (A.18) presents the general multivariate form of Gaussian Quadrature.
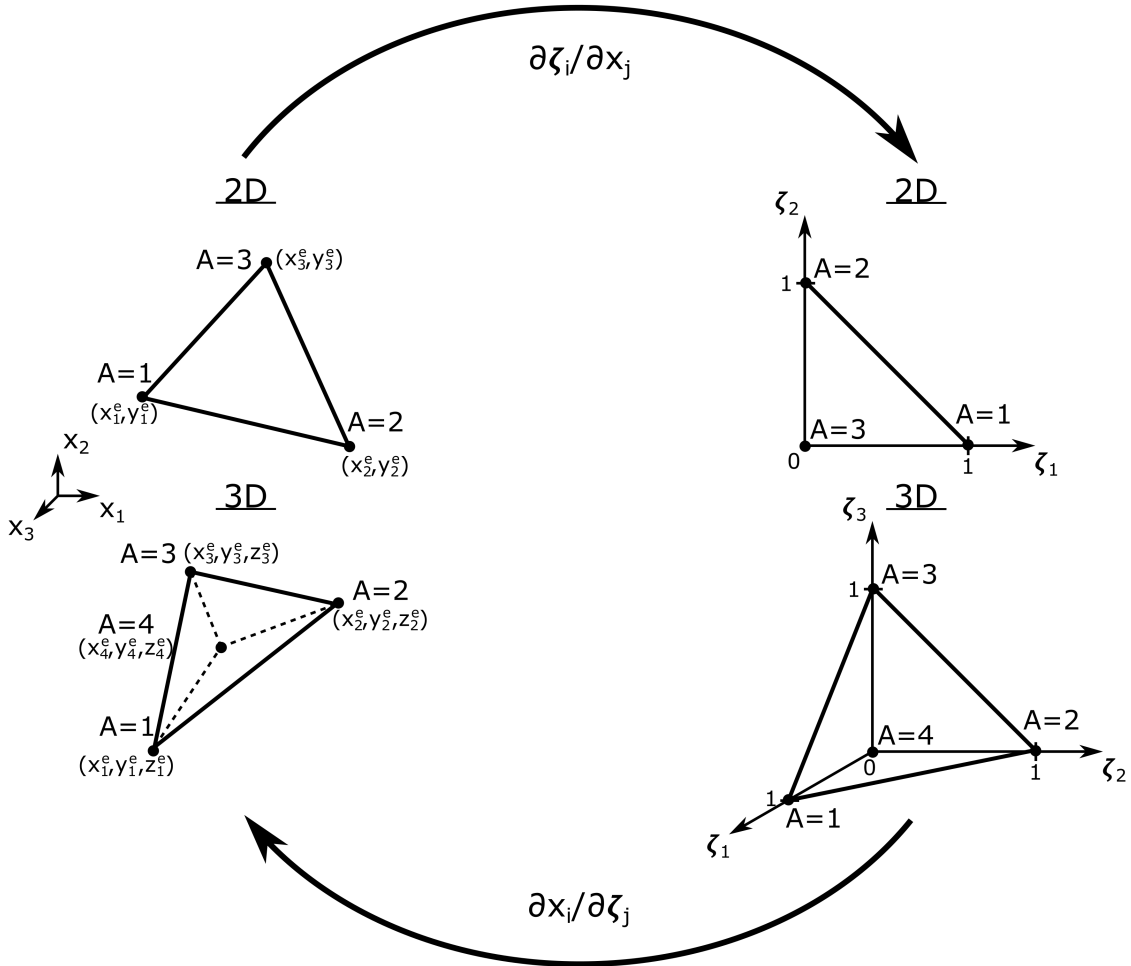
Figure A.2. The inverse of the Jacobian operator maps an arbitrary element onto the isoparametric domain. Triangular and tetrahedral elements will have the bounds $[0, 1]$ in the isoparametric domain. The mapping is reversible.

$$\int_{\Omega_{e_\zeta}} f(\zeta_i) d\Omega_{e_\zeta} \approx \sum_{l_i}^{n_{int_i}} f(\zeta_i^{l_i}) \, \omega_{l_i} \tag{A.18}$$

Where l_i is the index variable for the $\sum_{l_i}^{n_{int_i}}(\cdot)$ operator that belongs to the i'th-direction in the isoparametric element domain, Ω_{e_ζ}; explicitly, l_i does not imply the l_i'th polynomial power of $\zeta_i^{l_i}$. For numerical integration in three dimensions, Gaussian Quadrature employs a triple summation.

$$\int f(\zeta_1, \zeta_2, \zeta_3) d\zeta_1 d\zeta_2 d\zeta_3 \approx \sum_{l_3=1}^{n_{int_3}} \sum_{l_2=1}^{n_{int_2}} \sum_{l_1=1}^{n_{int_1}} f(\zeta_1^{l_1}, \zeta_2^{l_2}, \zeta_3^{l_3}) \, \omega_{l_1} \omega_{l_2} \omega_{l_3} \tag{A.19}$$

In general, the multivariate approach to Gaussian Quadrature involves multiple summations. However, to achieve exact integral evaluation, careful attention must be made to choosing an appropriate number of integration points and weights for each direction according to the highest polynomial order of ζ_i. Gaussian Quadrature can exactly evaluate polynomials of up to order $2n_{int} - 1$. The roots of orthogonal Legendre polynomials are used as the weights; these can be calculated or are easily found as tabulated values. Before applying the Gaussian Quadrature, it is critical that the integration over the general interval $[a, b]$ is transformed into an interval over $[-1, 1]$ for accurate calculation.

Let k_e^{AB} denote the finite element diffusion stiffness matrix for the e'th element where the superscripts A and B represent the index location of $\boldsymbol{k}_e$. Using an element connectivity matrix, the element diffusion matrix will be assembled into the global diffusion stiffness matrix, $\boldsymbol{A}_M$, and be a square matrix equal in size to the number of domain nodes, n_n. The details of this process are discussed in Appendix A.4.

$$\begin{aligned}
\int_{\Omega_e} \frac{\partial \psi_e}{\partial x_i} \sigma_{ij} \frac{\partial u_e}{\partial x_j} d\Omega_e &= \sum_{A=1}^{N} \sum_{B=1}^{N} c_e^A \underbrace{\int_{\Omega_{e_\zeta}} \frac{\partial w^A}{\partial \zeta_k} \frac{\partial \zeta_k}{\partial x_i} \sigma_{ij} \frac{\partial w^B}{\partial \zeta_l} \frac{\partial \zeta_l}{\partial x_j} \det \left| \frac{\partial x_m}{\partial \zeta_n} \right| d\Omega_{e_\zeta}}_{k_e^{AB}} d_e^B \\
&= \sum_{A=1}^{N} \sum_{B=1}^{N} c_e^A k_e^{AB} d_e^B \\
&= \begin{bmatrix} c_e^1 & c_e^2 & \cdots & c_e^N \end{bmatrix} \boldsymbol{k}_e \begin{bmatrix} d_e^1 \\ d_e^2 \\ \vdots \\ d_e^N \end{bmatrix}
\end{aligned} \tag{A.20}$$

A.3   The Complete Electrode Model Matrices

The CEM matrices $\boldsymbol{A}_Z$ and $\boldsymbol{A}_W$ can be formed by isolating the integral on the right-hand side of the equality sign for the weak-form of a discretized domain and providing a similar treatment to these expressions as the finite element diffusion matrix, $\boldsymbol{k}_e$. Equation (A.11) is

reproduced below for convenience and simplified by dropping the summation operator $\sum_e(\cdot)$ with the goal of constructing the finite element matrix expressions of the CEM model.

$$\int_{\Omega_e} \frac{\partial \psi_e}{\partial x_i} \sigma_{ij} \frac{\partial u_e}{\partial x_j} d\Omega_e = \sum_{l=1}^{L} \int_{E_{l\,e}} \frac{1}{z_l}(V_l - u_e)\psi_e dS_e$$

Organize the expression to collect all terms to a single side of the equality and expand the integral corresponding to the boundary electrodes.

$$\int_{\Omega_e} \frac{\partial \psi_e}{\partial x_i} \sigma_{ij} \frac{\partial u_e}{\partial x_j} d\Omega_e + \sum_{l=1}^{L} \int_{E_{l\,e}} \frac{1}{z_l}(u_e - V_l)\psi_e dS_e = 0$$

$$\underbrace{\int_{\Omega_e} \frac{\partial \psi_e}{\partial x_i} \sigma_{ij} \frac{\partial u_e}{\partial x_j} d\Omega_e}_{\boldsymbol{k}_e} + \sum_{l=1}^{L} \underbrace{\int_{E_{l\,e}} \frac{1}{z_l}u_e\psi_e dS_e}_{\boldsymbol{A}_{Z\,e}^l} + \sum_{l=1}^{L} \underbrace{\int_{E_{l\,e}} \left(-\frac{1}{z_l}V_l\psi_e\right) dS_e}_{\boldsymbol{A}_{W\,e}^l} = 0 \qquad (A.21)$$

It is essential to utilize dimensionally appropriate basis functions for the CEM formulation. For example, the formulation of the element diffusion stiffness matrix, $\boldsymbol{k}_e$, uses basis functions that are the same dimension as the domain due to the integration operation occurring over the entire finite element. Whereas the boundary of the domain is one order lower than the dimension of the finite element, such as a face or edge for three or two-dimensional elements, respectively. Consequently, $\boldsymbol{A}_{Z\,e}^l$ and $\boldsymbol{A}_{W\,e}^l$ are formed by collapsing one dimension of the isoparametric domain and utilizing reduced-dimensional basis functions.

To obtain the matrix $\boldsymbol{A}_Z$, consider the first integral operator $\int(\cdot)dS_e$ corresponding to the e'th element of the l'th electrode. By substituting the reduced-dimensional form of the basis function expressions for the potential solution, u_e, and for its variation, ψ_e, we can express the resulting matrix as:

$$\int_{E_{l\,e}} \frac{1}{z_l}u_e\psi_e dS_e = \sum_{A=1}^{N} \sum_{B=1}^{N} c_e^A \underbrace{\int_{\Omega_{e\zeta}} \frac{1}{z_l}w^A w^B d\Omega_{e\xi}}_{A_{Z\,e}^{AB\,l}} d_e^B$$

$$= \sum_{A=1}^{N} \sum_{B=1}^{N} c_e^A A_{Z\,e}^{AB\,l} d_e^B$$

$$= \begin{bmatrix} c_e^1 & c_e^2 & \cdots & c_e^N \end{bmatrix} \boldsymbol{A}_{Z\,e}^l \begin{bmatrix} d_e^1 \\ d_e^2 \\ \vdots \\ d_e^N \end{bmatrix} \qquad (A.22)$$

Here, w represents the reduced-dimensional basis functions for the local nodes A and B of the e'th element, corresponding to the element feature (2D surface or 1D edge) that belongs to the set of elements at the boundary electrodes. The double summation operators treat

the local node numbers as superscript indices. The element matrix $\boldsymbol{A}_{Z\,\text{e}}^l$ is a square matrix with a size equal to the N-number of nodes that make up a finite element's edge/face feature. The global $\boldsymbol{A}_Z$ matrix is a square matrix with a size equal to the total number of nodes in the domain, n_n. It is a sparsely populated matrix with its nonzero values corresponding to the nodes at the electrodes and will contribute to the global diffusion stiffness matrix, $\boldsymbol{A}_M$. Physically, $\boldsymbol{A}_Z$ represents the resistance at the interface between the electrodes and the domain. This effect is known as contact impedance and is assumed to be constant across the electrode surfaces.

To obtain the matrix $\boldsymbol{A}_W$, consider the second integral operator $\int(\cdot)dS_\text{e}$ corresponding to the e'th element of the l'th electrode. By substituting reduced-dimensional basis function expressions for the solution variation, ψ_e, we can express the resulting element matrix $\boldsymbol{A}_{W\,\text{e}}^l$ with the following.

$$
\begin{aligned}
-\int_{E_{l\,\text{e}}} \frac{1}{z_l} V_l \psi_\text{e} dS_\text{e} &= -\sum_{A=1}^{N} c_\text{e}^A \underbrace{\int_{\Omega_{\text{e}_\zeta}} \frac{1}{z_l} w^A d\Omega_{\text{e}_\zeta}}_{A_{W\,\text{e}}^{A\,l}} V_l \\
&= \sum_{A=1}^{N} c_\text{e}^A A_{W\,\text{e}}^{A\,l} V_l \\
&= \begin{bmatrix} c_\text{e}^1 & c_\text{e}^2 & \cdots & c_\text{e}^N \end{bmatrix} \boldsymbol{A}_{W\,\text{e}}^l V_l
\end{aligned}
\tag{A.23}
$$

Here, w represents the reduced-dimensional basis functions for the variation for the A'th node of the e'th element, corresponding to the element feature (2D surface or 1D edge) that belongs to the set of elements at the l'th electrode. Because the voltage at the electrodes is assumed to be constant, V_l is outside the integral operator. The summation operator, $\sum_A^N(\cdot)$, denotes the construction of a column vector for $\boldsymbol{A}_{W\,\text{e}}^l$ with a length, N, equal to the number of element feature nodes corresponding to the electrode boundary. The size of the global $\boldsymbol{A}_W$ has a number of rows equal to the number of nodes of the entire domain, n_n, used in the finite element simulation and the number of columns corresponding to the number of electrodes, L, in the CEM model. Physically, $\boldsymbol{A}_W$ links the domain voltage to the electrodes.

The final CEM matrix $\boldsymbol{A}_D$ can be formed by considering the total current in the system through the conservation of charge, Equation (A.2), and the domain-electrode CEM interface conduction due to contact impedance, Equation (A.4). These expressions have been reproduced below for convenience.

$$
\begin{aligned}
\sum_{l=1}^{L} I_l &= \int_{E_l} \frac{1}{z_l}(V_l - u)dS \\
&= \underbrace{\frac{1}{z_l} E_l}_{A_D^l} V_l - \int_{E_l} \frac{1}{z_l} u dS = 0
\end{aligned}
\tag{A.24}
$$

$$\Rightarrow A_D^l = \int_{E_l} \frac{1}{z_l} dS_\text{e}$$

$$\Rightarrow \boldsymbol{A}_D = \text{diag}\left(\frac{E_l}{z_l}\right) \tag{A.25}$$

Recall I_l and V_l are the current and voltage at the l'th electrodes. The contact impedance, z_l, at the interface between the domain and electrode is assumed to be constant. The second integral operator can be recognized from the derivation of Equation (A.23) with the nodal solution instead of the nodal variation and accounts for the domain-electrode voltage coupling. This integral operator must be evaluated element-by-element using reduced-dimensional basis functions (as was done prior). The first integral operator $\int_{E_l}(\cdot)dS$ corresponds to a surface or line integral taken over the l'th electrode and can be evaluated directly. Evaluating the first integral operator will produce the total length or area, E_l, of the l'th electrode. The element matrix, A_D^l, will be this geometric quantity divided by the contact impedance, z_l. The global $\boldsymbol{A}_D$ matrix will be a square array with a size equal to the total number of electrodes, L, with the diagonal components corresponding to the l'th electrode. Physically, $\boldsymbol{A}_D$ relates the electrode voltages to the electrode currents.

A.3.1 Two-dimensional Elements

This subsection seeks to outline the process of obtaining the two-dimensional element matrices, $\boldsymbol{k}_\text{e}$, $\boldsymbol{A}_{Z\,\text{e}}^l$, and $\boldsymbol{A}_{W\,\text{e}}^l$ through the integration of the basis functions. The matrix $\boldsymbol{A}_D$ can be found directly using geometric relations using nodal coordinates from the FEM mesh. This work employed the use of linear Lagrange basis functions. The work in this section will be outlined using major steps, with the intermediate steps left up to the reader as practice.

Triangular Elements

For two-dimensional elements, three linear basis functions are used, with each local node consisting of a single function. The linear form of the basis functions facilitates easier integration and direct evaluation of the element matrices. Let the basis functions w^A be defined in the isoparametric domain ζ in two dimensions. The basis functions at local node number A are presented as,

$$w^A = \left\{ \begin{array}{c} \zeta_1 \\ \zeta_2 \\ 1 - \zeta_1 - \zeta_2 \end{array} \right\}$$

Taking the gradient of the basis functions with respect to the isoparametric variable, $\frac{\partial w^A}{\partial \xi_\text{i}}$, results in a matrix with constant integer coefficients.

$$\frac{\partial w^A}{\partial \zeta_i} = \begin{bmatrix} \frac{\partial w^1}{\partial \zeta_1} & \frac{\partial w^1}{\partial \zeta_2} \\ \frac{\partial w^2}{\partial \zeta_1} & \frac{\partial w^2}{\partial \zeta_2} \\ \frac{\partial w^3}{\partial \zeta_1} & \frac{\partial w^3}{\partial \zeta_2} \end{bmatrix} = \begin{bmatrix} 1 & 0 \\ 0 & 1 \\ -1 & -1 \end{bmatrix}$$

The isoparametric mapping of the element domain can be represented as a function of the isoparametric domain variable and the nodal coordinates. Recall the isoparametric mapping,

$$x_i^{\mathrm{e}}(\zeta) = \sum_{A=1}^{N} w^A(\zeta) x_{i\,A}^{\mathrm{e}}$$

Let $x_1^{\mathrm{e}} = x^{\mathrm{e}}$ and $x_2^{\mathrm{e}} = y^{\mathrm{e}}$. The indical notation has been abandoned here for the sake of convenience, where x_i^{e} and y_i^{e} are the 'x-' and 'y-coordinate' of the ith node of the eth element. The nodal number is now denoted as the subscript for the nodal coordinates and superscripts for the basis functions.

$$
\begin{aligned}
x^{\mathrm{e}} &= w^1 x_1^{\mathrm{e}} + w^2 x_2^{\mathrm{e}} + w^3 x_3^{\mathrm{e}} \\
&= \zeta_1 x_1^{\mathrm{e}} + \zeta_2 x_2^{\mathrm{e}} + (1 - \zeta_1 - \zeta_2) x_3^{\mathrm{e}} \\
&= \zeta_1 (x_1^{\mathrm{e}} - x_3^{\mathrm{e}}) + \zeta_2 (x_2^{\mathrm{e}} - x_3^2) + x_3^2
\end{aligned}
\qquad
\begin{aligned}
y^{\mathrm{e}} &= w^1 y_1^{\mathrm{e}} + w^2 y_2^{\mathrm{e}} + w^3 y_3^{\mathrm{e}} \\
&= \zeta_1 y_1^{\mathrm{e}} + \zeta_2 y_2^{\mathrm{e}} + (1 - \zeta_1 - \zeta_2) y_3^{\mathrm{e}} \\
&= \zeta_1 (y_1^{\mathrm{e}} - y_3^{\mathrm{e}}) + \zeta_2 (y_2^{\mathrm{e}} - y_3^2) + y_3^{\mathrm{e}}
\end{aligned}
$$

The Jacobian can be formed from the partial derivatives of the isoparametric mapping relations with respect to the isoparametric variable,

$$J = \frac{\partial x_i}{\partial \zeta_j} = \begin{bmatrix} \frac{\partial x^{\mathrm{e}}}{\partial \zeta_1} & \frac{\partial x^{\mathrm{e}}}{\partial \zeta_2} \\ \frac{\partial y^{\mathrm{e}}}{\partial \zeta_1} & \frac{\partial y^{\mathrm{e}}}{\partial \zeta_2} \end{bmatrix} = \begin{bmatrix} x_1^{\mathrm{e}} - x_3^{\mathrm{e}} & x_2^{\mathrm{e}} - x_3^{\mathrm{e}} \\ y_1^{\mathrm{e}} - y_3^{\mathrm{e}} & y_2^{\mathrm{e}} - y_3^{\mathrm{e}} \end{bmatrix}$$

Interestingly, the area of the e'th element can be calculated via $A^{\mathrm{e}} = \frac{1}{2} \det | J |$ in the special case when linear basis function are utilized. Alternatively, the element area can be directly calculated using the nodal coordinates of the vertices,

$$A^{\mathrm{e}} = \frac{1}{2} \det \left| \begin{bmatrix} 1 & x_1^{\mathrm{e}} & y_1^{\mathrm{e}} \\ 1 & x_2^{\mathrm{e}} & y_2^{\mathrm{e}} \\ 1 & x_3^{\mathrm{e}} & y_3^{\mathrm{e}} \end{bmatrix} \right|$$

Recall the expression for the element diffusivity stiffness matrix,

$$k_{\mathrm{e}}^{AB} = \int_{\Omega_{\mathrm{e}\zeta}} \frac{\partial w^A}{\partial \zeta_k} \frac{\partial \zeta_k}{\partial x_i} \sigma_{ij} \frac{\partial w^B}{\partial \zeta_l} \frac{\partial \zeta_l}{\partial x_j} \det \left| \frac{\partial x_m}{\partial \zeta_n} \right| d\Omega_{\mathrm{e}\zeta}$$

By substituting the expressions for the gradient of the basis functions and Jacobian, the diffusion stiffness matrix can be expressed as the following integral:

$$\boldsymbol{k}_{\mathrm{e}} = \int_0^1 \int_0^{1-\zeta_1} \begin{bmatrix} 1 & 0 \\ 0 & 1 \\ -1 & -1 \end{bmatrix} \begin{bmatrix} x_1^{\mathrm{e}} - x_3^{\mathrm{e}} & x_2^{\mathrm{e}} - x_3^{\mathrm{e}} \\ y_1^{\mathrm{e}} - y_3^{\mathrm{e}} & y_2^{\mathrm{e}} - y_3^{\mathrm{e}} \end{bmatrix}^{-1} \begin{bmatrix} \sigma_{11} & \sigma_{12} \\ \sigma_{12} & \sigma_{22} \end{bmatrix} \cdots$$

$$\cdots \begin{bmatrix} x_1^{\mathrm{e}} - x_3^{\mathrm{e}} & x_2^{\mathrm{e}} - x_3^{\mathrm{e}} \\ y_1^{\mathrm{e}} - y_3^{\mathrm{e}} & y_2^{\mathrm{e}} - y_3^{\mathrm{e}} \end{bmatrix}^{-T} \begin{bmatrix} 1 & 0 \\ 0 & 1 \\ -1 & -1 \end{bmatrix}^T \det \left| \begin{bmatrix} x_1^{\mathrm{e}} - x_3^{\mathrm{e}} & x_2^{\mathrm{e}} - x_3^{\mathrm{e}} \\ y_1^{\mathrm{e}} - y_3^{\mathrm{e}} & y_2^{\mathrm{e}} - y_3^{\mathrm{e}} \end{bmatrix} \right| d\zeta_2 d\zeta_1 \qquad (A.26)$$

Notably, the terms inside the double integral are independent of the isoparametric variable (i.e., a constant) and can be pulled out. Due to the fact that the double integral is performed over the entire element in the isoparametric domain, it yields the area of the (unit) triangular element.

$$\boldsymbol{k}_{\mathrm{e}} = \frac{1}{2} \begin{bmatrix} 1 & 0 \\ 0 & 1 \\ -1 & -1 \end{bmatrix} \begin{bmatrix} x_1^{\mathrm{e}} - x_3^{\mathrm{e}} & x_2^{\mathrm{e}} - x_3^{\mathrm{e}} \\ y_1^{\mathrm{e}} - y_3^{\mathrm{e}} & y_2^{\mathrm{e}} - y_3^{\mathrm{e}} \end{bmatrix}^{-1} \begin{bmatrix} \sigma_{11} & \sigma_{12} \\ \sigma_{12} & \sigma_{22} \end{bmatrix} \cdots$$

$$\cdots \begin{bmatrix} x_1^{\mathrm{e}} - x_3^{\mathrm{e}} & x_2^{\mathrm{e}} - x_3^{\mathrm{e}} \\ y_1^{\mathrm{e}} - y_3^{\mathrm{e}} & y_2^{\mathrm{e}} - y_3^{\mathrm{e}} \end{bmatrix}^{-T} \begin{bmatrix} 1 & 0 \\ 0 & 1 \\ -1 & -1 \end{bmatrix}^T \det \left| \begin{bmatrix} x_1^{\mathrm{e}} - x_3^{\mathrm{e}} & x_2^{\mathrm{e}} - x_3^{\mathrm{e}} \\ y_1^{\mathrm{e}} - y_3^{\mathrm{e}} & y_2^{\mathrm{e}} - y_3^{\mathrm{e}} \end{bmatrix} \right| \qquad (A.27)$$

Or alternatively,

$$\boldsymbol{k}_{\mathrm{e}} = A^{\mathrm{e}} \begin{bmatrix} 1 & 0 \\ 0 & 1 \\ -1 & -1 \end{bmatrix} \begin{bmatrix} x_1^{\mathrm{e}} - x_3^{\mathrm{e}} & x_2^{\mathrm{e}} - x_3^{\mathrm{e}} \\ y_1^{\mathrm{e}} - y_3^{\mathrm{e}} & y_2^{\mathrm{e}} - y_3^{\mathrm{e}} \end{bmatrix}^{-1} \begin{bmatrix} \sigma_{11} & \sigma_{12} \\ \sigma_{12} & \sigma_{22} \end{bmatrix} \cdots$$

$$\cdots \begin{bmatrix} x_1^{\mathrm{e}} - x_3^{\mathrm{e}} & x_2^{\mathrm{e}} - x_3^{\mathrm{e}} \\ y_1^{\mathrm{e}} - y_3^{\mathrm{e}} & y_2^{\mathrm{e}} - y_3^{\mathrm{e}} \end{bmatrix}^{-T} \begin{bmatrix} 1 & 0 \\ 0 & 1 \\ -1 & -1 \end{bmatrix}^T \qquad (A.28)$$

Recall that evaluating the CEM matrices $\boldsymbol{A}_Z$ and $\boldsymbol{A}_W$ at the electrode boundaries requires using reduced-dimensional basis functions. In the case of triangular elements, the reduced-dimensional basis functions in the isoparametric domain are collapsed into one dimension over the interval $[-1, 1]$,

$$w^A = \left\{ \begin{array}{c} \frac{1}{2}(1 - \zeta) \\ \frac{1}{2}(1 + \zeta) \end{array} \right\}$$

The expression for the isoparametric mapping of the element edge can be written as a function of a single variable, ζ, by employing the reduced-dimensional basis functions.

$$x^e = w^1 x_1^e + w^2 x_2^e$$
$$= \frac{1}{2}(1-\zeta)x_1^e + \frac{1}{2}(1+\zeta)x_2^e$$
$$= \frac{1}{2}(x_2^e + x_1^e + \zeta(x_2^e - x_1^e))$$

$$y^e = w^1 y_1^e + w^2 y_2^e$$
$$= \frac{1}{2}(1-\zeta)y_1^e + \frac{1}{2}(1+\zeta)y_2^e$$
$$= \frac{1}{2}(y_2^e + y_1^e + \zeta(y_2^e - y_1^e))$$

A subtle consequence of this isoparametric mapping arises to produce a one-dimensional function that represents a multidimensional curve in space. Otherwise known as a bijective parametrization or a parametric function. Let this vector expression take the form $\boldsymbol{r}(\zeta) = \{x^e(\zeta), y^e(\zeta)\}$. Considering the CEM matrices involving the electrode boundaries denote line integrals, it is prudent to approach their evaluation using a bijective parameterization via $\int_C f(\boldsymbol{r})dS = \int_a^b f(\boldsymbol{r}(t))\|\boldsymbol{r}'(t)\|dt$ (recall from calculus on the topic of approaches to evaluate line integrals). The gradient of the isoparametric mapping produces the vector:

$$\boldsymbol{r}'(\zeta) = \frac{\partial x_i}{\partial \zeta} = \left\{ \begin{array}{c} \frac{\partial x^e}{\partial \zeta} \\ \frac{\partial y^e}{\partial \zeta} \end{array} \right\} = \frac{1}{2} \left\{ \begin{array}{c} x_2^e - x_1^e \\ y_2^e - y_1^e \end{array} \right\}$$

A change of variables requires the standard (Euclidean) norm of the gradient vector (similar to taking the determinate of the Jacobian in higher dimensions) to scale the integration to the bounds of the isoparametric domain.

$$\|\boldsymbol{r}'(\zeta)\| = \frac{1}{2}\sqrt{(x_2^e - x_1^e)^2 + (y_2^e - y_1^e)^2} = \frac{h^e}{2} \tag{A.29}$$

Where h^e is the line element length of the e'th element feature (e.g., edge) that belongs to the electrode boundary. By substituting the reduced-dimensional basis functions and employing a bijective parameterization to transform the line integrals to a standard single-variable definite integral in the isoparametric domain, the following simplified expression can be obtained for $\boldsymbol{A}_{Z\,e}^l$.

$$A_{Z\,e}^{AB\,l} = \int_{\Omega_{e\zeta}} \frac{1}{z_l} w^A w^B d\Omega_{e\zeta}$$
$$= \int_{-1}^{1} \frac{1}{4z_l} \begin{bmatrix} 1 - 2\zeta + \zeta^2 & 1 - \zeta^2 \\ 1 - \zeta^2 & 1 + 2\zeta + \zeta^2 \end{bmatrix} \underbrace{\frac{h^e}{2}d\zeta}_{\|\boldsymbol{r}'(\zeta)\|d\Omega_\zeta}$$
$$\boldsymbol{A}_{Z\,e}^l = \frac{h^e}{6z_l} \begin{bmatrix} 2 & 1 \\ 1 & 2 \end{bmatrix} \tag{A.30}$$

Integration can be evaluated directly due to the relatively low polynomial order observed. However, this is mainly due to the fact that the Euclidean norm of the gradient of the isoparametric mapping produces a constant. Leveraging higher-order basis functions will require Gaussian Quadrature. Employing the same approach for $\boldsymbol{A}_{W\,e}^l$, the column vector of the e'th linear line element of the l'th electrode in two-dimensional analysis is,

$$
\begin{aligned}
A_{W\ e}^{A\ l} &= -\int_{\Omega_{e\zeta}} \frac{1}{z_l} w^A d\Omega_{e\zeta} \\
&= -\int_{-1}^{1} \frac{1}{z_l} \begin{bmatrix} \frac{1}{2}(1-\zeta) \\ \frac{1}{2}(1+\zeta) \end{bmatrix} \underbrace{\frac{h^e}{2} d\zeta}_{\|\boldsymbol{r}'(\zeta)\| d\Omega_\zeta} \\
\boldsymbol{A}_{W\ e}^{l} &= -\frac{h^e}{2z_l} \begin{bmatrix} 1 \\ 1 \end{bmatrix}
\end{aligned}
\tag{A.31}
$$

The global matrix, $\boldsymbol{A}_D$ can be formed using purely geometric information provided by the nodal coordinate matrix. Here, the l'th diagonal of $\boldsymbol{A}_D$ corresponds to the quotient of the electrode length, E_l, and contact impedance, z_l. The total length of the electrode can be constructed through a summation of all the line element lengths, h_e, of the e'th element features for the l'th electrode.

$$
\boldsymbol{A}_D(l,l) = \frac{E_l}{z_l} = \frac{1}{z_l} \sum_e h_e
\tag{A.32}
$$

A.3.2 Three-dimensional Elements

This subsection seeks to outline the process of obtaining the three-dimensional element matrices, $\mathbf{k}_e$, $\mathbf{A}_{Z\ e}^l$, and $\mathbf{A}_{W\ e}^l$ through the integration of the basis functions. The matrix $\mathbf{A}_D$ can be found directly using geometric relations using nodal coordinates from the FEM mesh. This work employed the use of linear Lagrange basis functions. The work in the section will be outlined using major steps, with the intermediate steps left up to the reader as practice.

Tetrahedral Elements

For three-dimensional elements, three linear basis functions are used, with each local node consisting of a single function. The linear form of the basis functions for easier integration and evaluation of the element matrices. Let the basis functions w^A be defined in the isoparametric domain ζ in three dimensions. The basis functions at local node number A are presented as,

$$
w^A = \left\{ \begin{array}{c} \zeta_1 \\ \zeta_2 \\ \zeta_3 \\ 1 - \zeta_1 - \zeta_2 - \zeta_3 \end{array} \right\}
$$

Taking the gradient of the linear basis functions with respect to the isoparametric variable, $\frac{\partial w^A}{\partial \xi_i}$, results in a matrix with constant integer coefficients.

134

$$
\frac{\partial w^A}{\partial \zeta_i} = \begin{bmatrix} \frac{\partial w^1}{\partial \zeta_1} & \frac{\partial w^1}{\partial \zeta_2} & \frac{\partial w^1}{\partial \zeta_3} \\ \frac{\partial w^2}{\partial \zeta_1} & \frac{\partial w^2}{\partial \zeta_2} & \frac{\partial w^2}{\partial \zeta_3} \\ \frac{\partial w^3}{\partial \zeta_1} & \frac{\partial w^3}{\partial \zeta_2} & \frac{\partial w^3}{\partial \zeta_3} \\ \frac{\partial w^4}{\partial \zeta_1} & \frac{\partial w^4}{\partial \zeta_2} & \frac{\partial w^4}{\partial \zeta_3} \end{bmatrix} = \begin{bmatrix} 1 & 0 & 0 \\ 0 & 1 & 0 \\ 0 & 0 & 1 \\ -1 & -1 & -1 \end{bmatrix}
$$

The isoparametric mapping of the element domain can be represented as a function of the isoparametric domain variable and the nodal coordinates. Recall the isoparametric mapping,

$$
x_i^e(\zeta) = \sum_{A=1}^{N} w^A(\zeta) x_{i\,A}^e
$$

Let $x_1^e = x^e$, $x_2^e = y^e$, and $x_3^e = z^e$. The indical notation has been abandoned here for the sake of conceptual convenience, where x_i^e, y_i^e, and z_i^e are the 'x-,' 'y-,' and 'z-coordinate' of the i'th node of the e'th element. The nodal number is now denoted as the subscript for the nodal coordinates and superscripts for the basis functions.

$$
\begin{aligned}
x^e &= w^1 x_1^e + w^2 x_2^e + w^3 x_3^e + w^4 x_4^e \\
&= (x_1^e - x_4^e)\zeta_1 + (x_2^e - x_4^e)\zeta_2 + (x_3^e - x_4^e)\zeta_3 + x_4^e \\
y^e &= w^1 y_1^e + w^2 y_2^e + w^3 y_3^e + w^4 y_4^e \\
&= (y_1^e - y_4^e)\zeta_1 + (y_2^e - y_4^e)\zeta_2 + (y_3^e - y_4^e)\zeta_3 + y_4^e \\
z^e &= w^1 z_1^e + w^2 z_2^e + w^3 z_3^e + w^4 z_4^e \\
&= (z_1^e - z_4^e)\zeta_1 + (z_2^e - z_4^e)\zeta_2 + (z_3^e - z_4^e)\zeta_3 + z_4^e
\end{aligned}
$$

The Jacobian can be formed from the partial derivatives of the isoparametric mapping relations with respect to the isoparametric variable,

$$
J = \frac{\partial x_i}{\partial \zeta_j} = \begin{bmatrix} \frac{\partial x^e}{\partial \zeta_1} & \frac{\partial x^e}{\partial \zeta_2} & \frac{\partial x^e}{\partial \zeta_3} \\ \frac{\partial y^e}{\partial \zeta_1} & \frac{\partial y^e}{\partial \zeta_2} & \frac{\partial y^e}{\partial \zeta_3} \\ \frac{\partial z^e}{\partial \zeta_1} & \frac{\partial z^e}{\partial \zeta_2} & \frac{\partial z^e}{\partial \zeta_3} \end{bmatrix} = \begin{bmatrix} x_1^e - x_4^e & x_2^e - x_4^e & x_3^e - x_4^e \\ y_1^e - y_4^e & y_2^e - y_4^e & y_3^e - y_4^e \\ z_1^e - z_4^e & z_2^e - z_4^e & z_3^e - z_4^e \end{bmatrix}
$$

Interestingly, the volume of the eth element can be calculated through the determinate of the Jacobian, $V^e = \frac{1}{6} \det | J |$, in the special case when linear basis functions are utilized. Alternatively, the volume of a tetrahedral can be directly calculated using the nodal coordinates of the vertices,

$$
V^e = \frac{1}{6} \det \begin{vmatrix} 1 & x_1^e & y_1^e & z_1^e \\ 1 & x_2^e & y_2^e & z_2^e \\ 1 & x_3^e & y_3^e & z_3^e \\ 1 & x_4^e & y_4^e & z_4^e \end{vmatrix}
$$

Recall the expression for the element diffusivity stiffness matrix,

$$k_e^{AB} = \int_{\Omega_{e\zeta}} \frac{\partial w^A}{\partial \zeta_k} \frac{\partial \zeta_k}{\partial x_i} \sigma_{ij} \frac{\partial w^B}{\partial \zeta_l} \frac{\partial \zeta_l}{\partial x_j} \det \left| \frac{\partial x_m}{\partial \zeta_n} \right| d\Omega_{e\zeta}$$

By substituting the expressions for the gradient of the basis functions and Jacobian, the diffusion stiffness matrix can be expressed as the following integral:

$$
\begin{aligned}
\boldsymbol{k}_e = \int_0^1 \int_0^{1-\zeta_1} \int_0^{1-\zeta_1-\zeta_2}
\begin{bmatrix} 1 & 0 & 0 \\ 0 & 1 & 0 \\ 0 & 0 & 1 \\ -1 & -1 & -1 \end{bmatrix}
\begin{bmatrix} x_1^e - x_4^e & x_2^e - x_4^e & x_3^e - x_4^e \\ y_1^e - y_4^e & y_2^e - y_4^e & y_3^e - y_4^e \\ z_1^e - z_4^e & z_2^e - z_4^e & z_3^e - z_4^e \end{bmatrix}^{-1} \cdots \\[1em]
\cdots \begin{bmatrix} \sigma_{11} & \sigma_{12} & \sigma_{13} \\ \sigma_{12} & \sigma_{22} & \sigma_{23} \\ \sigma_{13} & \sigma_{23} & \sigma_{33} \end{bmatrix}
\begin{bmatrix} x_1^e - x_4^e & x_2^e - x_4^e & x_3^e - x_4^e \\ y_1^e - y_4^e & y_2^e - y_4^e & y_3^e - y_4^e \\ z_1^e - z_4^e & z_2^e - z_4^e & z_3^e - z_4^e \end{bmatrix}^{-T} \cdots \\[1em]
\cdots \begin{bmatrix} 1 & 0 & 0 \\ 0 & 1 & 0 \\ 0 & 0 & 1 \\ -1 & -1 & -1 \end{bmatrix}^T
\det \left| \begin{bmatrix} x_1^e - x_4^e & x_2^e - x_4^e & x_3^e - x_4^e \\ y_1^e - y_4^e & y_2^e - y_4^e & y_3^e - y_4^e \\ z_1^e - z_4^e & z_2^e - z_4^e & z_3^e - z_4^e \end{bmatrix} \right| d\zeta_3 d\zeta_2 d\zeta_1 \quad \text{(A.33)}
\end{aligned}
$$

Notably, the terms inside the triple integral are constant and can be pulled out. Due to the fact that the triple integral is performed over the entire element in the isoparametric domain, it yields the volume of the (unit) tetrahedral element.

$$
\begin{aligned}
\boldsymbol{k}_e = \frac{1}{6}
\begin{bmatrix} 1 & 0 & 0 \\ 0 & 1 & 0 \\ 0 & 0 & 1 \\ -1 & -1 & -1 \end{bmatrix}
\begin{bmatrix} x_1^e - x_4^e & x_2^e - x_4^e & x_3^e - x_4^e \\ y_1^e - y_4^e & y_2^e - y_4^e & y_3^e - y_4^e \\ z_1^e - z_4^e & z_2^e - z_4^e & z_3^e - z_4^e \end{bmatrix}^{-1} \cdots \\[1em]
\cdots \begin{bmatrix} \sigma_{11} & \sigma_{12} & \sigma_{13} \\ \sigma_{12} & \sigma_{22} & \sigma_{23} \\ \sigma_{13} & \sigma_{23} & \sigma_{33} \end{bmatrix}
\begin{bmatrix} x_1^e - x_4^e & x_2^e - x_4^e & x_3^e - x_4^e \\ y_1^e - y_4^e & y_2^e - y_4^e & y_3^e - y_4^e \\ z_1^e - z_4^e & z_2^e - z_4^e & z_3^e - z_4^e \end{bmatrix}^{-T} \cdots \\[1em]
\cdots \begin{bmatrix} 1 & 0 & 0 \\ 0 & 1 & 0 \\ 0 & 0 & 1 \\ -1 & -1 & -1 \end{bmatrix}^T
\det \left| \begin{bmatrix} x_1^e - x_4^e & x_2^e - x_4^e & x_3^e - x_4^e \\ y_1^e - y_4^e & y_2^e - y_4^e & y_3^e - y_4^e \\ z_1^e - z_4^e & z_2^e - z_4^e & z_3^e - z_4^e \end{bmatrix} \right| \quad \text{(A.34)}
\end{aligned}
$$

Or alternatively,

$$\boldsymbol{k}_\mathrm{e} = V^\mathrm{e} \begin{bmatrix} 1 & 0 & 0 \\ 0 & 1 & 0 \\ 0 & 0 & 1 \\ -1 & -1 & -1 \end{bmatrix} \begin{bmatrix} x_1^\mathrm{e} - x_4^\mathrm{e} & x_2^\mathrm{e} - x_4^\mathrm{e} & x_3^\mathrm{e} - x_4^\mathrm{e} \\ y_1^\mathrm{e} - y_4^\mathrm{e} & y_2^\mathrm{e} - y_4^\mathrm{e} & y_3^\mathrm{e} - y_4^\mathrm{e} \\ z_1^\mathrm{e} - z_4^\mathrm{e} & z_2^\mathrm{e} - z_4^\mathrm{e} & z_3^\mathrm{e} - z_4^\mathrm{e} \end{bmatrix}^{-1} \dots$$

$$\dots \begin{bmatrix} \sigma_{11} & \sigma_{12} & \sigma_{13} \\ \sigma_{12} & \sigma_{22} & \sigma_{23} \\ \sigma_{13} & \sigma_{23} & \sigma_{33} \end{bmatrix} \begin{bmatrix} x_1^\mathrm{e} - x_4^\mathrm{e} & x_2^\mathrm{e} - x_4^\mathrm{e} & x_3^\mathrm{e} - x_4^\mathrm{e} \\ y_1^\mathrm{e} - y_4^\mathrm{e} & y_2^\mathrm{e} - y_4^\mathrm{e} & y_3^\mathrm{e} - y_4^\mathrm{e} \\ z_1^\mathrm{e} - z_4^\mathrm{e} & z_2^\mathrm{e} - z_4^\mathrm{e} & z_3^\mathrm{e} - z_4^\mathrm{e} \end{bmatrix}^{-T} \begin{bmatrix} 1 & 0 & 0 \\ 0 & 1 & 0 \\ 0 & 0 & 1 \\ -1 & -1 & -1 \end{bmatrix}^{T} \tag{A.35}$$

Recall that evaluating the CEM matrices $\boldsymbol{A}_Z$ and $\boldsymbol{A}_W$ at the electrode boundaries requires using reduced-dimensional basis functions. In the case of tetrahedral elements, the reduced-dimensional basis functions in the isoparametric domain are collapsed into two dimensions over the interval $[0,1]$,

$$w^A = \left\{ \begin{array}{c} \zeta_1 \\ \zeta_2 \\ 1 - \zeta_1 - \zeta_2 \end{array} \right\}$$

The expression for the isoparametric mapping of the element area can is represented as,

$$\begin{aligned} x^\mathrm{e} &= w^1 x_1^\mathrm{e} + w^2 x_2^\mathrm{e} + w^3 x_3^\mathrm{e} \\ &= \zeta_1(x_1^\mathrm{e} - x_3^\mathrm{e}) + \zeta_2(x_2^\mathrm{e} - x_3^\mathrm{e}) + x_3^\mathrm{e} \\ y^\mathrm{e} &= w^1 y_1^\mathrm{e} + w^2 y_2^\mathrm{e} + w^3 y_3^\mathrm{e} \\ &= \zeta_1(y_1^\mathrm{e} - y_3^\mathrm{e}) + \zeta_2(y_2^\mathrm{e} - y_3^\mathrm{e}) + y_3^\mathrm{e} \\ z^\mathrm{e} &= w^1 z_1^\mathrm{e} + w^2 z_2^\mathrm{e} + w^3 z_3^\mathrm{e} \\ &= \zeta_1(z_1^\mathrm{e} - z_3^\mathrm{e}) + \zeta_2(z_2^\mathrm{e} - z_3^\mathrm{e}) + z_3^\mathrm{e} \end{aligned}$$

Careful examination of the isoparametric mapping reveals similarities to mapping for triangular elements, now with an extension into the third dimension. When dealing with a 3D domain and 2D electrodes, evaluating $\boldsymbol{A}_Z$ and $\boldsymbol{A}_w$ requires careful attention. The integral transformation for an element, from the original domain to the isoparametric domain, is achieved by the following relation, $dS_\mathrm{e} = \|J\| d\Omega_\zeta$. Where J is the Jacobian of the transformation,

$$J = L_1 \times L_2$$

The gradient of the isoparametric mapping of a surface in 3D space is calculated through,

$$L_\mathrm{i} = \left\{ \begin{array}{c} \frac{\partial x^\mathrm{e}}{\partial \zeta_\mathrm{i}} \\ \frac{\partial y^\mathrm{e}}{\partial \zeta_\mathrm{i}} \\ \frac{\partial z^\mathrm{e}}{\partial \zeta_\mathrm{i}} \end{array} \right\}$$

In the special case when linear basis functions are utilized, the area of the e'th element is calculated via $A^{\mathrm{e}} = \frac{1}{2}\|J\|$. Alternatively, the area of the triangular element can be determined through the Euclidian norm of the cross-product of two vectors constructed by the two edges of the element through a common vertex.

$$A^{\mathrm{e}} = \frac{1}{2} \left\| \begin{Bmatrix} x_1^{\mathrm{e}} - x_3^{\mathrm{e}} \\ y_1^{\mathrm{e}} - y_3^{\mathrm{e}} \\ z_1^{\mathrm{e}} - z_3^{\mathrm{e}} \end{Bmatrix} \times \begin{Bmatrix} x_2^{\mathrm{e}} - x_3^{\mathrm{e}} \\ y_2^{\mathrm{e}} - y_3^{\mathrm{e}} \\ z_2^{\mathrm{e}} - z_3^{\mathrm{e}} \end{Bmatrix} \right\| \tag{A.36}$$

Substituting the reduced-dimensional basis functions and employing an integral transformation to the isoparametric domain, the following simplified expression can be obtained for $\boldsymbol{A}_{Z\,\mathrm{e}}^l$.

$$
\begin{aligned}
A_{Z\,\mathrm{e}}^{AB\,l} &= \int_{\Omega_{\mathrm{e}\zeta}} \frac{1}{z_l} w^A w^B d\Omega_{\mathrm{e}\zeta} \\
&= \int_0^1 \int_0^{1-\zeta_1} \frac{1}{z_l} \begin{bmatrix} \zeta_1^2 & \zeta_1\zeta_2 & \zeta_1(1-\zeta_1-\zeta_2) \\ \zeta_1\zeta_2 & \zeta_2^2 & \zeta_2(1-\zeta_1-\zeta_2) \\ \zeta_1(1-\zeta_1-\zeta^2) & \zeta_2(1-\zeta_1-\zeta_2) & (1-\zeta_1-\zeta_2)^2 \end{bmatrix} \underbrace{(2A^{\mathrm{e}})d\zeta_2 d\zeta_1}_{\|J\|d\Omega_\zeta} \\
\boldsymbol{A}_{Z\,\mathrm{e}}^l &= \frac{A^{\mathrm{e}}}{12z_l} \begin{bmatrix} 2 & 1 & 1 \\ 1 & 2 & 1 \\ 1 & 1 & 2 \end{bmatrix}
\end{aligned}
\tag{A.37}
$$

Integration can be evaluated directly due to the relatively low polynomial order observed. However, this is mainly due to the fact that the Euclidean norm of the Jacobian is a constant. Employing the same approach for $A_{W\,\mathrm{e}}^l$, the column vector of the e'th surface feature of the l'th electrode in a three-dimensional domain is,

$$
\begin{aligned}
A_{W\,\mathrm{e}}^{A\,l} &= -\int_{\Omega_{\mathrm{e}\zeta}} \frac{1}{z_l} w^A d\Omega_{\mathrm{e}\zeta} \\
&= -\int_0^1 \int_0^{1-\zeta_1} \frac{1}{z_l} \begin{bmatrix} \zeta_1 \\ \zeta_2 \\ 1-\zeta_1-\zeta_2 \end{bmatrix} \underbrace{(2A^{\mathrm{e}})d\zeta_2 d\zeta_1}_{\|J\|d\Omega_\zeta} \\
\boldsymbol{A}_{W\,\mathrm{e}}^l &= -\frac{A^{\mathrm{e}}}{3z_l} \begin{bmatrix} 1 \\ 1 \\ 1 \end{bmatrix}
\end{aligned}
\tag{A.38}
$$

The global matrix, $\boldsymbol{A}_D$ can be formed using purely geometric information provided by the nodal coordinate matrix. Here, the l'th diagonal of $\boldsymbol{A}_D$ corresponds to the quotient of the electrode area, E_l, and contact impedance, z_l. The total area of the electrode can be constructed through a summation of all the element areas, A^{e}, of the e'th element features for the l'th electrode.

$$\boldsymbol{A}_D(l,l) = \frac{E_l}{z_l} = \frac{1}{z_l}\sum_{\mathrm{e}} A^{\mathrm{e}} \tag{A.39}$$

A.4 Matrix Assembly

The matrix assembly process is a crucial step in solving the system of linear equations to obtain a physically meaningful FEM solution. To facilitate an enhanced conceptual understanding of the assembly process, it is advisable to initially consider an arbitrary element, as seen in Figure A.3.
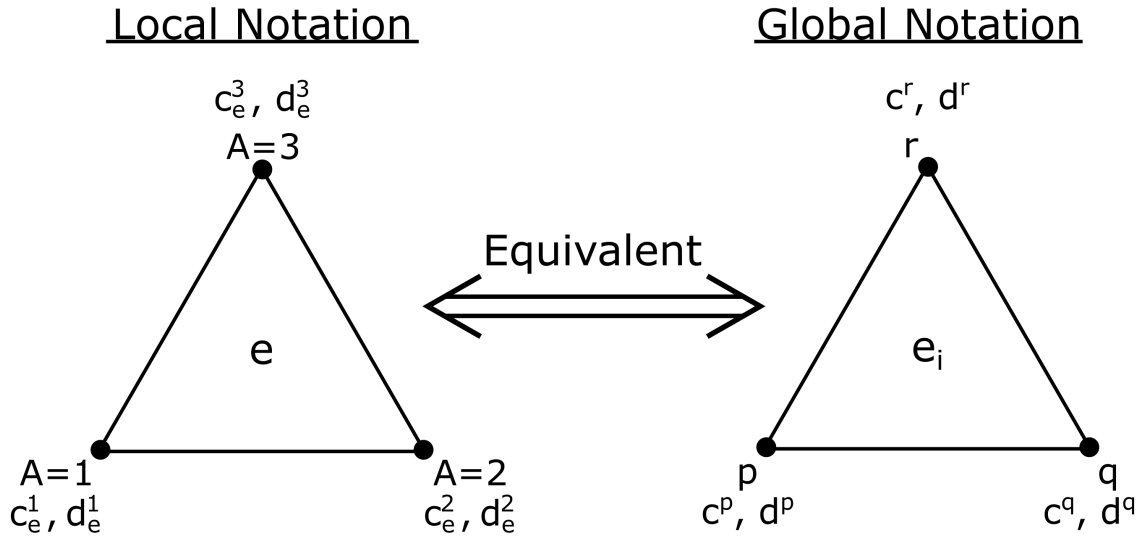
Figure A.3. A simple diagram showing the equivalent local and global notation for a single triangular element. The local node numbers, $A = 1, 2, 3$, are denoted with the arbitrary node numbers p, q, and r in the global notation scheme. It is important to note that a single node will maintain its global notation while belonging to multiple neighboring elements.

When Equation (A.20) is evaluated for a two-dimensional domain and triangular element, the element stiffness matrix will take the general form using the local notation,

$$\boldsymbol{c}_{\mathrm{e}}^T \boldsymbol{k}_{\mathrm{e}} \boldsymbol{d}_{\mathrm{e}} = c_{\mathrm{e}}^A k_{\mathrm{e}}^{AB} d_{\mathrm{e}}^B = \begin{bmatrix} c_{\mathrm{e}}^1 & c_{\mathrm{e}}^2 & c_{\mathrm{e}}^3 \end{bmatrix} \begin{bmatrix} k_{\mathrm{e}}^{11} & k_{\mathrm{e}}^{12} & k_{\mathrm{e}}^{13} \\ k_{\mathrm{e}}^{12} & k_{\mathrm{e}}^{22} & k_{\mathrm{e}}^{23} \\ k_{\mathrm{e}}^{13} & k_{\mathrm{e}}^{23} & k_{\mathrm{e}}^{33} \end{bmatrix} \begin{bmatrix} d_{\mathrm{e}}^1 \\ d_{\mathrm{e}}^2 \\ d_{\mathrm{e}}^3 \end{bmatrix}$$

Recall super scripts A and B denote the index location of the element stiffness matrix, k_{e}^{AB}, and vector index location for c_{e}^A and d_{e}^B using the local numbering of the nodes. However, the finite element mesh is described using a global numbering scheme. For an arbitrary element, $\mathrm{e_i}$, the equivalent numbering and notation are expressed as,

139

$$\boldsymbol{c}^T \boldsymbol{k}_{\mathrm{e_i}} \boldsymbol{d} = \begin{bmatrix} c^p & c^q & c^r \end{bmatrix} \begin{bmatrix} k_{\mathrm{e_i}}^{11} & k_{\mathrm{e_i}}^{12} & k_{\mathrm{e_i}}^{13} \\ k_{\mathrm{e_i}}^{12} & k_{\mathrm{e_i}}^{22} & k_{\mathrm{e_i}}^{23} \\ k_{\mathrm{e_i}}^{13} & k_{\mathrm{e_i}}^{23} & k_{\mathrm{e_i}}^{33} \end{bmatrix} \begin{bmatrix} d^p \\ d^q \\ d^r \end{bmatrix}$$

Where the quantities $[d^p, d^q, d^r]^T$ and $[c^p, c^q, c^r]$ are the potential solution and variation for three arbitrary nodes belonging to the $\mathrm{e_i}$'th element in the global numbering scheme. These three quantities represent a vector subset of the potential solution and variation vectors for the entire mesh. In general, the global stiffness matrix, $\boldsymbol{A}_M$, can be constructed through a summation of the total number of elements that map element stiffness matrix contributions with the corresponding appropriate nodal variation, $\boldsymbol{c}$, and solution, $\boldsymbol{d}$.

$$\begin{bmatrix} \boldsymbol{c}^T \end{bmatrix} \begin{bmatrix} \boldsymbol{A}_M \end{bmatrix} \begin{bmatrix} \boldsymbol{d} \end{bmatrix} = \sum_{\mathrm{e}} \boldsymbol{c}_{\mathrm{e}}^T \boldsymbol{k}_{\mathrm{e}} \boldsymbol{d}_{\mathrm{e}}$$

As an example, consider the two-dimensional triangular mesh is shown in Figure A.4 (a). From observation, the domain contains two electrodes at the boundary and is discretized into 8 elements. In an effort to enhance conceptual understanding of the assembly process, an element-by-element approach is employed. Figure A.4 (b-c) presents a clear and visually distinguishable representation of the individual elements in a color-coded assembly drawing explosion schematic. Equations (A.40)-(A.47) provide the individual element stiffness matrices for each element following the labeling convention presented in Figure A.3. The left and right sides of the equality sign represent the local and global notation of the element stiffness matrix in a color-coded fashion. Special attention is given to the right-hand side of the equation, it is important to observe structure and ordering of the element stiffness matrix is preserved with respect to the local node numbering. However, the local node numbering represented in the accompanying potential solution and variation vectors is replaced with the global node numbering of the mesh. When viewed from the perspective of maintaining a system of linear equations through a reordering of vector-matrix operations, the assembly process of the global stiffness matrix involves the summation of contributions from a set of smaller equations. The expanded global stiffness matrix is presented in Equation (A.48) and more compactly in Equation (A.49).

$$\text{Element 1: } \begin{bmatrix} c_e^1 & c_e^2 & c_e^3 \end{bmatrix} \begin{bmatrix} k_e^{11} & k_e^{12} & k_e^{13} \\ k_e^{12} & k_e^{22} & k_e^{23} \\ k_e^{13} & k_e^{23} & k_e^{33} \end{bmatrix} \begin{bmatrix} d_e^1 \\ d_e^2 \\ d_e^4 \end{bmatrix} \Leftrightarrow \begin{bmatrix} c^2 & c^1 & c^4 \end{bmatrix} \begin{bmatrix} k_{e_1}^{11} & k_{e_1}^{12} & k_{e_1}^{13} \\ k_{e_1}^{12} & k_{e_1}^{22} & k_{e_1}^{23} \\ k_{e_1}^{13} & k_{e_1}^{23} & k_{e_1}^{33} \end{bmatrix} \begin{bmatrix} d^2 \\ d^1 \\ d^4 \end{bmatrix} \quad (A.40)$$

$$\text{Element 2: } \begin{bmatrix} c_e^1 & c_e^2 & c_e^3 \end{bmatrix} \begin{bmatrix} k_e^{11} & k_e^{12} & k_e^{13} \\ k_e^{12} & k_e^{22} & k_e^{23} \\ k_e^{13} & k_e^{23} & k_e^{33} \end{bmatrix} \begin{bmatrix} d_e^1 \\ d_e^2 \\ d_e^3 \end{bmatrix} \Leftrightarrow \begin{bmatrix} c^2 & c^4 & c^5 \end{bmatrix} \begin{bmatrix} k_{e_2}^{11} & k_{e_2}^{12} & k_{e_2}^{13} \\ k_{e_2}^{12} & k_{e_2}^{22} & k_{e_2}^{23} \\ k_{e_2}^{13} & k_{e_2}^{23} & k_{e_2}^{33} \end{bmatrix} \begin{bmatrix} d^2 \\ d^4 \\ d^5 \end{bmatrix} \quad (A.41)$$

$$\text{Element 3: } \begin{bmatrix} c_e^1 & c_e^2 & c_e^3 \end{bmatrix} \begin{bmatrix} k_e^{11} & k_e^{12} & k_e^{13} \\ k_e^{12} & k_e^{22} & k_e^{23} \\ k_e^{13} & k_e^{23} & k_e^{33} \end{bmatrix} \begin{bmatrix} d_e^1 \\ d_e^2 \\ d_e^3 \end{bmatrix} \Leftrightarrow \begin{bmatrix} c^2 & c^5 & c^6 \end{bmatrix} \begin{bmatrix} k_{e_3}^{11} & k_{e_3}^{12} & k_{e_3}^{13} \\ k_{e_3}^{12} & k_{e_3}^{22} & k_{e_3}^{23} \\ k_{e_3}^{13} & k_{e_3}^{23} & k_{e_3}^{33} \end{bmatrix} \begin{bmatrix} d^2 \\ d^5 \\ d^6 \end{bmatrix} \quad (A.42)$$

$$\text{Element 4: } \begin{bmatrix} c_e^1 & c_e^2 & c_e^3 \end{bmatrix} \begin{bmatrix} k_e^{11} & k_e^{12} & k_e^{13} \\ k_e^{12} & k_e^{22} & k_e^{23} \\ k_e^{13} & k_e^{23} & k_e^{33} \end{bmatrix} \begin{bmatrix} d_e^1 \\ d_e^2 \\ d_e^3 \end{bmatrix} \Leftrightarrow \begin{bmatrix} c^3 & c^2 & c^6 \end{bmatrix} \begin{bmatrix} k_{e_4}^{11} & k_{e_4}^{12} & k_{e_4}^{13} \\ k_{e_4}^{12} & k_{e_4}^{22} & k_{e_4}^{23} \\ k_{e_4}^{13} & k_{e_4}^{23} & k_{e_4}^{33} \end{bmatrix} \begin{bmatrix} d^3 \\ d^2 \\ d^6 \end{bmatrix} \quad (A.43)$$

$$\text{Element 5: } \begin{bmatrix} c_e^1 & c_e^2 & c_e^3 \end{bmatrix} \begin{bmatrix} k_e^{11} & k_e^{12} & k_e^{13} \\ k_e^{12} & k_e^{22} & k_e^{23} \\ k_e^{13} & k_e^{23} & k_e^{33} \end{bmatrix} \begin{bmatrix} d_e^1 \\ d_e^2 \\ d_e^3 \end{bmatrix} \Leftrightarrow \begin{bmatrix} c^4 & c^7 & c^8 \end{bmatrix} \begin{bmatrix} k_{e_5}^{11} & k_{e_5}^{12} & k_{e_5}^{13} \\ k_{e_5}^{12} & k_{e_5}^{22} & k_{e_5}^{23} \\ k_{e_5}^{13} & k_{e_5}^{23} & k_{e_5}^{33} \end{bmatrix} \begin{bmatrix} d^4 \\ d^7 \\ d^8 \end{bmatrix} \quad (A.44)$$

$$\text{Element 6: } \begin{bmatrix} c_e^1 & c_e^2 & c_e^3 \end{bmatrix} \begin{bmatrix} k_e^{11} & k_e^{12} & k_e^{13} \\ k_e^{12} & k_e^{22} & k_e^{23} \\ k_e^{13} & k_e^{23} & k_e^{33} \end{bmatrix} \begin{bmatrix} d_e^1 \\ d_e^2 \\ d_e^3 \end{bmatrix} \Leftrightarrow \begin{bmatrix} c^5 & c^4 & c^8 \end{bmatrix} \begin{bmatrix} k_{e_6}^{11} & k_{e_6}^{12} & k_{e_6}^{13} \\ k_{e_6}^{12} & k_{e_6}^{22} & k_{e_6}^{23} \\ k_{e_6}^{13} & k_{e_6}^{23} & k_{e_6}^{33} \end{bmatrix} \begin{bmatrix} d^5 \\ d^4 \\ d^8 \end{bmatrix} \quad (A.45)$$

$$\text{Element 7: } \begin{bmatrix} c_e^1 & c_e^2 & c_e^3 \end{bmatrix} \begin{bmatrix} k_e^{11} & k_e^{12} & k_e^{13} \\ k_e^{12} & k_e^{22} & k_e^{23} \\ k_e^{13} & k_e^{23} & k_e^{33} \end{bmatrix} \begin{bmatrix} d_e^1 \\ d_e^2 \\ d_e^3 \end{bmatrix} \Leftrightarrow \begin{bmatrix} c^6 & c^5 & c^8 \end{bmatrix} \begin{bmatrix} k_{e_7}^{11} & k_{e_7}^{12} & k_{e_7}^{13} \\ k_{e_7}^{12} & k_{e_7}^{22} & k_{e_7}^{23} \\ k_{e_7}^{13} & k_{e_7}^{23} & k_{e_7}^{33} \end{bmatrix} \begin{bmatrix} d^6 \\ d^5 \\ d^8 \end{bmatrix} \quad (A.46)$$

$$\text{Element 8: } \begin{bmatrix} c_e^1 & c_e^2 & c_e^3 \end{bmatrix} \begin{bmatrix} k_e^{11} & k_e^{12} & k_e^{13} \\ k_e^{12} & k_e^{22} & k_e^{23} \\ k_e^{13} & k_e^{23} & k_e^{33} \end{bmatrix} \begin{bmatrix} d_e^1 \\ d_e^2 \\ d_e^3 \end{bmatrix} \Leftrightarrow \begin{bmatrix} c^6 & c^8 & c^9 \end{bmatrix} \begin{bmatrix} k_{e_8}^{11} & k_{e_8}^{12} & k_{e_8}^{13} \\ k_{e_8}^{12} & k_{e_8}^{22} & k_{e_8}^{23} \\ k_{e_8}^{13} & k_{e_8}^{23} & k_{e_8}^{33} \end{bmatrix} \begin{bmatrix} d^6 \\ d^8 \\ d^9 \end{bmatrix} \quad (A.47)$$

$$\left[\boldsymbol{A}_M\right] = \begin{bmatrix}
k_{e_1}^{22} & k_{e_1}^{12} & 0 & k_{e_1}^{23} & 0 & 0 & 0 & 0 & 0 \\[4pt]
k_{e_1}^{12} & k_{e_1}^{11}+k_{e_2}^{11}+k_{e_3}^{11}+k_{e_4}^{22} & k_{e_4}^{12} & k_{e_1}^{13}+k_{e_2}^{12} & k_{e_2}^{13}+k_{e_3}^{12} & k_{e_3}^{13}+k_{e_4}^{23} & 0 & 0 & 0 \\[4pt]
0 & k_{e_4}^{12} & k_{e_4}^{11} & 0 & 0 & k_{e_4}^{13} & 0 & 0 & 0 \\[4pt]
k_{e_1}^{23} & k_{e_1}^{13}+k_{e_2}^{12} & 0 & k_{e_1}^{33}+k_{e_2}^{22}+k_{e_5}^{11}+k_{e_6}^{22} & k_{e_2}^{23}+k_{e_6}^{12} & 0 & k_{e_5}^{12} & k_{e_5}^{13}+k_{e_6}^{23} & 0 \\[4pt]
0 & k_{e_2}^{13}+k_{e_3}^{12} & 0 & k_{e_2}^{23}+k_{e_6}^{12} & k_{e_2}^{33}+k_{e_3}^{22}+k_{e_6}^{11}+k_{e_7}^{22} & k_{e_3}^{23}+k_{e_7}^{12} & 0 & k_{e_6}^{13}+k_{e_7}^{23} & 0 \\[4pt]
0 & k_{e_3}^{13}+k_{e_4}^{23} & k_{e_4}^{13} & 0 & k_{e_3}^{23}+k_{e_7}^{12} & k_{e_3}^{33}+k_{e_4}^{33}+k_{e_7}^{11}+k_{e_8}^{11} & 0 & k_{e_7}^{13}+k_{e_8}^{12} & k_{e_8}^{13} \\[4pt]
0 & 0 & 0 & k_{e_5}^{12} & 0 & 0 & k_{e_5}^{22} & k_{e_5}^{23} & 0 \\[4pt]
0 & 0 & 0 & k_{e_5}^{13}+k_{e_6}^{23} & k_{e_6}^{13}+k_{e_7}^{23} & k_{e_7}^{13}+k_{e_8}^{12} & k_{e_5}^{23} & k_{e_5}^{33}+k_{e_6}^{33}+k_{e_7}^{33}+k_{e_8}^{22} & k_{e_8}^{23} \\[4pt]
0 & 0 & 0 & 0 & 0 & k_{e_8}^{13} & 0 & k_{e_8}^{23} & k_{e_8}^{33}
\end{bmatrix}$$

$$(A.48)$$

$$\Rightarrow \begin{bmatrix} c^1 & c^2 & c^3 & c^4 & c^5 & c^6 & c^7 & c^8 & c^9 \end{bmatrix} \left[\boldsymbol{A}_M\right] \begin{bmatrix} d^1 \\ d^2 \\ d^3 \\ d^4 \\ d^5 \\ d^6 \\ d^7 \\ d^8 \\ d^9 \end{bmatrix} \qquad (A.49)$$
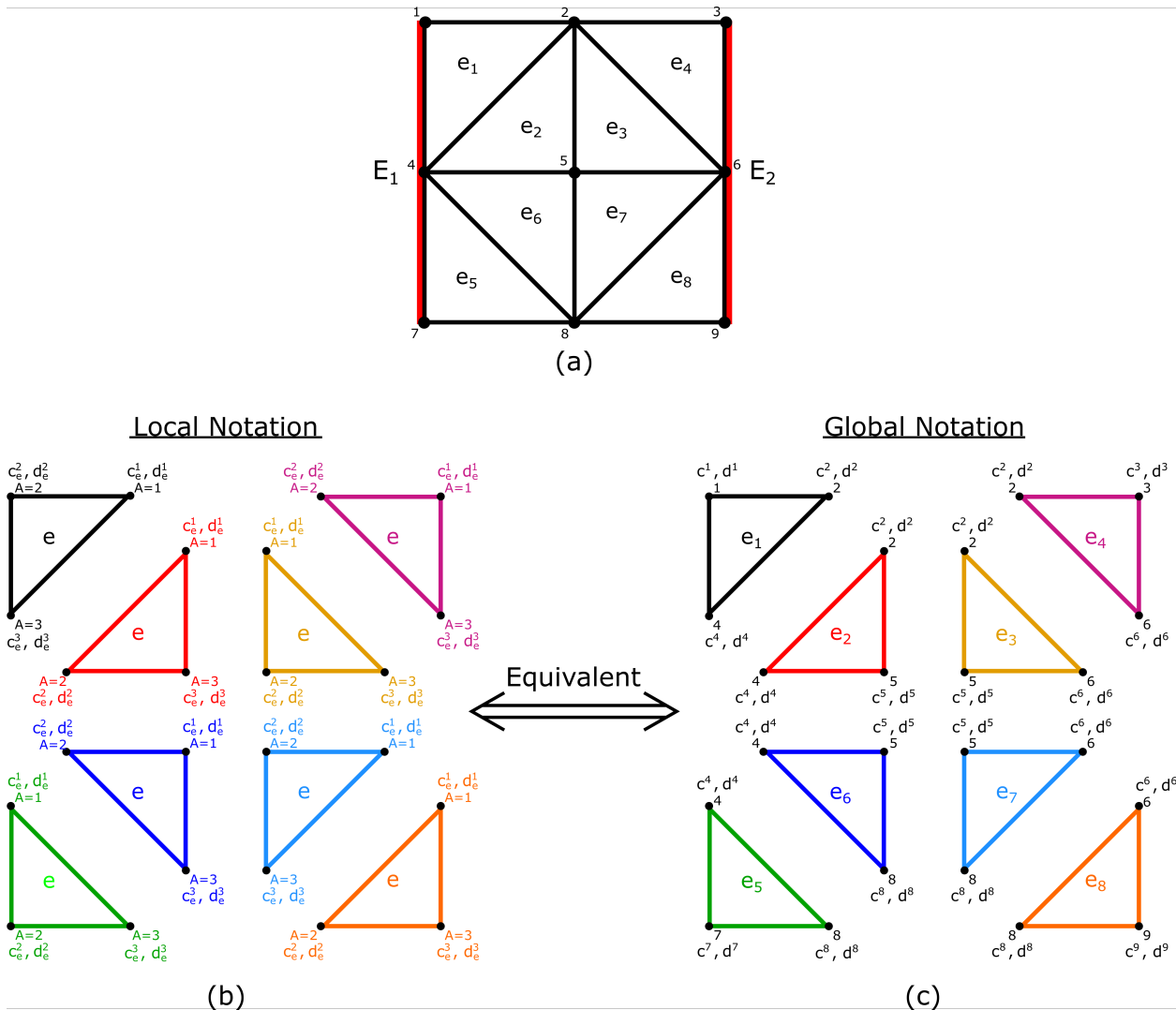
Figure A.4. (a) A 2D rectangular domain is discretized into 8 triangular elements. Electrodes are attached to the domain boundary. (b) An assembly explosion of the mesh with the color-coded elements labeled with a local numbering notation. (c) An assembly explosion of the mesh with the color-coded elements labeled with an equivalent global numbering and notation.

143

B. Coding Efficiency and Implementation in MATLAB

The complete electrode model and analytical piezoresistivity code were written by the author in MATLAB (Mathworks, Natick, MA, USA), a programming language commonly used for scientific numerical computing. Some defining features of MATLAB include matrix multiplication, implementation of algorithms, and interfacing with external programs such as ABAQUS. However, computational resources are finite, and implementing efficient coding practices is crucial for expensive or large operations. For example, the construction of the global stiffness matrix or solving a large system of linear equations, $Ax = b$. This chapter of the appendix aims to empower the reader with some of the best practices employed by the author. This resource is not all-inclusive, and the reader is encouraged to discover and implement further tools or practices for enhanced coding efficiency.

B.1   Sparse Matrices

A consequence of employing many degrees of freedom for FEM is the construction of large and very sparsely populated matrices. A sparse matrix is defined to be a matrix primarily populated by zeros as elements of the table. Typically, this is not a problem. However, it is important to consider that while machines have the capability to handle and solve large systems of linear equations with sufficient computational resources, the memory storage requirements for both sparsely and densely populated matrices remain the same when utilizing full storage organization in the MATLAB workspace. From a computer science perspective, sparsely or densely populated matrices of equal size have identical memory requirements when using full storage organization in MATLAB. This is because zero-valued elements utilize the same number of bits as any other element in the matrix (e.g., signed integers/decimals).

Employing sparse matrix storage and operations in MATLAB is one potential solution for proper memory management [129]. The *sparse()* command in MATLAB can reduce the memory overhead required to represent large matrices by only storing the index location and value of non-zero elements. This can lead to a potentially dramatic reduction of memory required for data storage of sparsely populated matrices. In MATLAB, there are two main approaches to constructing a matrix with the sparse attribute. However, the most appropriate choice depends on prior knowledge of the memory limitations of the machine employed. Consider the coefficient matrix for a system of linear equations, A. In the first approach, the full matrix A does not exceed the machine's random access memory (RAM) or MATLAB's workspace memory limits. The *sparse()* command can be directly applied to the matrix A. Comparison between the original and sparse matrices will show a dramatic reduction in size for a sufficiently large matrix size with a significant percentage of zero-valued elements. In the second approach, the construction of the full matrix A will exceed the memory limitations of the machine; exceeding the memory limitations is a common problem in FEM. Construction of the sparse matrix should be approached as the concatenation of vectors that denote the non-zero entries at certain rows and columns within the matrix. The concatenation is practically executed triplicate indexing. For example, the global stiffness matrix,

Equation (A.48), can be constructed from the global notation of Equation (A.40)-Equation (A.47) with the one-time call of the *sparse(i,j,v)* function,

$$
i = \begin{Bmatrix} 2 \\ 1 \\ 4 \\ 2 \\ 1 \\ 4 \\ 2 \\ 1 \\ 4 \\ 2 \\ 4 \\ 5 \\ 2 \\ 4 \\ \vdots \end{Bmatrix}, \quad
j = \begin{Bmatrix} 2 \\ 2 \\ 2 \\ 1 \\ 1 \\ 1 \\ 4 \\ 4 \\ 4 \\ 2 \\ 2 \\ 2 \\ 4 \\ 4 \\ \vdots \end{Bmatrix}, \quad
v = \begin{Bmatrix} k_{e_1}^{11} \\ k_{e_1}^{12} \\ k_{e_1}^{13} \\ k_{e_1}^{12} \\ k_{e_1}^{22} \\ k_{e_1}^{23} \\ k_{e_1}^{13} \\ k_{e_1}^{23} \\ k_{e_1}^{33} \\ \color{red}{k_{e_2}^{11}} \\ \color{red}{k_{e_2}^{12}} \\ \color{red}{k_{e_2}^{13}} \\ \color{red}{k_{e_2}^{12}} \\ \color{red}{k_{e_2}^{22}} \\ \vdots \end{Bmatrix}
\tag{B.1}
$$

Triplet notation i, j, v denotes the construction of the sparse matrix, $A_M(\mathrm{i}(k), \mathrm{j}(k)) = v(k)$, through vectorization. It is important to note that vectorized array elements with repeated indices are summed, and the newly created matrix with the sparse attribute is considered a distinct storage class within the workspace. While the sparse matrix is considered a different storage class than the full matrix, it contains the same information. Furthermore, the integrity of matrix operations is preserved. Matrices with the sparse attribute in MATLAB do not require special treatment in regard to matrix operations such as multiplication/division, addition/subtraction, and inversion. Significant computational time improvements can be found for matrices, with more than a third of the table elements being zero-valued.

B.2 Parallel Computing Toolbox

Multi-core processors and sophisticated graphical processing units (GPUs) are commonplace in modern computing systems. Advancement in hardware architecture has led to significant improvements in computational capabilities. To harness the advancements in multi-core processing, MathWorks has developed the Parallel Computing Toolbox to accelerate data processing. This toolbox effectively distributes the workload across multiple cores, also known as workers, enabling the efficient and expedient execution of computationally demanding tasks. For instance, the parallel processing toolbox can significantly reduce the execution time for matrix calculations that would exceed the memory capacity of a single machine. Furthermore, this can be scaled up to clusters and cloud computing. However, it is important to note that effective utilization of the parallel computing toolbox necessitates appropriate construction of transparent code structures.

B.3 Pseudo-code and Algorithms

The following MATLAB pseudo-code provides a high-level representation of the implementation steps for the complete electrode model and the assembly of its constitutive matrices. This section aims to decrease the implementation time for writing their own code. To improve performance, the following pseudo-code incorporates MATLAB's *sparse()* function and the parallel computing toolbox. These tools assist in mitigating memory bottlenecks and enhancing computational efficiency during the process of scaling to evaluate finite element domains with potentially millions of elements or cloud computing on cluster machines. In the author's experience, these tools helped reduce the execution time from several hours to a few minutes on a quad-core machine and eight gigabytes of RAM. Outlined below is the pseudo-code for the complete electrode model and associated matrix assembly algorithms. The author encourages the reader to make further improvements and enhancements to meet the demands of their specific applications.

Complete Electrode Model Pseudo-code:

1: Load: Element Connectivity, Nodal Coordinates, and Electrode Connectivity matrices
2: Extract mesh parameters:
3:    n_n: Total number of domain nodes
4: Define:
5:    z_l: Contact impedance
6:    σ_e: Element conductivity (cells)
7:    I_0: Current amplitude
8: Initialize Parallel Computing Toolbox
9:    *parpool('Processes')*
10: Construct CEM 'A' matrix:
11:    Call Algorithm 1 $\boldsymbol{A}_M$ Assembly
12:    Call Algorithm 2 $\boldsymbol{A}_Z$ Assembly
13:    Call Algorithm 3 $\boldsymbol{A}_W$ Assembly
14:    Call Algorithm 4 $\boldsymbol{A}_D$ Assembly
15:    $\boldsymbol{A} = \begin{bmatrix} \boldsymbol{A}_M + \boldsymbol{A}_Z & \boldsymbol{A}_W \\ \boldsymbol{A}_W^T & \boldsymbol{A}_D \end{bmatrix}$
16: Construct CEM 'b' vector:
17:    $b = sparse\left(\left\{ \begin{matrix} zeros(n_n, 1) \\ I \end{matrix} \right\} \right)$
18: Solve for domain and electrode voltages:
19:    **spmd**
20:      $x = codistributed(\boldsymbol{A}) \backslash codistributed(b)$
21:    **end spmd**
22:    $\left\{ \begin{matrix} U \\ V \end{matrix} \right\} = full(gather(x))$
23: Delete the current parallel pool
24:    *delete(gcp)*

146

Algorithm 1 $\boldsymbol{A}_M$ Assembly

1: Import: Element Connectivity, Nodal Coordinates, Element Conductivity
2: Extract mesh parameters:
3:    n_e: Total number of domain elements
4:    n_{ne}: Number of nodes in an element
5:    n_n: Total number of domain nodes
6: Initialize empty cell variables i, j, and v
7: **parfor** $k = 1, 2, \ldots n_e$ **do**
8:    σ_e: Extract conductivity of the k'th element
9:    nodes: Extract global node numbers for the k'th element
10:    x_e: Extract node locations for the k'th element,
11:    $k_e(x_e, \sigma_e)$: Evaluate Equation (A.26) or (A.33)
12:    Store of element degrees of freedom and element diffusion stiffness matrix:
13:       $i\{k\}, j\{k\} \leftarrow$ global node numbers as indices to k_e
14:       $v\{k\} \leftarrow k_e(:)$
15: **end parfor**
16: Assembly of Global Diffusion Stiffness Matrix:
17:    $\boldsymbol{A}_M = sparse(cell2mat(i), cell2mat(j), cell2mat(v), n_n, n_n)$

Algorithm 2 $\boldsymbol{A}_Z$ Assembly

1: Import: Electrode Connectivity, Nodal Coordinates, z_l
2: Extract mesh parameters:
3:    L: Total number of electrodes
4:    n_n: Total number of domain nodes
5: Initialize index counter, $m = 0$
6: **parfor** $l = 1, 2, \ldots L$ **do**
7:    n_e: Define the total number of elements belonging to the l'th electrode
8:    **for** $k = 1, 2, \ldots n_e$ **do**
9:       $m = m + 1$
10:       nodes: Extract global node numbers for the k'th element of the l'th electrode
11:       x_e: Extract node locations for the k'th element of the l'th electrode
12:       $A_{Z\,e}(x_e, z_l)$: Evaluate Equation (A.30) or (A.37)
13:       Store of element degrees of freedom and element matrix:
14:          $i\{m\}, j\{m\} \leftarrow$ global node numbers as indices to $A_{Z\,e}$
15:          $v\{m\} \leftarrow A_{Z\,e}(:)$
16:    **end for**
17: **end parfor**
18: Assembly of $\boldsymbol{A}_Z$ Matrix:
19:    $\boldsymbol{A}_Z = sparse(cell2mat(i), cell2mat(j), cell2mat(v), n_n, n_n)$

Algorithm 3 A_W Assembly

 1: Import: Electrode Connectivity, Nodal Coordinates, z_l

 2: Extract mesh parameters:

 3:    L: Total number of electrodes

 4:    n_n: Total number of domain nodes

 5: Initialize index counter, $m = 0$

 6: **parfor** $l = 1, 2, \ldots L$ **do**

 7:    n_e: Define the total number of elements belonging to the l'th electrode

 8:    **for** $k = 1, 2, \ldots n_e$ **do**

 9:       $m = m + 1$

10:       nodes: Extract global node numbers for the k'th element of the l'th electrode

11:       x_e: Extract node locations for the k'th element of the l'th electrode

12:       $A_{W\,e}(x_e, z_l)$: Evaluate Equation (A.31) or (A.38)

13:       Store of element degrees of freedom and element matrix:

14:          i$\{m\} \leftarrow$ global node numbers as indices to $A_{W\,e}$

15:          j$\{m\} \leftarrow$ array corresponding to electrode number, l

16:          v$\{m\} \leftarrow A_{W\,e}(:)$

17:    **end for**

18: **end parfor**

19: Assembly of $\boldsymbol{A}_W$ Matrix:

20:    $\boldsymbol{A}_W = sparse(cell2mat(i), cell2mat(j), cell2mat(v), n_n, L)$

Algorithm 4 A_D Assembly

 1: Import: Electrode Connectivity, Nodal Coordinates, z_l

 2: Extract mesh parameters:

 3:    L: Total number of electrodes

 4: Initialize index counter, $m = 0$

 5: **parfor** $l = 1, 2, \ldots L$ **do**

 6:    n_e: Define the total number of elements belonging to the l'th electrode

 7:    **for** $k = 1, 2, \ldots n_e$ **do**

 8:       $m = m + 1$

 9:       nodes: Extract global node numbers for the k'th element of the l'th electrode

10:       x_e: Extract node locations for the k'th element of the l'th electrode

11:       h_e or A_e: Evaluate Equation (A.29) or (A.36)

12:       Store of indices and element line length or triangle area:

13:          i$\{m\}$, j$\{m\} \leftarrow$ electrode number, l

14:          v$\{m\} \leftarrow h_e/z_l$ or A_e/z_l

15:    **end for**

16: **end parfor**

17: Assembly of $\boldsymbol{A}_D$ Matrix:

18:    $\boldsymbol{A}_D = sparse(cell2mat(i), cell2mat(j), cell2mat(v), L, L)$

VITA

(209) 612-1994
West Lafayette, IN
Herna283@purdue.edu

Julio Andres Hernandez
Ph.D. Candidate

LinkedIn: julioastroh
Lab: TNT Labs
Citizenship: USA

Ph.D. Candidate in Aeronautical and Astronautical Engineering specializing in developing multifunctional materials for embedded sensing applications. My background in mathematics, mechanical engineering, and aerospace engineering provides a strong foundation for conducting fundamental research and solving real-world engineering problems. I aim to ensure the structural integrity of aircraft and spacecraft through smart materials and advanced manufacturing techniques. My ultimate goal is to develop application-specific integrated sensing elements, instrumentation, and nondestructive evaluation technologies to protect engineering and human assets.

Research Interests

Additive Manufacturing, Self-actuating/sensing Materials, Multifunctional/Smart Composite Structures, Embedded Sensing, Electrical Impedance Tomography, Multi-Physics Modeling, Machine Learning, Human Space Exploration

SKILLS

Tools and Languages	Abaqus, LabVIEW, LaTeX, MATLAB, SolidWorks, Trelis
Communication	English (native), Spanish (basic)
Manufacturing	Additive Manufacturing, Fiber-reinforced Composites,Nanocomposites, Sandwich Composites, VARTM
other	Class 200 cleanroom, Design of Experiments, Multi-disciplinary Optimization, Reliability-centered Maintence

RECENT WORK EXPERIENCE

Graduate Researcher   **August 2016 — Present**
Purdue University   *West Lafayette, IN*

- Led research on developing multifunctional filament for Fused Filament Fabrication Additive Manufacturing.
- Employed a Design of Experiments (DOE) to improve the performance of conductive piezoresistive filament with the goal of fabricating sensing elements for surface-mounted and embedded sensing applications.
- Proficient in using multiphysics computational tools to model and simulate piezoresistive and elastodynamic behavior.
- Provided regular progress updates to funding agencies and industrial/academic collaborators, such as the Naval Surface Warfare Center (NSWC), by producing quarterly reports identifying research goals and defining current/future work.
- Delivered findings in technical reports, presentations, and scholarly journal publications.
- Defined, designed, and delivered completed research problems to advance the state-of-the-art in multifunctional additive manufacturing and piezoresistive embedded sensing fields. Demonstrated expertise in all stages of project life cycles.

- Established best practices and standard operating procedures for laboratory equipment and nanocomposite manufacturing processes, ensuring consistent operation and electromechanical performance.
- Conducted semi-annual lab safety reviews, chemical inventory checks, maintained updated safety data sheets, and conducted in-person training as the Lab Manager and Designated Training Individual.
- Mentored undergraduate and graduate researchers in conducting literature reviews, identifying research gaps, planning experiments, analyzing data, and presenting results both in writing and verbally; providing mentorship is a top personal priority.
- Facilitated productive and ongoing collaborations between four lab groups across two universities, bringing together six principal investigators, six Ph.D. students, and multiple masters and undergraduate students.

Key Achievements:

- Authored/Co-authored 13 peer-reviewed scientific publications in leading journals and 12 conference manuscripts.

Student Intern   **June 2015 — December 2015**
National Ignition Facility, Lawrence Livermore National Laboratory   *Livermore, CA*

- Provided general assembly, engineering testing, and documentation for hoisting assemblies, as per LLNL Design Safety Standards.
- Created CAD drawings and schematics of mechanical components to the sub-assembly level of optical beamline systems.
- Assessed and resolved complex issues with mechanical and electrical hardware with minimal supervision.
- Installed sensitive diagnostic equipment in class 200 cleanroom environment during scheduled facility maintenance periods.

Key Achievements:

- Revised and consolidated six preventative maintenance procedures into a single document to save the National Ignition Facility 56 technician hours annually.

Student Intern   **May 2014 — August 2014**
Environmental Restoration Dept., Lawrence Livermore National Laboratory Livermore, CA

- Spearheaded a complex internal project to redeploy a portable treatment unit to a location with high pollution concentration in the water table; prepared complete models and drawings in AutoCAD.
- Performed pipe sizing, pump head requirement, pump selection, and engineering calculations associated with providing adequate fluid flow rate to remove pollution and other volatile organic compounds from the water table
- Provided independent engineering support and operational solutions to resolve complex operational, maintenance, refurbishment, and reliability issues on portable groundwater treatment units

Key Achievements:

- Obtained 20-year approval for the relocation of the portable treatment unit from LLNL administration

Undergraduate Researcher   **January 2013 — June 20134**
University of the Pacific   *Stockton, CA*

- Diagnosed and debugged Linux programming and Gfortran90 compiling codes.
- Interpreted simulated strain data of turbine blades from cluster analysis.

EDUCATION

Ph.D. Aeronautical and Astronautical Engineering, GPA: 3.61, *Purdue University*   2023
MS Aeronautical and Astronautical Engineering, GPA: 3.72, *Purdue University* May 2019
MS Engineering Sciences, GPA: 3.76, *University of the Pacific*   May 2016
BS Mechanical Engineering, GPA: 3.76, *University of the Pacific*   May 2016
AS Mathematics, GPA: 3.52, *San Jacinto Community College*   May 2012

AWARDS AND DISTINCTIONS

AAE Summer Research Fellowship, *Purdue University*   April 2023
College of Engineering Award for Outstanding Service, *Purdue University*   March 2021
Recognition of a graduate student who has contributed to the quality, reputation, and success of the graduate student community, School, College, and University.
Estus Magoon Award for Excellence in Teaching, *Purdue University*   March 2019
Institutional service award recognizing profound and promising skills in being an educator.
HENAAC Scholarship, *Great Minds in STEM*   August 2013 & 2019
A national scholarship supporting underrepresented students in STEM.
Ross Graduate Fellowship, *Purdue University*   August 2016
Recruitment fellowship for outstanding Ph.D. track students.
Outstanding Mechanical Engineer Graduate Award, *University of the Pacific*   May 2016
Given to one student a year that has displayed excellent academic ability, involvement in extracurricular activities, and a solid commitment to community service.
Eagle Scout, *Boy Scouts of America*   2002—2012
Highest achievement and rank attainable in the Scouting program. Only four percent of Scouts have earned this rank after committing to years of community service, leadership, and a review process.

KEY PUBLICATIONS

J. A. Hernandez, C. Maynard, D. Gonzalez, M. Viz, C. O'Brien, J. Garcia, B. Newell, and T. N. Tallman, 2022, "The Development and Characterization of Carbon Nanofiber/Polylactic Acid Filament for Additively Manufactured Piezoresistive Sensors," Additive Manufacturing, 58, 102948.

J. A. Hernandez, N. Kedir, B. H. Lim, W. Chen, and T. N. Tallman, 2020, "An Experimental Study on the Piezoresistive and Mechanical Behavior of Carbon Nanocomposites Subject to High-Rate Elastic Loading," Composites Science and Technology, 198, 108285.

T. N. Tallman and J. A. Hernandez, 2017, "The Effect of Error and Regularization Norms on Strain and Damage Identification via Electrical Impedance Tomography in Piezoresistive

Nanocomposites," Nondestructive Testing & Evaluation International, 91, 156-163.
PATENTS

- Provisional patent (US-69740-01): Wet-mixing processes, electrically conductive fused deposition modeling (FDM) materials, 3D printable FDM filaments, electrically conductive inks, and associated methods. (Submitted for review)

PUBLICATIONS

Journal Manuscripts

13. J. Gao, N. Kedir, J. A. Hernandez, F. Zhou, J. T. Tsai, T. N. Tallman, M. B. G. Jun, and W. Chen, 2022, "Dynamic Failure of Composite Strips Under Reverse Ballistic Impact," International Journal of Mechanical Sciences, 234, 107700.

12. J. A. Hernandez, C. Maynard, D. Gonzalez, M. Viz, C. O'Brien, J. Garcia, B. Newell, and T. N. Tallman, 2022, "The Development and Characterization of Carbon Nanofiber/Polylactic Acid Filament for Additively Manufactured Piezoresistive Sensors," Additive Manufacturing, 58, 102948.

11. J. Gao, N. Kedir, J. A. Hernandez, J. Gao, T. Horn, G. Kim, K. Fezzaa, T. N. Tallman, G. Palmese, R. Sterkenburg, and W. Chen, 2022, "Dynamic Fracture of Glass Fiber-Reinforced Ductile Polymer Matrix Composites and Loading Rate Effect," Composites Part B: Engineering, 235, 109754.

10. N. Kedir, J. A. Hernandez, B. H. Lim, J. Gao, X. Zhai, Y. Nie, M. N. Issahaq, T. N. Tallman, and W. Chen, 2021, "Effect of Laser Irradiation Time on the Surface Characteristics of a Carbon Fiber Composite," Journal of Laser Applications, 33, 042034.

9. A. J. Fairbanks, T. D. Crawford, J. A. Hernandez, J. D. Mateja, X. Zhu, T. N. Tallman, and A. L. Garner, 2021, "Electromagnetic Properties of Multiphase Composites Containing Barium Strontium Titanate and Nickel Zinc Ferrite Inclusions From 1-4 GHz," Composites Science and Technology, 211, 108826.

8. J. Gao, N. Kedir, C. Kirk, J. A. Hernandez, J. Wang, S. Paulson, X. Zhai, T. Horn, G. Kim, K. Fezzaa, F. De Carlo, P. D. Shevchenko, T. N. Tallman, R. Sterkenburg, and W. Chen, 2021, "High-Speed Synchrotron X-Ray Phase Contrast Imaging for Evaluation of Microscale Damage Mechanisms and Fracture Toughness of Cross-Ply GFRCs," Composites Science and Technology, 210, 108814.

7. J. Gao, Z. Guo, J. A. Hernandez, F. Zhou, Y. Nie, J. Gao, B. H. Lim, N. Kedir, X. Zhai, J. Wang, J. T. Tsai, F. De Carlo, P. D. Shevchenko, T. N. Tallman, M. B. G. Jun, G. R. Palmese, and W. Chen, 2021, "Transverse Impact by RCCs on S-Glass and Kevlar® FRC Strips," Composites Part A: Applied Science and Manufacturing, 146, 106425.

6. A. J. Fairbanks, T. D. Crawford, J. A. Hernandez, J. D. Mateja, X. Zhu, T. N. Tallman, and A. L. Garner, 2021, "Electromagnetic Measurements of Composites Containing Barium Strontium Titanate or Nickel Zinc Ferrite Inclusions From 1-4 GHz," Composites Science and Technology, 210, 108798.

5. T. D. Crawford, A. J. Fairbanks, J. A. Hernandez, T. N. Tallman, and A. L. Garner, 2021, "Nonlinear Permeability Measurements for Nickel Zinc Ferrite and Nickel Zinc Ferrite/Barium Strontium Titanate Composites From 1-4 GHz," IEEE Transactions on Magnetics, 57, 6100810.

4. J. Gao, N. Kedir, C. Kirk, J. A. Hernandez, J. Wang, S. Paulson, X. Zhai, T. Horn, G. Kim, J. Gao, K. Fezzaa, F. De Carlo, P. D. Shevchenko, T. N. Tallman, R. Sterkenburg, G. R. Palmese, and W. Chen, 2021, "Real-Time Damage Characterization for GFRCs Using High-Speed Synchrotron X-Ray Phase Contrast Imaging," Composites Part B: Engineering, 207, 108565.

3. J. Gao, C. Kirk, N. Kedir, S. Paulson, J. A. Hernandez, J. Gao, X. Zhai, J. Wang, T. Horn, G. Kim, F. De Carlo, P. D. Shevchenko, T. N. Tallman, G. R. Palmese, R. Sterkenburg, and W. Chen, 2021, "A Method for Characterization of Multiple Dynamic Constitutive Parameters of FRCs," Composites Science and Technology, 203, 108607.

2. J. A. Hernandez, N. Kedir, B. H. Lim, W. Chen, and T. N. Tallman, 2020, "An Experimental Study on the Piezoresistive and Mechanical Behavior of Carbon Nanocomposites Subject to High-Rate Elastic Loading," Composites Science and Technology, 198, 108285.

1. T. N. Tallman and J. A. Hernandez, 2017, "The Effect of Error and Regularization Norms on Strain and Damage Identification via Electrical Impedance Tomography in Piezoresistive Nanocomposites," Nondestructive Testing & Evaluation International, 91, 156-163

Conference Proceedings

12. D. Rodriguez, C. Maynard, J. A. Hernandez, C. O'Brien, T. N. Tallman, B. Newell, and J. Garcia, 2022, "3D Printed Flexible Dielectric Electroactive Polymer Sensors," Proceedings of ASME Smart Materials, Adaptive Structures, and Intelligent Systems, Dearborn, MI.

11. J. A. Hernandez, H. Zhu, F. Semperlotti, and T. N. Tallman, 2022, "Electrode Spacing-Induced Signal Filtering for Transient Piezoresistivity," Proceedings of SPIE Smart Structures/NDE, Long Beach, CA.

10. C. Maynard, J. A. Hernandez, D. Gonzalez, M. Viz, C. O'Brien, T. N. Tallman, J. Garcia, and B. Newell, 2021, "Functionalized Thermoplastic Polyurethane for FDM Printing of Piezoresistive Sensors," Proceedings of ASME Smart Materials, Adaptive Structures, and Intelligent Systems, digital forum.

9. J. A. Hernandez, H. Zhu, F. Semperlotti, and T. N. Tallman, 2021, "The Transient Response of Piezoresistive CNF-Modified Epoxy Rods to One-Dimensional Wave Packet Excitation," Proceedings of ASME Smart Materials, Adaptive Structures, and Intelligent Systems, digital forum.

8. J. A. Hernandez, C. M. Maynard, D. Gonzalez, M. Viz, J. Garcia, B. Newell, and T. N. Tallman, 2021, "On the Performance of Additively Manufactured CNF/PLA Piezoresistive Strain Sensors," Proceedings of SPIE Smart Structures/NDE, digital forum.

7. J. Gao, N. Kedir, C. Kirk, J. A. Hernandez, X. Zhai, J. Wang, T. N. Tallman, K. Fezzaa, and W. Chen, 2020, "Real-Time Visualization of Damage Progression Inside GFRP Composites via High-Speed X-Ray PCI Technique," Proceedings of the Society for Experimental Mechanics 14th International Congress, Albuquerque, NM.

6. J. Gao, N. Kedir, C. D. Kirk, J. A. Hernandez, J. Wang, X. Zhai, T. Horn, G. Kim, K. Fezzaa, F. De Carlo, P. Shevchenko, T. N. Tallman, R. Sterkenburg, and W. Chen, 2020, "In-Situ Observation of Dynamic Damage Evolution Inside GFRCs Through High-Speed X-Ray PCI," Proceedings of the American Society for Composites 35th Technical Conference, Hoboken, NJ.

5. J. A. Hernandez and T. N. Tallman, 2020, "The Piezoresistive Response of CNF/Epoxy to One-Dimensional Strain Wave Excitation via Remote Loading," Proceedings of ASME Smart Materials, Adaptive Structures, and Intelligent Systems, digital forum.

4. C. M. Maynard, J. A. Hernandez, A. Doak, B. Mardikis, M. Viz, B. Newell, J. Garcia, and T. N. Tallman, 2020, "A Computational Study of Strain Sensing via 3D-Printed CNF-Modified PLA Strain Gauges," Proceedings of ASME Smart Materials, Adaptive Structures, and Intelligent Systems, digital forum.

3. C. Maynard, J. A. Hernandez, D. Gonzalez, T. N. Tallman, J. Garcia, and B. Newell, 2020, "The Effect of Extrusion Temperature and Cycles on Electrical Resistivity in Carbon Nanofiber-Modified PLA Filament for Multi-Functional Additive Manufacturing," Proceedings of SPIE Smart Structures/NDE, digital forum.

2. J. Gao, Z. Guo, Y. Nie, J. A. Hernandez, B. H. Lim, N. Kedir, T. N. Tallman, and W. Chen, 2019, "Transverse Impact on a Single Layer S-Glass/SC15 Epoxy Composite Strip," Proceedings of the American Society for Composites 34th Technical Conference, Atlanta, GA.

1. J. A. Hernandez and T. N. Tallman, 2019, "On the Transient Piezoresistive Response of Impacted NanofiberModified Epoxy," Proceedings of SPIE Smart Structures/NDE, Denver, CO.

INDEX